1997

Stability and electronic properties of amorphous silicon p-i-n devices fabricated using ECR plasma enhanced chemical deposition

Sanjeev Kumar Kaushal
Iowa State University

INFORMATION TO USERS

This manuscript has been reproduced from the microfilm master. UMI films the text directly from the original or copy submitted. Thus, some thesis and dissertation copies are in typewriter face, while others may be from any type of computer printer.

The quality of this reproduction is dependent upon the quality of the copy submitted. Broken or indistinct print, colored or poor quality illustrations and photographs, print bleedthrough, substandard margins, and improper alignment can adversely affect reproduction.

In the unlikely event that the author did not send UMI a complete manuscript and there are missing pages, these will be noted. Also, if unauthorized copyright material had to be removed, a note will indicate the deletion.

Oversize materials (e.g., maps, drawings, charts) are reproduced by sectioning the original, beginning at the upper left-hand corner and continuing from left to right in equal sections with small overlaps. Each original is also photographed in one exposure and is included in reduced form at the back of the book.

Photographs included in the original manuscript have been reproduced xerographically in this copy. Higher quality 6" x 9" black and white photographic prints are available for any photographs or illustrations appearing in this copy for an additional charge. Contact UMI directly to order.

UMI

A Bell & Howell Information Company
300 North Zeeb Road, Ann Arbor MI 48106-1346 USA
313/761-4700 800/521-0600

Stability and electronic properties of amorphous silicon p-i-n devices fabricated using ECR plasma enhanced chemical deposition

by

Sanjeev Kumar Kaushal

A dissertation submitted to the graduate faculty
in partial fulfillment of the requirements for the degree of
DOCTOR OF PHILOSOPHY

Major: Electrical Engineering (Microelectronics)
Major Professor: Vikram L. Dalal

Iowa State University
Ames, Iowa
1997

Graduate College
Iowa State University

This is to certify that the Doctoral dissertation of

Sanjeev Kumar Kaushal

has met the dissertation requirements of Iowa State University

Signature was redacted for privacy.

Committee Member

Signature was redacted for privacy.

Committee Member

Signature was redacted for privacy.

Committee Member

Signature was redacted for privacy.

Committee Member

Signature was redacted for privacy.

Major Professor

Signature was redacted for privacy.

For the Major Program

Signature was redacted for privacy.

For the Graduate College

To my parents,

Swatantarta Devi and Satya Pal Sharma

TABLE OF CONTENTS

ABSTRACT

The prime, objective of the research was to investigate the fabrication, stability and electronic properties of a-Si:H devices deposited using electron cyclotron resonance (ECR) plasma deposition technique. Both reactive (hydrogen) and non-reactive (helium) gases were used as the primary plasma gas. The reactants generated by the ECR plasma from these gases were allowed to flow towards the substrate, where they reacted with silane to give rise to growth of a-Si:H. In general, we used a high dilution ratio of plasma gas (H_2 or He) to silane, about 15:1 to 20:1; for growing a-Si:H. Very high quality a-Si:H films could be deposited using H-ECR plasma at relatively higher temperatures (325°C - 375°C). The use of He in the discharge does not lead to any etching during growth (as with H-plasma), but does lead to significant ion bombardment. We found that by using a highly diluted He-ECR growth technique, we can reduce the Tauc bandgap of a-Si:H to 1.67eV, which is significantly lower than the 1.75eV obtained with H as the plasma gas. We further found that the hydrogen content in the films grown using He dilution was much lower than the H content in the films made using H-dilution. The microstructure of these films were further probed using TEM. We succeeded in making reasonable quality devices from the ECR-deposited a-Si:H materials prepared at high temperatures. The devices were deposited both on tin oxide (superstrate) and stainless steel (substrate) substrates. To deposit the superstrate type devices on tin oxide substrate we had to overcome various problems, such as reduction in tin oxide at high temperature and diffusion of B across the p-i interface at high temperature. The reduction in tin oxide was avoided by using a He-diluted p-layer deposited at low temperature. The diffusion of 'B' was avoided by using an a-Si:H buffer layer with a high C content between the p and i-layer. We found that the design of the buffer layer was critical to achieving good performance. While we had successfully solved these problems at lower temperatures (up to 360°C), it

became progressively more difficult to solve the diffusion problem as the growth temperature was increased. These problems were overcome by the use of a substrate cell geometry. We could finally achieve fill factors of about 72% using such geometries. We also investigated the stability of the cells that we made using ECR plasma and compared it with the cells grown using glow discharge growth technique. We found that the solar cells made using H-ECR growth technique were more stable than those made using glow discharge technique. The hole mobility lifetime product ($\mu\tau$) has not been previously measured in a-Si:H based devices grown using ECR growth technique. We measured the hole $\mu\tau$ product in devices, by making a systematic series of devices, all with same p and n layers, but with i-layers grown using hydrogen or helium dilutions and at different growth temperatures. Using quantum efficiency spectroscopy, we could deduce the hole $\mu\tau$ product. The quantum efficiency values were accurately modeled by adjusting just two parameters: the p-layer absorption and the hole $\mu\tau$ product. The results were quantified by modifying the earlier model, developed by Greg Baldwin.

I. INTRODUCTION

Interest in hydrogenated amorphous silicon (a-Si:H) owes its origin to the first practical device which was demonstrated with the material - a solar cell [1]. Since then, the interest in this material has grown rapidly, and applications requiring large area microelectronics, such as active matrix flat panel displays [AMLCD], vidicons, light emitting diodes, etc., continue to emerge. Amorphous silicon solar cells have found their way into a myriad of consumer products, as well as remote power generating facilities. By some estimates [2], sales of amorphous silicon photovoltaic cells and modules now exceed that of their crystalline silicon counterparts.

Several key features that make a-Si:H an attractive photovoltaic material are:

1. It has a very high optical absorption coefficient ($>10^5$ cm) over the majority of visible spectrum, making extremely thin film (1000-5000°A) devices possible, which implies low cost.
2. A simple low temperature deposition process can be used to uniformly coat extremely large areas, and in keeping with the spirit of renewable energy, is environmentally beingn.
3. The optical bandgap of ~ 1.7eV lies near the energy at which high energy conversion efficiencies are expected [3].
4. Monolithic integration of individual cells is simply and easily accomplished, thus avoiding costly cut and paste methods.
5. The raw materials i.e. silicon and hydrogen are abundant.
6. The material is easily (although not efficiently) doped both p-type and n-type using boron or phosphorous sources, respectively.

7. The material posses the necessary electron and hole transport properties.

One can conclude from the features cited above, that the use of amorphous silicon gives us an opportunity to achieve high conversion efficiency at low cost. A comparison of the manufacturing costs of the various crystalline silicon methods with amorphous silicon has been performed [4]. This economic analysis of a 25MW capacity solar cell production line indicates that a-Si:H cell based single and tandem devices offer the lowest cc despite the lower assumed conversion efficiency.

The first amorphous silicon solar cells were prepared by Carlson and Wronski in 1974 at what was then RCA's David Sarnoff Research Center [1]. The first devices, which had a conversion efficiency of only 2.4%, were p-i-n (intrinsic a-Si:H) diodes. There has since been a rapid improvement in the performance of amorphous silicon solar cells. Although early work on Schottky devices was promising [5], p-i-n devices permitted the higher open circuit voltages necessary for improved performance [6]. The next major development in device performance was the use of a heterojunction device structure [7]. In these devices, p-type hydrogenated amorphous silicon carbon (a-SiC:H) alloys replaced a-Si:H as the front contact. This allowed for not only higher currents owing to the increased transmission of the doped layer but also improved open circuit voltages as a consequence of the higher built-in potential of the device. The a-Si:H device crossed the 10% conversion efficiency threshold when the improved performance of the a-SiC:H heterojunction devices was combined with the use of textured substrate to enhance optical absorption within the device [8]. Recognition of the importance of recombination at the p/i a-Si:H interface and attempts to reduce the losses by compositional grading have led to further performance improvements [9]. Combining such advanced device concepts with structures designed to maximize light collection have resulted in conversion efficiencies as high as 12% [10] for single function devices.

Although prospects appear excellent for improving the efficiency of single junction devices, the majority of industrial research programs are now focusing on multijunction

devices where much higher conversion efficiencies are predicted. Concerns about light-induced degradation have also spurred interest in multijunction solar cells, which appear considerably more stable [11].

In this thesis, the properties of solar cells based on amorphous silicon fabricated using ECR PECVD will be discussed. Many workers intent on understanding material properties and obtain amorphous materials with improved transport properties have ignored employing devices as a tool of study. In fact, the device which is the ultimate application of the material is the final arbiter of quality. By failing to use devices as a study tool, one is often the victim of the narrow field of view permitted by a few transport, optical and other material measurements. In this thesis we would like to study all these material properties deduced from the performance of a real time device. We will discuss the devices and material preparation, theory of operation, contacts, interface and doping, and solar cell stability.

A. Structural and Electro-Optical Properties of Amorphous Silicon

Many of the structural and physical concepts used to describe the crystalline solid state cannot be applied directly to amorphous metals and semiconductors. For example, the very notion of a lattice defect, such as a dislocation or a point defect, which is quite useful to describe a crystal quality, appears meaningless in a disordered structure. The lack of adequate physical concepts hampers the investigation of the amorphous state of semiconductors. Although great progress has been made in this regard, many difficulties in the understanding of the physical behavior of amorphous materials still remain. For instance, a complete understanding of the important light-induced degradation of amorphous silicon has not yet been achieved. From the perspective of the photovoltaic behavior the description of the amorphous state and the band structure are the most fundamental issues and shall be discussed next.

1. Band gap states

Several deposition processes, such as CVD, PECVD, reactive sputtering, sputter-assisted plasma CVD, and others, can be used to produce amorphous silicon for solar cells, although the (glow discharge) plasma deposition remains the major film deposition method. In these techniques, hydrogen is either added or released during the process and incorporated in to the deposited film. Hydrogenated films contain about 4 to 40 atomic percentage of hydrogen and are generally denoted by a-Si:H. Hydrogen passivates the defect levels in the amorphous films, thereby increasing the photo conductivity. Significant efforts have been made to study the nature of these defects and their interaction with hydrogen. In this regard an important observation in the annealing experiment conducted on undoped a-Si:H by the researchers was the loss of hydrogen for ($T > 500^{o}C$) and the decrease in conductivity as a result of annealing was accompanied by an increase in the density of unpaired electron spins, which can be measured by ESR [13]. Photo conductivity is directly proportioned to the product of lifetime τ and mobility μ; therefore, there is a relationship between $\mu\tau$ and the spin density given by $N_S\mu\tau = \text{constant}$. Since in the amorphous state of a semiconductor unsaturated covalent bonds occur, it is assumed that the ESR signal measures the concentration of unsaturated dangling bonds. This is indicative of the fact that hydrogen is trapped at defects with dangling bonds that are electrically active centers, and if unsaturated reduce the lifetime of free charge carriers.

In a perfect crystalline silicon structure, all four covalent bonds of an atom are saturated, and no unpaired spins occur. Structural models of an amorphous covalently bonded crystal show that the average number of next neighboring atoms are lower than four, so a certain fraction of atoms are only co-ordinated with three or two nearest neighbors. This is shown in Figure 1.1. Atoms with lower co-ordination occur because they locally release the strain in the disordered structure. The threefold co-ordinated atoms process an unpaired (dangling) bond that produces an electron spin signal in an ESR experiment. The amorphous

structure is thus characterized by fourfold, threefold, and twofold co-ordinated atoms and the loss of the long-range order. A bandgap can be defined that determines the optical and electronic properties of the semiconductor. The structure related dangling bond states introduce trap levels in the band gap and thus have to be considered as a part of band structure.

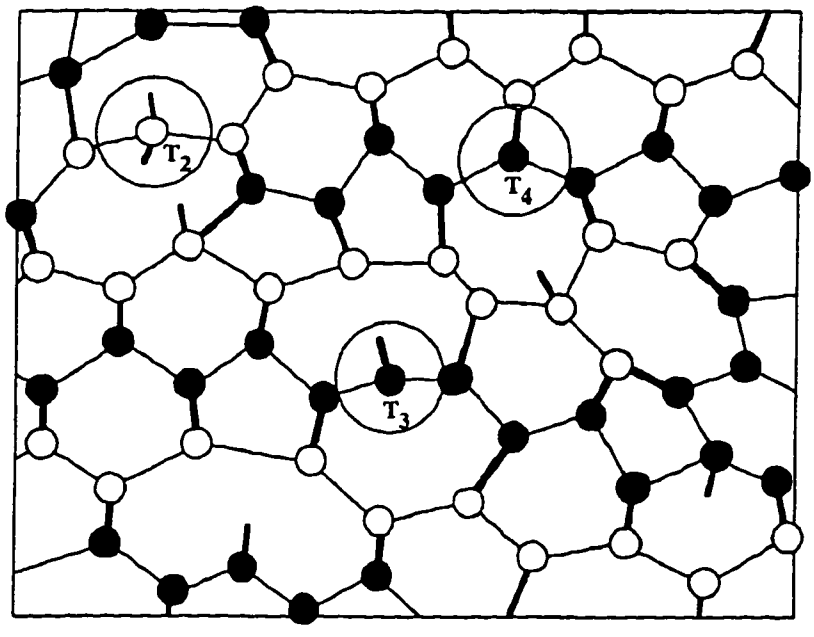

Figure 1.1. Structural atomic model of the covalent bonding in an amorphous semiconductor [12].

In order to describe the configuration of atoms in the structure, the notation T_z^q will be adopted, where 'T' stands for the atom, 'q' for the charge state, and 'z' describes the co-ordination number. A neutral twofold co-ordinated atom T_2^0 can also occur and release the strain more effectively compared to a threefold co-ordinated atom [14]. Since the neutral T_2^0

center has only paired spins, it does not produce an ESR signal and cannot be detected. Nonetheless, it is assumed that these defects also occur. More complicated pairs of charged twofold and threefold co-ordinated atoms T_3^- - T_3^+, complexes of several defects or micro voids.

Hydrogen free amorphous silicon has spin densities of up to 10^{20} cm^3, depending on the deposition conditions, and it is assumed that the spins are related to unco-ordinated covalent bonds. A hydrogen atom with a single electron can supply an electron and complete an unsaturated covalent bond. This removes the dangling bond level from the forbidden bandgap (passivation) and trap the hydrogen. For a good material, the spin density can drop down to 10^{15} cm^{-3} after passivation with hydrogen.

In order to obtain more insight into the electronic properties of amorphous silicon, it is important to determine the distribution of the trap states in the bandgap. Figure 1.2. shows a density of states curve for a n-doped a-Si:H film. Since the majority of atoms are still fourfold co-ordinated, the essential features of the crystalline band-structure, the existence of extended valence and conduction band states, are still maintained. The lack of the long-range order and distortion of the covalent bonds of fourfold co-ordicated neutral silicon atom T_4^0 in the amorphous structure gives rise to a gradual, approximately exponential decrease of the density of states, so called band tails, given by

$$N_{TC} = N_{C0} \exp\left(\frac{E_c - E}{kT_{TC}}\right) \tag{1.1}$$

$$N_{TV} = N_{V0} \exp\left(\frac{E - E_V}{kT_{TV}}\right) \tag{1.2}$$

kT_{TC} and kT_{TV} are the characteristic widths of the conduction and valence band tails respectively. In silicon, typical values are about $N_{C0} = N_{V0} = 10^{21}$ to 10^{22} eV^{-1} cm^{-1}, and kT_{TC} = 26m eV and kT_{TV} = 42m eV, which indicates that the valence band tail extends deeper into the gap [15].

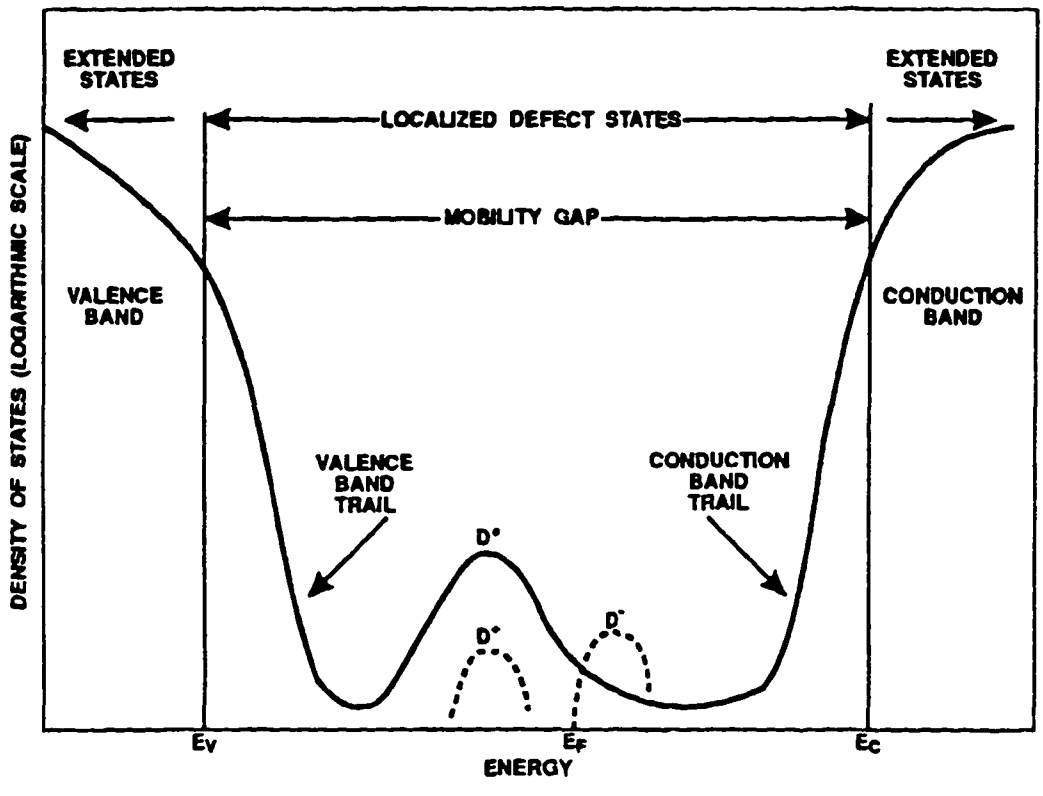

Figure 1.2. Electronic density of states in the mobility gap of a-Si:H.

A fraction of tail states also originates from silicon atoms with three silicon neighbors and one hydrogen atom in tetrahedral configuration. These additional states from the silicon-hydrogen bond changes the optical band-gap, depending on the hydrogen content. The optical gap increases from about 1.5eV for pure amorphous silicon to about 2.0eV when 30 at. %

hydrogen is present. All states in the valence band tail $T_4^{+/0}$ are donor-like; i.e. positive when empty and neutral when full. The states in the conduction band tail $T_4^{0/-}$ are acceptor like; they are neutral when empty and negative when occupied.

Grossly distorted bonds form states deeper inside the gap, and there exists a critical considered localized states. These critical energies are called the mobility edges (E_C, E_V) and are located below the optical band gap edges. The localized states inside the mobility edges essentially determine the Fermi energy and the electrical transport properties.

Adjacent to the band tail states are two deep-level bands in the lower and upper-half of the bandgap (at about E_C-0.4eV, E_C+0.6eV in amorphous silicon), which are considered to be related to dangling bonds of mainly threefold co-ordinated silicon atoms as shown Figure 1.3. These defect bands consist of two different charge states of the neutral dangling bond T_3^0. The separation of the two levels is due to the electrostatic correlation energy of the two electrons. It is mostly assumed that the upper levels $E_{db}^{0/-}$ correspond to the negatively charged defect $T_3^- \Leftrightarrow T_3^0 + e$ when an electron is trapped, and the lower levels $E_{db}^{+/o}$ to the positive charge defect $T_3^- \Leftrightarrow T_3^0 - e$. As can be seen in Figure 1.3, the shift in the Fermi level changes the concentration of positively and negatively charged states. In an undoped material, the bonds are neutral and occupied by one electron. In a p-type material the lower levels ($E_{db}^{+/o}$) begin to empty and positively charged dangling bonds T_3^+ dominates carrying no electrons. In n-type material, the upper levels ($E_{db}^{0/-}$) become partly (or totally) occupied, and the negatively charged dangling bonds T_3^- with two electrons dominate.

The capture cross sections for electron σ_n and holes σ_p for the donor $T_3^{+/0}$ and acceptor $T_3^{0/-}$ differ considerably: $\sigma_n^+ >> \sigma_p^+$ and $\sigma_n^- << \sigma_p^-$; respectively, while the capture cross sections for the electrons and holes for the neutral state are about equal $\sigma_n^0 \approx \sigma_p^0$. These dangling bonds states are effective recombination centers, especially in undoped a-Si:H,

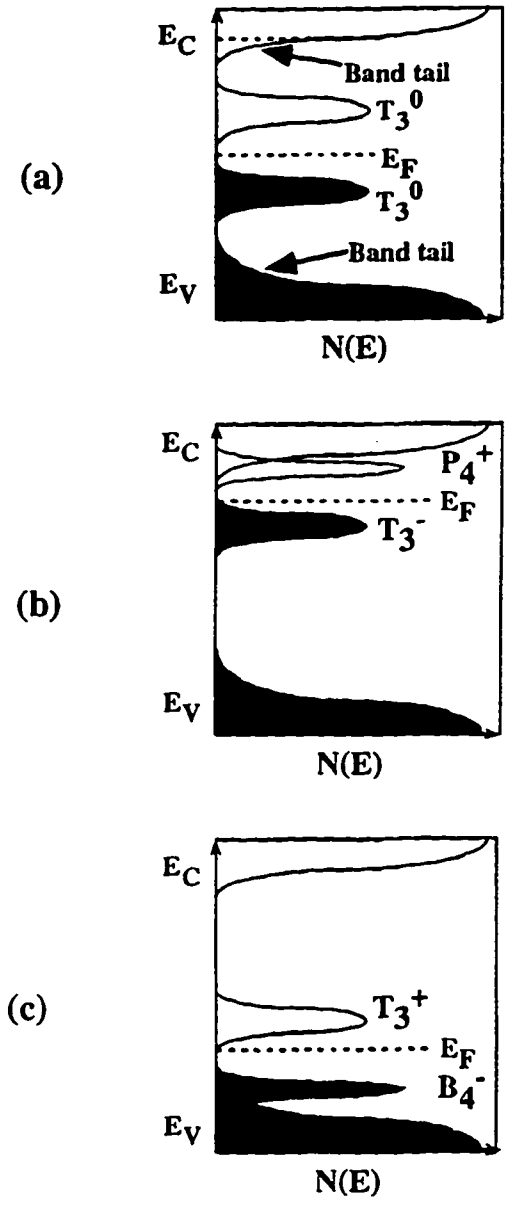

Figure 1.3. Simplified density of states model for dangling bond states in undoped and doped a-Si:H. (a) undoped; (b) heavily p-doped; (c) B-doped films [16].

where they can capture electrons and holes. A consequence of the different charge states is therefore that the lifetime in undoped a-Si:H is rather low and depends on the position of Fermi energy.

Amorphous silicon usually also contains impurities that contribute to the density of states in the band gap. The most common impurities are oxygen, carbon, and nitrogen with concentrations typically in the range of about 10^{18} to 10^{20} cm^{-3}. These impurities have been shown to effect the diffusion length been shown to effect the diffusion length and thus the efficiency of solar cells.

2. Doping in a-Si:H

The problem of doping in amorphous silicon becomes evident if one considers that atoms in the disordered structure are to some extent rather threefold co-ordinated compared to the fourfold co-ordination in crystalline silicon. Doping atoms in the crystalline structure supplies holes and electrons due to an excess or deficiency of electrons compared to the number of electrons necessary to form four covalent bonds (formulated as the 8-N rule). It has been argued that a doping atom on a substitutional threefold co-ordinated site will therefore not be able to supply holes or electrons according to this basic argument. Nonetheless, one can observe a doping effect in a-Si:H; however, only a fraction of the incorporated impurity atoms contributes to the free carrier concentration compared to low free carrier concentration in case of hydrogenated a-Si:H is because of both the trapping of carriers in the band gap states and the low activation of the impurity atoms.

Phosphorous is the most common n-type dopant in a-Si:H. Normal structural bonding for phosphorous is threefold and one might expect that all P-atoms are preferentially incorporated in the P_3^0 configuration, where it is electrically inactive and merely a network relaxer. Experimental results, show [16], however that P-atoms are also incorporated in the

fourfold configuration, where they act as a donor $P_4^{+/0}$. A possible explanation may be that phosphorous atoms in the fourfold configuration form a complex with another defect which is energetically comparable with the P_3^+ configuration. Although the configuration of the fourfold p-atom may still be controversial, it is clear that a fraction of the incorporated atoms are electrically active and contribute impurity states to the band tails or just below. One can define the doping efficiency $\eta = [P_4]/[P_{total}]$ of the electrically active component with respect to the total concentration of doping impurities. Despite the low activation of P atoms one can vary Fermi energy over a wide range up to about 0.1eV below the mobility edge for high concentrations of phosphorus.

Boron is the usual p-type dopant in a-Si:H. Because of its complex chemistry it is also difficult to predict the atomic configurations in the network where it becomes electrically active. Experimental data indicate that the vast majority of the boron atoms are in the neutral threefold co-ordinated configuration B_3^0 [14]. As with phosphorus, it has therefore been suggested that a defect pair must form to stabilize the electrically active fourfold configuration. Doping efficiencies of about $\eta < 0.06$ have been reported, which indicates the low activation of boron [16]. For high boron concentrations, the Fermi energy can also can be shifted to about 0.1eV above the mobility edge.

ESR measurements show that for slight doping levels the concentration of dangling bond centers decreases and finally completely disappears. This is in accordance with the conversion of the dangling bond center T_3^0 in to the spin paired centers T_3^- or T_3^+, when the Fermi energy shifts as discussed earlier. With the introduction of more impurity atoms, a new spin signal appears, however. The density of the dangling bond states N_{db} has been found to increase as $N_{db} \approx (N_d^{tot})^{1/2}$, where N_d^{tot} is the total concentration of the doping element [17]. For heavily doped films, the ESR signal strength decreases again [18]. These doping-induced deep levels can also be observed in the optical absorption as an increase of the

subband-gap absorption. Although several explanations have been proposed for the doping-induced deep trap centers, the nature of the dangling bond center remains controversial.

Summarizing the doping behavior, the important result is that the doping in amorphous silicon has two effects. First, it changes the Fermi energy and increases the concentration of free carriers. Second, the doping impurity also introduces new deep-level centers. Because of the increase of deep trap states the density of states of doped a-Si:H is changed compared to the intrinsic material. These new defects also have a significant influence on the electrical conductivity and the lifetime in a-Si:H.

3. Optical Absorption

Crystalline silicon as an indirect semiconductor has a rather low absorption in the visible spectral range, since only a few of the electronic states near the band edge can take part in the absorption process because of the momentum conservation rule and the participation of phonons. This situation is different for amorphous silicon, since most of the electronic states near the band edges (tail states) are available for optical transitions. Correspondingly, the optical absorption coefficient is much higher compared to crystalline silicon, as shown in Figure 1.4. Over most of the visible light region ($1.9eV < h\nu < 4.0eV$), the absorption is greater than $10^4\ cm^{-1}$. For high photon energies ($h\nu > 1.6eV$), the absorption can be described by the energy dependence for direct band transitions. The Tauc band gap E_g, which is obtained by fitting parameter, is here called as the optical band gap. In order to distinguish it from the mobility band gap, which is inferred from transport measurements. The optical gap for a-Si:H is about 1.7eV, and for photon energies above the gap the absorption co-efficient is about ten times higher compared to crystalline silicon. This has the consequence that a film thickness of about 0.5μm is already sufficient to absorb most of the light. It is interesting to note that the reduced penetration that compensates for the low carrier diffusion length and the

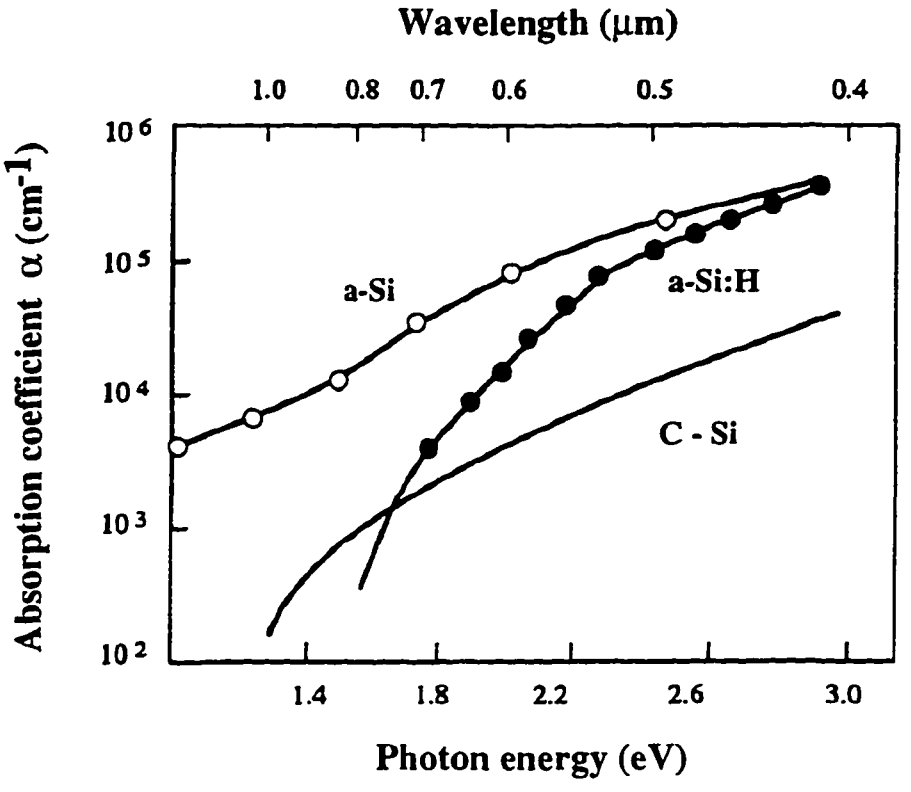

Figure 1.4. Optical absorption coefficient of monocrystalline silicon and hydrogenated and nonhydrogenated amorphous silicon as a function of the photon energy [16].

poor conductivity in amorphous silicon.

For photon energies below the optical gap, the absorption drops off slower compared to the energy dependence extrapolated from higher energies. This increased sub-bandgap absorption can be described by the Urbach law

$$\alpha_U(\nu) = C(\nu)\exp\left\{\frac{E_g - h\nu}{E_0}\right\} \tag{1.3}$$

where E_0 is the Urbach energy which relates directly to the characteristics distribution width of the band tail states. An important consequence of the tail states is that nonradiative recombination can occur, which limits the life time and is thus inescapable for amorphous semiconductors. This is important for photovoltaic applications, since a limitation of the lifetime also limits the open circuit voltage in solar cells. The density of these extended states and band tail states also determine the absorption of photons. This provides yet another way of defining the bandgap. The absorption co-efficient depends upon the extended states density distribution, which may be approximated as parabolic near the band edges. Under this approximation the absorption co-efficient a follows the relation

$$(\alpha h\nu)^{1/2} = B\left[h\nu - E_g\right] \tag{1.4}$$

where hν is the energy of the incident photon, 'B' is the material dependent prefactor, and E_g is the bandgap. The prefactor 'B' for amorphous semiconductor is given by

$$B = \sqrt{\frac{4\pi\sigma_0}{ncE_w}} \tag{1.5}$$

where E_W is the extent of band tailing. The bandgap measured above is known as Tauc gap because Tauc et.al. made this approximation. Since the bands may not be parabolic at the edges, the above gap is not entirely accurate.

One another method of defining an energy gap is to simply designate the energy where photon absorption reaches a value of 10^4 cm^{-1} and is known as the E_{04} gap.

The valence band tail characteristics energy of a-Si:H is usually determined by $d(h\nu)/d(\ln\alpha)$ from the straight line region of the sub-bandgap optical absorption co-efficient a (in logarithmic scale) vs. photon energy (hν) plot. The valance band tail of low defect density

a-Si:H has an exponential slope of about 45meV and the broader than the conduction band tail which is usually about 25meV. Thus it dominates the joint density of states. Since the slope, E_0, of the Urbach absorption reflects the shape of the valence band tails, it follows that E_0 varies with structural disorder. For example, one measure of disorder is the average bond angle variation, which is measured from the width of the vibrational spectrum using Raman spectroscopy. The defect density is another measure of disorder and also increases with the band tail slope. Therefore E_0 is very good measure o the material quality. The smaller the value of E_0, the better the film quality. Thus by establishing the correlation between E_0 and other material parameters such as transport parameters and optical characteristics would provide us with a useful technique for estimating the material quality. Finding this correlation will be one of the goals of the project.

The deeper energy levels within the bandgap have a strong influence on the absorption for low photon energies. Figure 1.4. shows, for instance, that hydrogen-free amorphous silicon has a significantly larger absorption below the mobility gap of about 1.7eV for lower photon energies, which is due to the much higher density of trapping states in the gap. The passivation of these states in a-Si:H decreases the sub-bandgap absorption significantly. The incorporation of hydrogen also changes the optical bandgap, which varies between 1.6eV and 1.8eV.

Doping has a similar effect: it generally increases the absorption in entire visible range, but particularly at lower photon energies. This has important consequences for the device design, since doped regions also have high recombination losses and as much as 20% of the incident light can be lost, for instance, in the boron doped p-layer, which is about 10nm thick for p-i-n cell.

4. Metastability

Hydrogenated amorphous silicon presents a serious problem which is less desirable for photovoltaic applications. The current voltage (I-V) characteristics of a-Si:H solar cells degrade upon exposure to light. The effect, which is quickly removed upon heating above about 150°C, is usually assumed to be associated with the light include charges in photo conductivity known as the Staebler-Wronski (S-W) effect, named after the people who reported it first [19, 20]. It can involve enormous changes in conductivity, which has of course strong implication for the technical applications. Whereas the original state has a clearly defined conductivity, the metastable state can have a range of conductivity depending on the light exposure.

ESR measurements show that during illumination the dangling bond density increases from low starting value of about 10^{16} cm^{-3} up to values of about 10^{17} cm^{-1} and thus reduces the minority carrier diffusion length [21].

The light induced creation of defects appears to be an intrinsic bulk effect which is probably self-limiting. The mechanism for the creation of the light induced defect is most likely the nonradiative recombination of photo-generated carriers. A model [22] based on the detailed balance between photo-generated carriers and the recombination of the excess carriers leading to generation of neutral, positive and negatively charged dangling bonds leads to the relationship

$$N_s \propto t^{\frac{1}{3}} G^{\frac{2}{3}} \tag{1.6}$$

where N_S is the spin density, t is the illumination time and G is the generation rate. The process is self-limited because recombination of the excess carriers via the photo-induced defects successfully complete with the process leading to the light induced defects. Hence, at

long timer, fewer carriers recombine via the defect forming pathway. The $t^{1/3}$ and $G^{2/3}$ behavior have been found experimentally from ESR measurements as a function of time and illumination intensity. In a similar fashion, the kinetics of the annealing of the defects have been studied [23], and shown to be monomolecular with the rate R obeying the relationship

$$R = \nu_0 \exp\left(\frac{-E_a}{kT_A}\right) \tag{1.7}$$

where ν_0 is an anneal prefactor, T_A is the annealing temperature, k is Boltzmann's constant, and E_a is the activation energy. Carbon [24] and oxygen [25, 26] have also been shown to rapidly increase the rate of light induced degradation. Intrinsic structural considerations, such as the concentrations of SiH_2 bonds in the solid, have also been shown to markedly increase the rate of degradation [27].

Redfield, in a series of recent papers [28], has argued that the light induced defect data can be fit by an alternative to earlier expression in which stretched exponential given an accurate fit to the data, and implicitly predicts the saturation of the light induced defect density. That saturation indeed occurs and has been demonstrated by Parketal [29] using high-intensity laser illumination. The form of the stretched exponential is given by

$$D = D_s - (D_s - D_o)\exp(-wt^2) \tag{1.8}$$

where D is the light induced defect density at time t, D_S is the saturated value of the defect density, D_O is the initial defect concentration, 'z' is a parameter describing dispersive process, and 'w' is a rate constant includes terms describing the efficiency of optical generation and annealing of defects. The transition from the metastable state to the original state by annealing

is a thermally activated process which has a unique activation energy of about 1.5eV independent of the material and the conditions under which the metastable state has been

reached. It has been observed that this value is close the activation energy for the diffusion of hydrogen in amorphous silicon, which may suggest that hydrogen plays a role in the formation and/or passivation of metastable defects.

B. Devices

Two basic a-Si:H device configurations have been employed for high efficiency devices. In a "superstrate" or "substrate up" device, the film comprising the device is deposited onto a transparent material. Light passes through the substrate first before reaching the film. In second case (substrate device), light enters the device first and support is provided from the rear. Each design imposes special contact requirements and has important consequences on the nature of interfaces. Unlike their crystalline counterparts, the most efficient a-Si:H and alloy based solar cells employ a p-i-n device structure. This is a consequence of the very small minority carrier transport in the doped material. The p-type layer is approximately 100¤A thick and obviously a wide band gap is preferred for this layer. Boron doped a-(Si,C):H has found extensive use for this purpose [30]. The i-region of the device is undoped and may range in thickness up to 10,000¤A based on practical considerations. As we will discuss later, the thickness of the i-layer not only determines the initial efficiency, but also the long term performance of the device. A n^+ layer, usually phosphorous doped, approximately 100-500¤A thick, completes the active device. An electrode at the rear of the device serves as both an ohmic contact to the n^+ layer and rear-reflection.

1. Device Models

The first comprehensive model of device operation was described by Swartz [31], who solved the charge transport equations assuming a constant lifetime throughout the i-region, using a single-level recombination model. Later Crandall proposed a model based on effective drift lengths assuming a uniform electric field [32]. The current collection efficiency was determined by an effective collection length, Lc, given by

$$L_c = L_e + L_h \tag{1.9}$$

where L_e and L_h are the electron and hole drift length, and

$$L_e = \mu_n \tau_n F \tag{1.10}$$

and

$$L_h = \mu_h \tau_h F \tag{1.11}$$

where $\mu_{n,p}$ denotes electron and hole mobility, $\tau_{n,p}$ represent their lifetimes, and F is the electric field. Faughnan and Crandall et.al [33] demonstrated an emprical relationship between the fill factor of amorphous silicon p-i-n solar cells and the collection length determined from the bias dependence of quantum efficiency measurements.

Hack and Shur [34] have advanced a comprehensive model which corrects many deficiencies of the earlier treatments. Their model assumes a continuous exponential distribution of deep localized donor and acceptor-like states in the gap, each with associated characteristic energy (E_d = 0.088eV and E_a = 0.053eV respectively) and a minimum densities of states of 10^{16} cm^{-3} eV^{-1}. The densities of states at the bottom of conduction band and top of

the valence band were assumed to be the same as for crystalline silicon. They concluded that the principal loss of carrier collection is caused by bulk recombination, which is governed primarily by the distribution of free carriers. In contrast to earlier work, they demonstrated that the efficiency of the device is determined by the transport of the limiting carrier (i.e., holes) rather than the sum of individual drift lengths. Their results show that for non uniform illumination through p^+ layer, most recombination occurs through bulk localized states close to the p/i interface where the free electron-hole product is the maximum. Unfortunately; they do not explicitly consider p/i interface recombination in the model.

One of the particular strengths of the model of Hack and Shur [34] is the quantitative affirmation of the experimental observation that devices illuminated through the p^+ contact almost always have higher conversion efficiency than when illuminated through the n^+ contact are limited by the hole concentration is, in turn, determined by the hole mobility, i.e. the holes ability to escape the high concentration of electrons in the vicinity of n^+/i contact which increases the effective drift length of holes. The device illuminated through p^+ contact with strongly absorbed light enjoys the advantage of the higher mobility electron which can escape the high density of holes generated near the p^+/i contact. However, for uniformly absorbed light, the hole mobility still limits collection.

Another result of Hack and Shur [34] model is an explanation of the effect of low level boron doping ($\approx 10^{17}$ cm^{-3}). Calculations show that boron doping raises the electric field in the bulk of the i-region near the n^+/i interface by a factor of 2.2 and thereby aids the collections of holes, and reduces recombination in the n^+/i region, where the carrier generation is highest. However, for illumination through the p^+ contact, the reduced electric field does not enhance carrier collection. Another predicted result of boron doping of the i-region is the effect on the open circuit voltage. At high built-in potentials, V_{bi} (defined as the potential difference in the junction region; also equivalent to the diffusion voltage V_d) for the p-i-n diode, the resulting high electric field effectively reduces recombination so that there is negligible improvement due

to boron doping. However, for low built in potentials and electric fields, recombination of holes is significant and boron doping is found to increase V_{OC} as a consequence of the reduced hole recombination current.

More recently, Schwartz et al [35] proposed a numerical model which incorporated the effect of recombination via midgap "dangling" bond states and interface recombination. The distribution of midgap states was assumed to follow a Gaussian distribution. In this model, three paths were assumed to dominate recombination in the p-i-n device; recombination through deep dangling bond states, tail states, and interface states. The participation of both dangling bond and tail states, as recombination pathways, has been confirmed by reference to the intensity dependence of the photo conductivity of annealed and light soaked samples [36]. At low intensity the recombination proceeds through both tail states and dangling bond states, while at high intensities, tail states dominate recombination. However, in light soaked samples, dangling bond density increases, and the increased recombination happens through midgap states. A necessary feature arising from this treatment are relatively low capture cross sections, compared to previous models. As a consequence, the model predicts that different process dominate the solar cell, depending upon the degree of light exposure. Light soaked devices would be expected to be dominated by recombination through dangling bonds and interface states while the initial performance is governed by the tail states. In both cases, however, interface recombination plays a major role.

2. Device Stability

The stability of amorphous silicon solar cells under prolonged light exposure is a major technological problem. Light exposure reduces the performance of p-i-n solar cells in a manner consistent with the degradation of the minority carrier diffusion length and principles of operation discussed earlier. In general, most of the degradation under illumination occurs in

the first 100 hours of operation, and is accompanied by a drop in the efficiency of the solar cells by 10% to 30%. The degradation depends upon the thickness of the intrinsic layer and the cell temperature: at higher operating temperature (e.g.,80°C), the degradation is considerably lower compared to room temperature. The operation conditions also play a role: cyclic illumination (e.g., in a day - night rhythm) shows a lower degradation compared to a continuous illumination (with the same exposure time).

At this time, it is appropriate to describe the physics of instability in a-Si:H solar cells. The photo-generated electron-hole pairs combine in the i-layer of an a-Si:H p-i-n cell, thereby breaking bonds and creating defects. These mid-gap defects act as recombination centers, thereby reducing the lifetime of both electrons and holes. The defects also act to reduce the electric field in the middle portions of the i-layer, particularly near, the maximum power point (i.e. under forward bias). The combination of a reduction in the field, and the reduction in lifetime of the carriers, leads to a reduction in the field-assisted diffusion length or range ($\mu\tau F$) of the carriers where μ is the conductivity mobility, τ the lifetime and F the electric field. The reduction in range leads to a reduction in the carrier collection efficiency, particularly near the maximum power point; i.e. to a reduction in the fill factor of the cells.

Modeling suggests [37] and experiments confirm [38] a substantial difference in the performance of devices illuminated through the p^+ and n^- contacts after light soaking. Because the lower mobility holes limit performance in devices illuminated through the n^- contact, the decrease in the hole diffusion length (L_p) after illumination drastically reduces conversion efficiency. This decrease is evidenced by a reduction in the short wavelength response, since holes must be transported across the i-layer thickness to the p^+ contacts, the long-wavelength response is reduced. However, the conversion efficiency is not as strongly affected because the distance the holes must traverse is relatively small for the bulk of the strongly absorbed radiation. The fill factor and the overall performance of the device is more drastically reduced for the device illuminated through the n^+ contact.

Smith and Wagner [39] have attempted to combine the kinetic description of Stutzman et al [22, 23, 24], with the empirical relationship between device fill factor and the thickness normalized collection length of Faughman and Crandall [33] to bridge the gap between the results of purely material studies and device operation. The additional assumptions of weakly absorbed light and uniform electric field are implicit in the nature of this association. An additional assumption made is that the normalized collection length is inversely proportional to the spin density (N_S). Hence the fine dependent data for N_S are readily transformed to yield the fill factor of the p-i-n diode. The derived relationship with the hypothetical dependence on inverse spin density yields the equation

$$FF(t) = FF_2 - \frac{k_1}{3}\log_{10}\left(\frac{t}{t_0}\right) \tag{1.12}$$

where FF(t) is the fill factor at time 't', FF_2 is the initial fill factor, k_1 is the kinetic rate constant for degradation, t_0 is the initial time, and 't' is sufficiently long that the spin density is much greater than $N_S(t = 0)$. The relationship correctly predicts the semi logarithmic dependence of fill factor on time.

Unfortunately, the empirical nature of the fill factor vs. collection length data and other simplifying assumptions limit the usefulness of the model. For example, the rate of degradation resulting from the treatment is invariant with i-layer thickness. But we know that the thin i-layer devices degrades at a lower rate than thickness.

Although most of the decrease in device performance occurs in fill factor the relationship may also be usefully described in terms of efficiency as [26],

$$\frac{\eta}{\eta_o} = 1.1 - K\log_{10}\frac{t}{t_o} \tag{1.13}$$

where η and η_o are efficiencies at time 't' and to respectively, and K is the rate constant. Devices degrade at a rate K, which depends on i-layer thickness and temperature. In the model of Stutzmann et al [24], the removal of defects was found to be temperature activated process and this also appears to be the care for devices. The rate constant varies with temperature according to

$$K = K' \exp\left(\frac{E}{kT}\right) \tag{1.14}$$

where 'E' is an activation energy and 'K' is a constant proportional to thickness [26]. A 35°C the rate constant varies as

$$K = 0.165 d^{0.54} \tag{1.15}$$

where 'd' is the i-layer thickness in microns, this design may be used as a predictive tool to determine the long term performance of a given solar cell design. Stacked junction cells are a more complex case because of the lower illumination intensity and differing bias conditions that occur within the multifunction device. Experimentally one sees a rate of degradation which appears to be the average of the rates of the individual p-i-n diodes. Benett and Rajan [37] have confirmed this finding. Thus, we may expect a stacked cell; which is usually comprised of one or more extremely thin ($\approx$ 1000°A) i-layer device, to exhibit far better long term stability and efficiency than their single function counterparts, and experimental measurements have confirmed this.

C. Growth Chemistry

Growth chemistry plays a major role in the deposition of high quality material using plasma deposition [40]. A-Si:H is generally grown on a foreign substrate. Therefore, for initial layers, there is no template which dictates the growth of a suitably ordered Si layer. Rather, it is likely that many islands of a-Si:H growth are started, and they may coalesce in to homogeneous structure after some thickness has been deposited. In this sense, a-Si:H grows like any other material. In line with any heterogeneous growth, we would expect that the initial layers of a-Si:H are possibly the worst layers in terms of the structure, H bonding and homogeneity. And yet, in a superstrate device made directly on a foreign (tin oxide) substrate, the most critical layer of a-Si:H, namely the p-layer and the p-i interface, are the worst layers from a structural view point. This fact may have something to do with the instability observed at the p-i interface in most a-Si:H devices.

Once the a-Si:H layer starts growing in a homogeneous fashion, away from the substrate, a growing surface may be represented as shown in Figure 1.4. There, we schematically show a H-terminated a-Si:H, a very likely event, given the strong Si:H bond strength (300 kJ/mole). To build a layer of a-Si:H on this surface, first the hydrogen has to be eliminated, and then, a radical such as SiH_3 or SiH_2 gets inserted in to the growing surface. Therefore, we need, preferably, an excess of atomic hydrogen to extract the H from the surface, a likely reaction given the high bond strength of H-H radicals (435 kJ/mole) and we need a radical for insertion. This is a stage where a wrong growth technique can give a poor film. If the growth chemistry produces only one kind of radical, either SiH_2 or SiH_3, the surface would grow by insertion of either of radicals into the surface bond (see Figure 1.4). However if both types of radicals are present, then both can insert themselves and we end up with a surface after insertion which looks as in Figure 1.4b, where part of the surface is terminated with an H (insertion of SiH_3) and part is not (insertion of SiH_2). Therefore a

uniform surface has now been converted into a non uniform surface. The consequence of such a mixed mode can only increase the surface roughness, since the type A site (one without H) can immediately accept a radical, but type B needs a H elimination before accepting a radical. Indeed, computer simulations and experiments show that having significant concentrations of SiH_2 in plasma leads to increased roughness of the surface. From this basic argument, one would want excess H and only one type of radical predominating in the chemical growth technique. Fortunately, having excess H around assures that both these events take place. In a highly H diluted plasma the likely reaction leading to fractionation of Silane is

$$SiH_4+H \longrightarrow SiH_3+H_2 \qquad (1.16)$$

The next logical step in improving the material beyond H dilution is to further use Hydrogen plasma chemistry during growth. In particular, the bond strengths of Si-Si and Si-H are so similar, one can argue that the weaker Si-Si bonds present in highly disordered a-Si:H may be etched away by H during growth, leading to an intrinsically more stable material. For this to happen, we need high energy, high density of H in the discharge. Our ECR reactor is one way of achieving such energetic and high density H. Appropriate H etching can also reduce the void structure. Thus, in principle, the ECR discharge can provide H to do etching during growth.

The next logical step in improving the film would be to improve the surface mobility of radicals such as SiH_3. One way of increasing the mobility would be to increase the growth temperature, to say 350 - 400 ^oC. However, at such high temperatures, the few SiH_2 bonds in

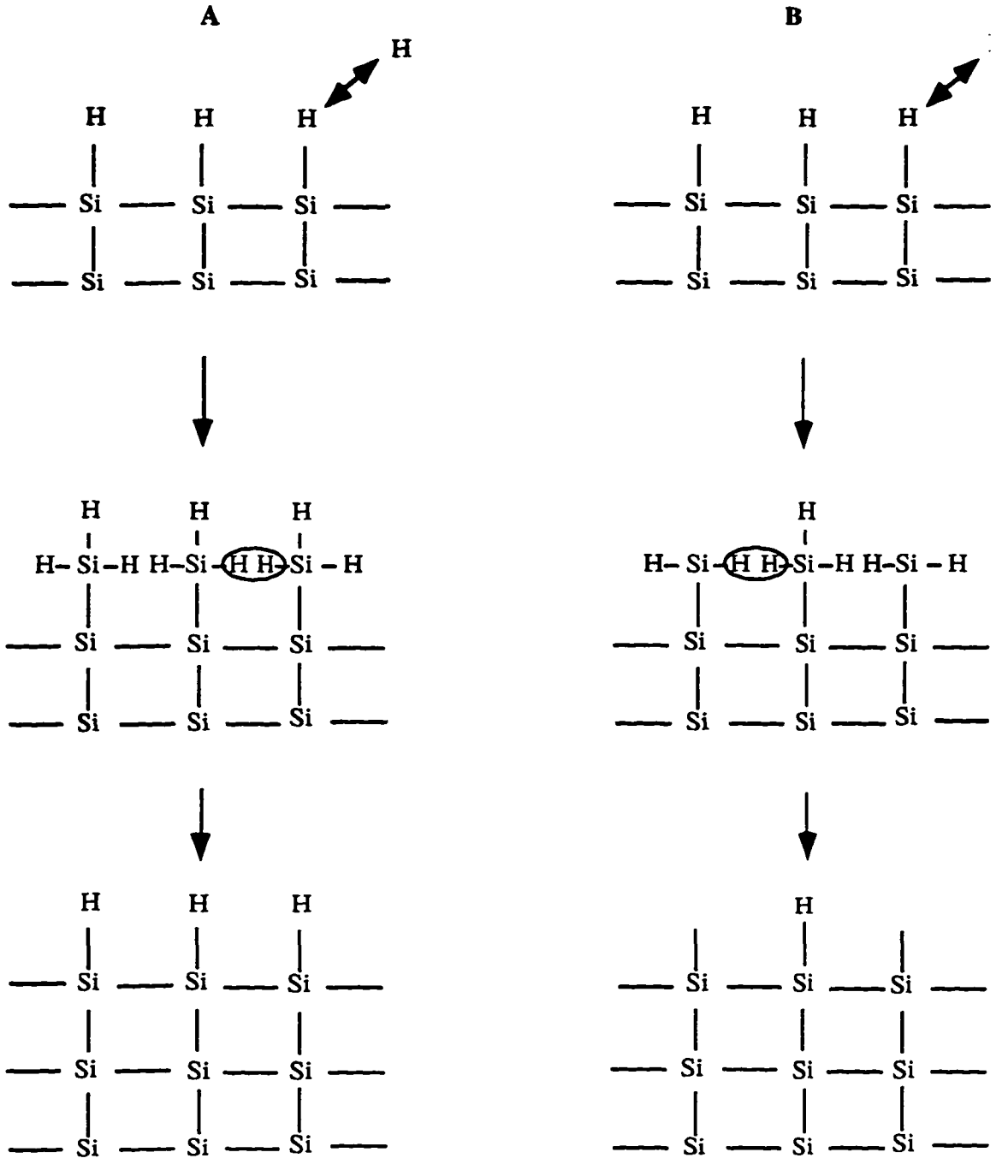

Figure 1.4. Steps in the growth of a-Si films [40].

the material may break, unless there was an excess of atomic Hydrogen around, which would then re-form the bonds. Once again, the ECR discharge, with its high density of excited H radicals and ions coming to the surface, will help in improving the bonding at higher temperatures.

Note that if we used a highly diluted helium discharge instead of Hydrogen discharge, there would be none of the beneficial etching of H but there would have been more ion bombardment effects. Thus a high He dilution would assure that the growth took place from SiH_3, since the most likely collision would be between SiH_4 and He, leading to fractionation of SiH_4 into SiH_3 and H. There would be little opportunity for SiH_3-SiH_3 collisions, which can lead to the formation of disilane and higher polymers. Since He does not do any chemical etching, the bandgap of a-Si:H produced from He discharge should be lower than the bandgap produced from a Hydrogen discharge, since during the etching phenomenon, the weakest states, those at the top of the valence band, get etched away, and the band gets pushed down in energy.

II. SAMPLE PREPARATION

In recent years electron cyclotron resonance (ECR) plasma sources have been widely explored in various plasma and ion beam technologies. The growing interest in ECR CVD technology is motivated by unique features of ECR plasma which are superior to those of conventional RF plasma source used in PECVD. Some of the most promising ECR plasma CVD characteristics and features are briefly listed below:

1. Low gas pressure: Typical ECR operational pressure 10^{-4} - 10^{-2} Torr, while RF plasma pressure are 10^{-2} - 5 Torr. Such low pressure allows to avoid undesirable homogeneous reactions in volume. At pressure below 1m Torr, ion mean free path is larger than source and stream dimensions. Thus by controlling the ECR plasma potential and magnetic field profile one can regulate the energy of ions oncoming to the substrate.

2. Low ion energy: V_i = 10 - 50eV. The ion bombardment with this energy is extremely important for the growth of the film with good micro structure and other mechanical properties.

3. High ion density at wafer location, $N_i > 10^{11}$ cm^{-3}. At the same power level, RF plasmas have densities of ten times lower, $N_i = 10^{10} cm^{-3}$.

4. High degree of gas decomposition and high concentration of excited species and radicals involve in film formation. This improves the gas utilization and dramatically increases the film growth rate.

5. Separation of plasma generation zone from the sample (wafer) stage. This allows one to independently control the energy of charged particles (ions and electrons) bombarding the sample.

6. Controllability of energy of ions bombarding the substrate by varying of magnetic field and it structure.

7. Low ion energy spread.

The slow path in the "industrialization" of ECR technology is associated with some factors which are not purely technological:

1. Complexity of the system (often two vacuum chambers, two or three magnetic coils and/or permanent magnets, bulky microwave transmission line).

2. High equipment cost compared with that of RF CVD and LPCVD systems (expensive turbo-molecular pumps, coil and microwave power supplies).

3. Large size and weight of the whole system compared with those of RF plasma systems.

There are many technological problems which are common for ECR plasma systems and have not been solved yet. Among these are:

1. Control of film uniformity, in particular across large area wafers of 15-20 cm diameter.

2. X-ray radiation from ECR plasma which could be a source of film structural damage.

3. Relatively low (compared with that of RF CVD and high temperature LPCVD) film deposition rate limited by low operational pressures, 0.1 - 30mTorr.

4. Particulation from flaky film deposited on the process chamber walls.

To solve these and other problems, extensive research of ECR plasma's and deposition process chemistry is in progress.

All samples reported in this study were deposited by using a ECR plasma deposition system. In the next few sections we shall discuss the underlying principle behind the working of this system, physical design of the system and the PECVD processing resulting in the growth of a-Si:H thin films and devices.

A. Deposition System

1. Fundamentals of ECR Process

The first step in the design of an ECR plasma deposition system [41] is an understanding of the plasma source. There are several different possible arrangements for ECR sources. Variations occur in system size and shape, method of microwave introduction, and the number, position, and type of the magnets [42]. The most commonly used arrangement is the Hitachi/NTT type ECR source shown in Figure 2.1. The plasma source is a stainless steel tube with two coils around it which are used to generate a uniform DC magnetic field. Microwaves are introduced through a quartz window on one end of the tube. The plasma is extracted from the other end of the tube.

In order to understand the plasma generation process, it is best to start with an overly simplified model. Free electrons in the plasma generation region spiral around the static magnetic field lines due to the Lorentz force. In Appendix A, it is shown that the frequency of the rotation (gyrotron frequency) is given by

$$\omega_0 = \frac{qB_z}{m_e} \tag{2.1}$$

and the radius of the spiral is given by

$$R = \left(\frac{m_e}{qB_z}\right)\sqrt{v_x^2 + v_y^2}\,. \tag{2.2}$$

The basic principle of ECR heating is illustrated in Figure 2.2. Linearly polarized microwaves enter the region propagating along the axis of the static magnetic field. Linearly polarized plane waves may be equivalently expressed as two circularly polarized waves rotating

in opposite directions. For example, the electric field of the linearly polarized microwaves, which can be expressed as

$$\mathbf{E} = E_0 \cos(\omega t)\mathbf{a}_y \tag{2.3}$$

may also be written as

$$\mathbf{E} = \mathrm{Re}\left[\frac{E_0}{2}(\mathbf{a}_y + j\mathbf{a}_x)e^{j\omega t} + \frac{E_0}{2}(\mathbf{a}_y - j\mathbf{a}_x)e^{j\omega t}\right] \tag{2.4}$$

where the first component in the bracket is a wave with right-hand circular polarization (RCP) and the second term is a wave with left-hand circular polarization (LCP).

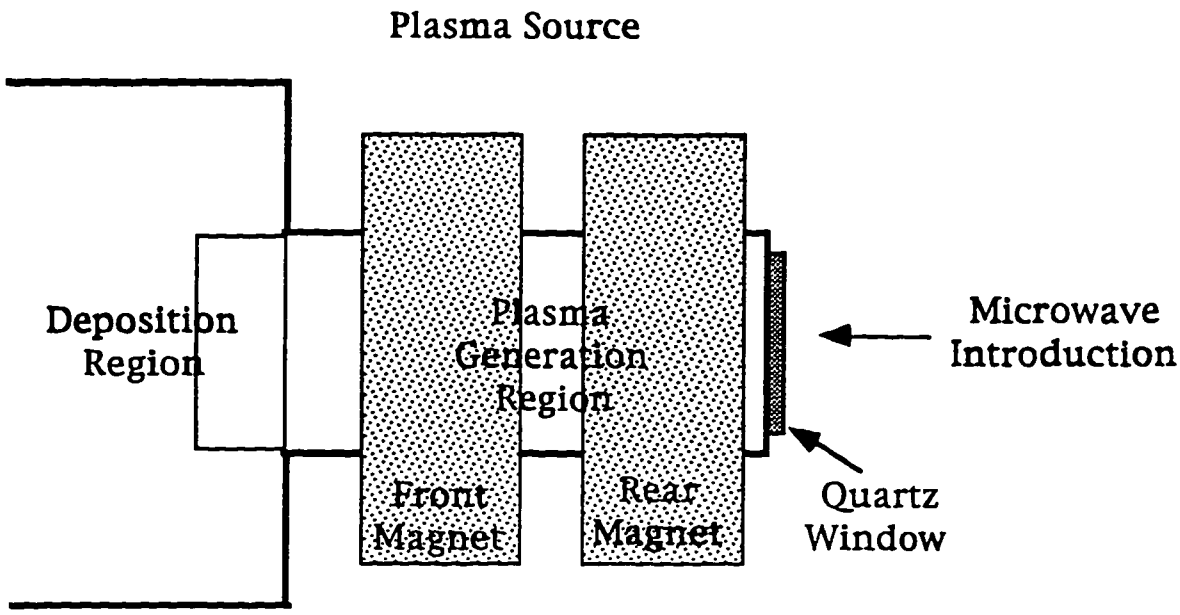

Figure 2.1. Typical arrangement for a Hitachi/NTT type ECR source.

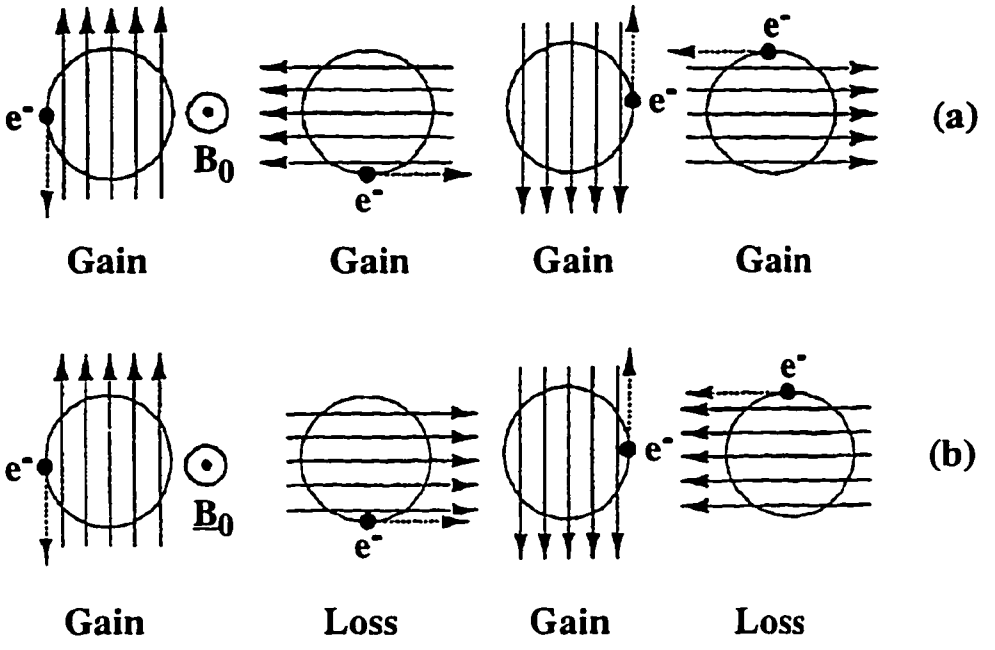

Figure 2.2. Basic principle of ECR heating: (a) continuous energy gain for right-hand polarization; (b) oscillating energy for left hand polarization.

When the gyrotron frequency and the frequency of the microwaves are the same, the electrons and the electric field vector of the RCP waves are rotating in phase with each other. This is the electron cyclotron resonance condition. The energy of the RCP microwaves goes into accelerating the electrons. The electrons then collide with neutral gas molecules, causing ionization and the formation of free radicals. Since the electrons and the LCP electric field vector are rotating in opposite directions, electron cyclotron resonance can not be the method of microwave power absorption for the LCP waves. In fact the LHP wave field produces an oscillating force whose time average is zero, resulting in no energy gain. Other possible energy loss mechanisms must be looked into for the LCP microwaves. There are many rather complex theories regarding the absorption of the LCP waves. The important result that comes out of the theories is that when the plasma density gets large enough, the LCP waves are

almost completely absorbed. The point where this occurs is called the critical density, N_{cr}. When the density of the plasma exceeds N_{cr}, the microwaves are no longer able to propagate through the plasma (the amplitude decreases exponentially). By solving Maxwell's equations, the critical density is determined to be

$$N_{cr} = \frac{\omega^2 \varepsilon_o m_e}{q^2} \tag{2.5}$$

which results in a critical density of 7.5×10^{10} cm^{-3} for the 2.45 GHz used in this work.

2. Description of ECR reactor

The reactor used in this study is shown schematically in Figure 2.3. It consists of a microwave source operating at 2.45 GHz, which feeds power through a 3-stub tuner into a cavity. This multi screw tuner is used to match the source to the load through the dielectric

window, achieving a condition of low reflected power. The cavity has a quartz window to let in microwave power. The axial magnetic field to create the ECR condition is produced using two coils, whose relative position and magnetic field strengths are controllable by the operator. The magnetic field needed for ECR resonance is determined by the following relationship

$$\omega_o = \frac{qB_z}{m_e} \tag{2.6}$$

It is about 875 Gauss for 2.45 GHz microwaves. Two DC power supplies (10V, 200A) are used to power the magnets. A typical profile of the magnetic field strength is shown in Figure

2.5. Thus, the position of the resonance plane can be changed by us and generally, we set it so that resonance plane is about 20 - 30 cm away from the substrate.

The plasma gases hydrogen and helium are introduced into the microwave cavity near the source end. Silane or Germane (process gases) are introduced near the substrate through a separate manifold. The typical pressures used for growth are in the range of 10 - 15 mT. At these pressures, the excited H radicals have a long mean free path and they arrive at the substrate with significant energies. A simple optical emission spectroscopy (OES) system detects the presence of these radicals by looking at emission coming from a region near the substrate. The typical OES spectrum of a hydrogen plasma is shown in Figure 2.4. The peaks at 656 nm and 610 nm are noteworthy, and they represent respectively, H_α and H_2 emission lines. The intensities and relative ratios of these lines, change as we change the plasma conditions, thereby providing us with some information about the nature of the chemical species arriving at the substrate as we change the plasma conditions.

B. PECVD Processing

Chemical vapor deposition (CVD) consists of a thermally activated set of gas-phase and surface reactions that produce a solid product at the surface. In plasma enhanced chemical vapor deposition (PECVD), the gas phases and often the surface reactions are controlled or strongly modified by the plasma properties. In place of thermal activation in CVD, the critical initial step in PECVD is electron impact dissociation of the feed stock gas. Since $T_e \approx 2$ - 5eV in a low-pressure discharge easily suffices for feed stock dissociation and since T_e is much greater than the substrate temperature, the deposition can be carried out at temperatures much lower than for CVD. One hundred percent (undiluted) silane gas (SiH_4) is used as the process gas for all the amorphous silicon films. For most of the processing SiH_4 is diluted inside the

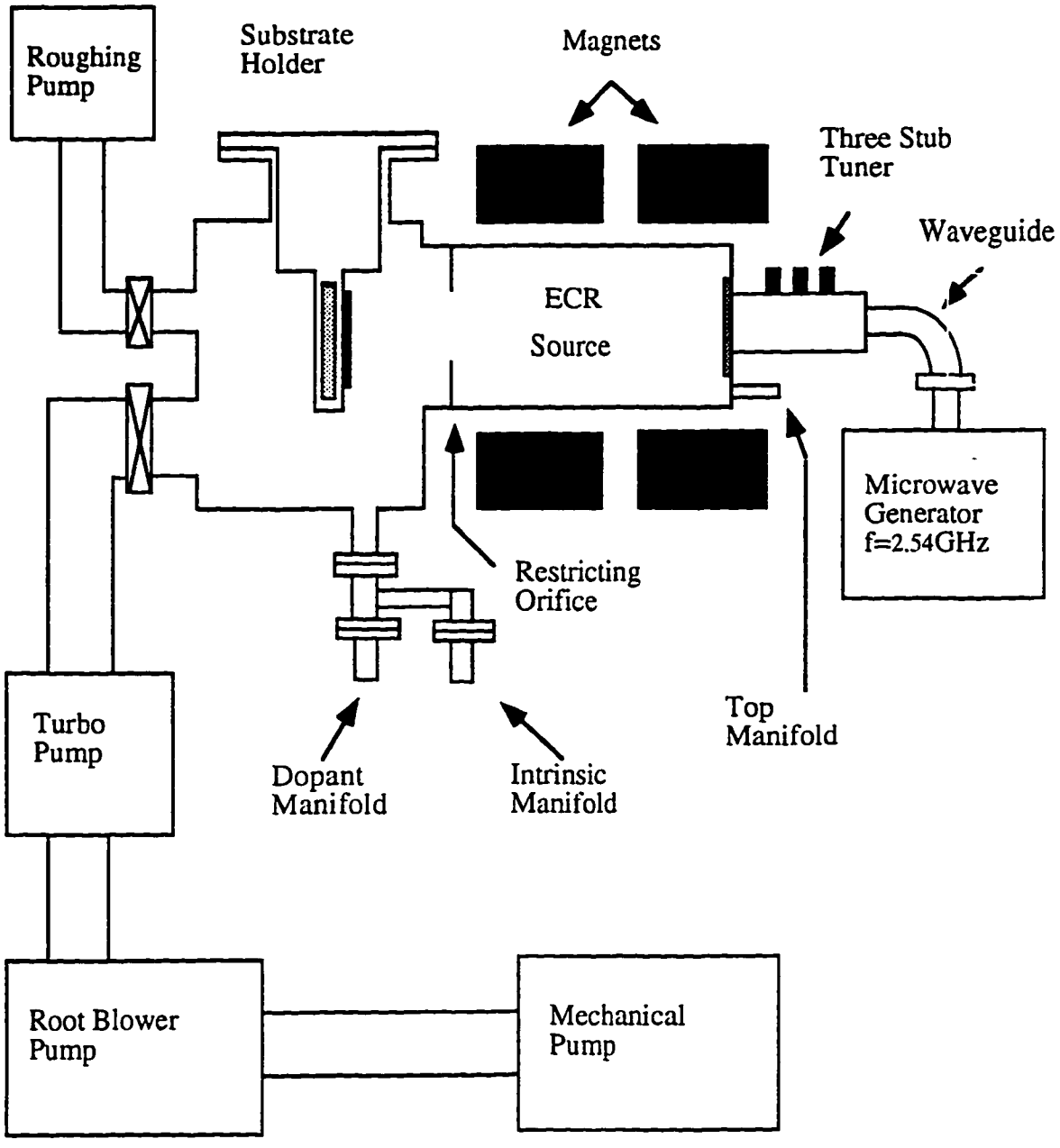

Figure 2.3. Diagram of the ECR-CVD system.

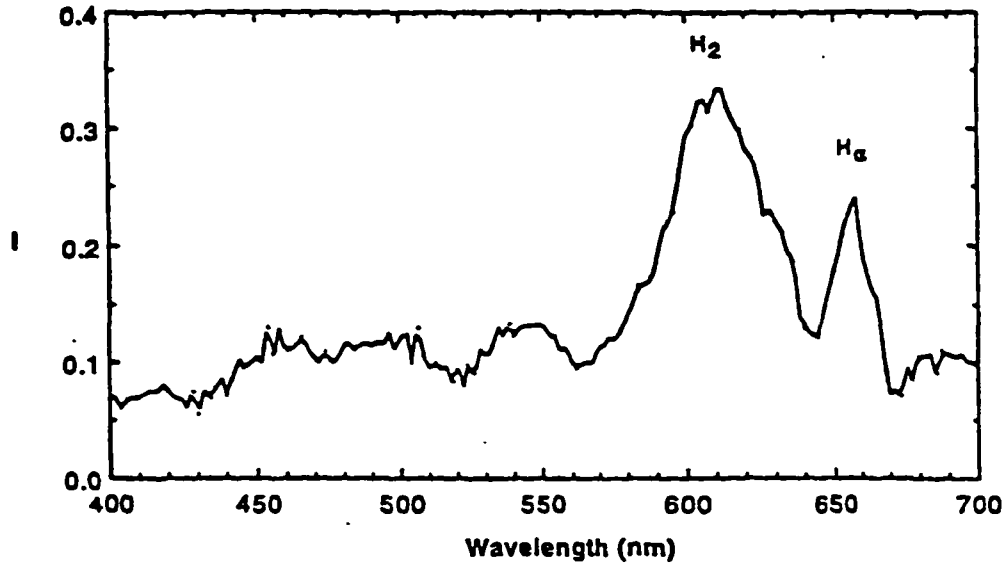

Figure 2.4. OES spectrum of ECR plasma [43].

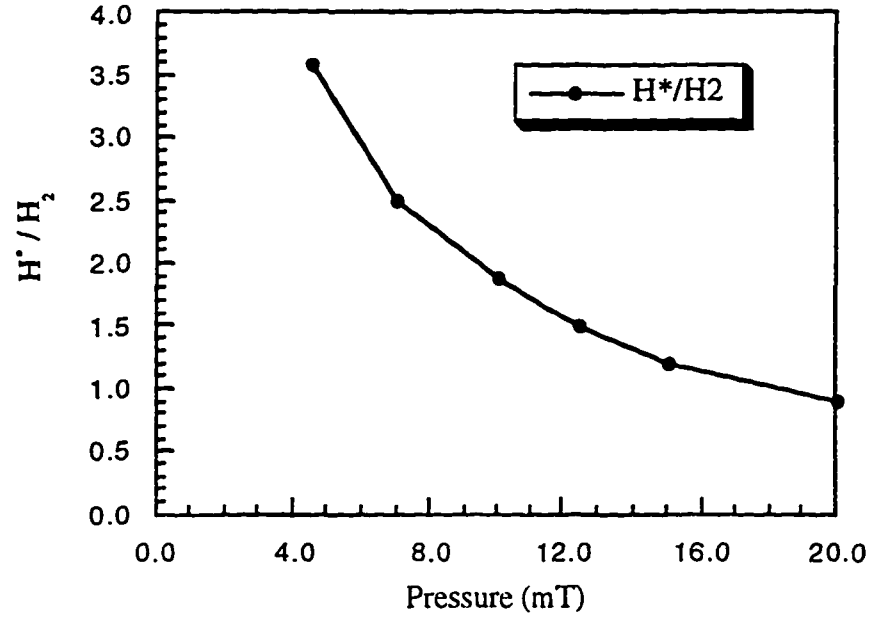

Figure 2.5. Influence of pressure on H^*/H_2 [43].

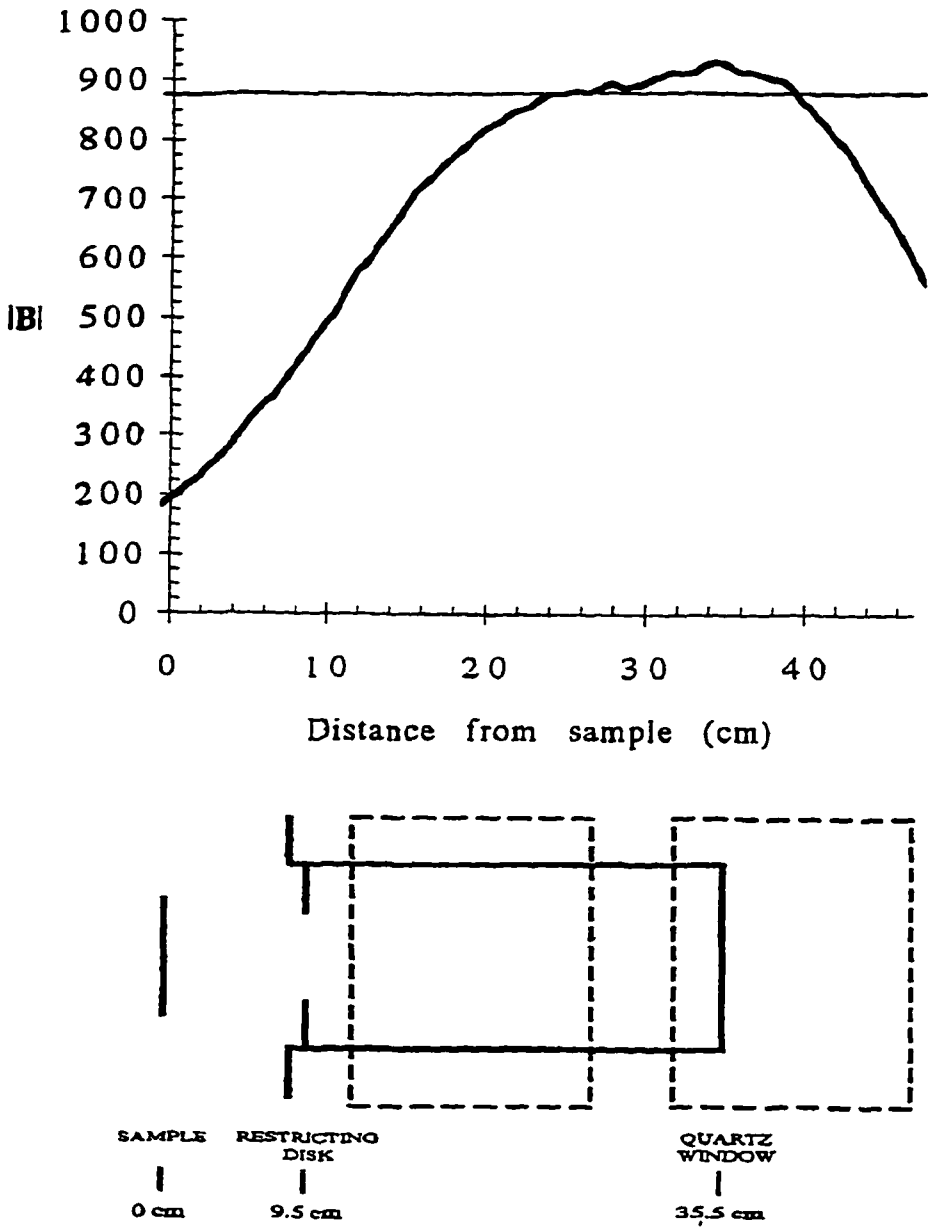

Figure 2.6. Magnetic profile present in the system during growth. This profile is made for I_{source} =183 Amps and $I_{chamber}$ = 178 Amps.

deposition chamber with hydrogen. The concentration of each atomic species incorporated into the material depends on the gas flow ratios of the precursor gases into the chamber, which is monitored by mass flow controllers. All of the depositions are done at low temperature (< 400 °C) to prevent thermally activated deposition. The substrate is heated to increase the mobility of hydrogen at the surface, which increases the passivation of dangling bond defects. Also, the thermal energy supplied to the growing surface helps to reduce the number of weak silicon bonds incorporated into the amorphous network by breaking these bonds before they become buried.

All the films for material characterization was deposited on cleaned 7059 corning glass substrates consisted of boiling for ten minutes in detergent and then in acetone and methanol solution. The devices were made either on conducting tin oxide in case of superstrate cell or on polished stainless steel in case of substrate solar cell.

Once the substrates are loaded into the reactor chamber, a system cleaning process is completed. The chamber is first pumped out with mechanical pump and then by the turbo pump through the gate valve. Then a series of gas purges with nitrogen, argon and silane are done to help remove any remaining moisture from the system. The substrate is then heated to a temperature that is at least 50°C higher than the intended deposition temperature to include outgassing of impurities from substrate and its holder.

A cleaning plasma is then lit immediately using silane and hydrogen. This cleaning plasma will etch impurities from the chamber walls and deposit a fresh layer of a-Si:H on all surfaces. A shutter is placed between the plasma and substrate to prevent deposition on the substrate.

In Figure 2.5 we show that what happens to the ratio of 656 nm to 610 nm lines as we decrease the pressure. Quite clearly, lower pressures, the relative intensity of the Hα line increases, implying that more H atoms and particularly more enegetic H atoms, are arriving at these pressures.

We call our process a remote reactive plasma beam deposition process. The term remote is used to emphasize the fact that the main plasma is remote from the substrate, and that the radicals such as H and excited molecules and ions such He^* generated by the ECR plasma are playing a role in the deposition. At low pressure, clearly silane can and does diffuse back into the plasma zone. However, since the mean free path of salyl radicals at these pressures is low (of the order of 1 cm or lower) these radicals do not play a role in growth on the substrate. Rather, the salyl radicals generated near the substrate by the fractionalization of silane upon reaction with either H or excited He give rise to growth, as explined in the section of growth chemistry.

The entire ECR system is pumped by a turbo-molecular pump, even during growth. The base vacuum is in the 3 - 5 x 10^{-8} T range. The gases for doping are introduced near the substrate through a separate manifold. This way, cross contamination of the i-layer by dopant gases flowing through the same manifold is avoided. Thus, we have three manifold, one for the plasma gases, one for the i-layer gases, and one for the dopant gases. Each manifold has a valve near the system which can be shut-off so that cross-contamination between manifolds is avoided.

The substrate is tightly mounted on a polished substrate holder with a thick stainless mask, and heated by heating up the substrate block from the outside using calibreated versus the heated block temperature, and generally is about 30 - 40°C lower than the block temperature for typical pressure, gas flow and plasma conditions we use.

III. CHARACTERIZATION

A. Plasma

1. Langmuir Probe Theory

An important step in characterization of the ECR system is the understanding of the plasma parameters [41] and the dependence of these parameters on the other system variables (microwave power and chamber pressure).

A plasma is defined as [44] "A conglomeration of positively and negatively charged particles which is on the average neutral due to the equal number density of the positive and negative charges. A plasma may contain neutral particles or it may be fully ionized. The ions may be singly or multiply charged and they also may be atomic or molecular." The fact that the plasma is neutral on the average is usually referred to as quasi-neutrality.

Langmuir probes are the simplest and most commonly used technique for determining the important plasma parameters. The procedure simply involves placing a metal probe in the plasma, and measuring the I-V curve between the probe and the vacuum chamber (ground potential). The setup for the Langmuir probe measurement is shown in Figure 3.1. The langmuir probe theory depends on the plasma being relatively unaffected by the insertion of the probe. When the probe is placed in the plasma, a region called the sheath forms around it. In this region the quasi-neutrality condition is not valid (excess charge densities build up). The size of the sheath for a given probe bias depends on the Debye shielding length in the plasma,

$$\lambda_D = \left(\frac{kT_e}{4\pi N_e e^2} \right) \tag{3.1}$$

where T_e is the electron temperature and N_e is the plasma density [45]. One assumption used in the plasma parameter calculations is that the sheath width is small compared to the probe dimensions. This assumes that all the particles entering the sheath will be collected by the probe.

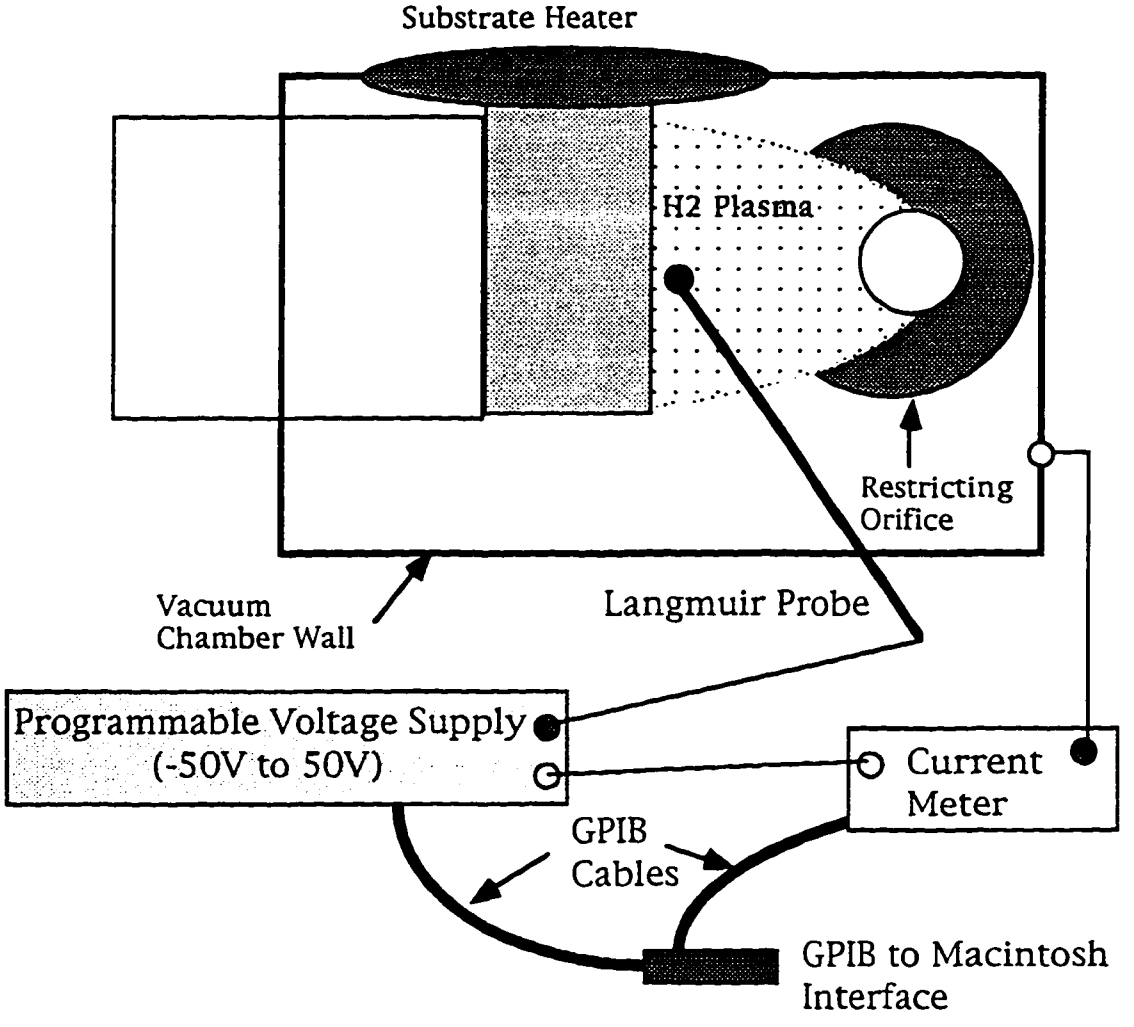

Figure 3.1. Setup for Langmuir probe measurement [41].

The other conditions on the Langmuir theory are: the electron velocity distribution must be Maxwellian, magnetic fields present must be less than approximately 200 Gauss, and the mean free path is much larger than probe dimensions [45].

2. I-V Curve Generation and Interpretation

The setup for the Langmuir probe measurement is shown in Figure 3.1. A BASIC program on the Macintosh is used to control a DC voltage supply via the IEEE 488 interface. The current is measured by a HP DMM and sent back to the Macintosh on the GPIB. The I-V data is sent to an Excel spreadsheet which calculates the plasma parameters.

The probe used in these measurements is a disk with an area of 0.512 cm^2. The back of the disk is insulated with boron nitride so that the only part of the probe that is exposed to the plasma is the front face. A typical plasma I-V curve is shown in Figure 3.2.

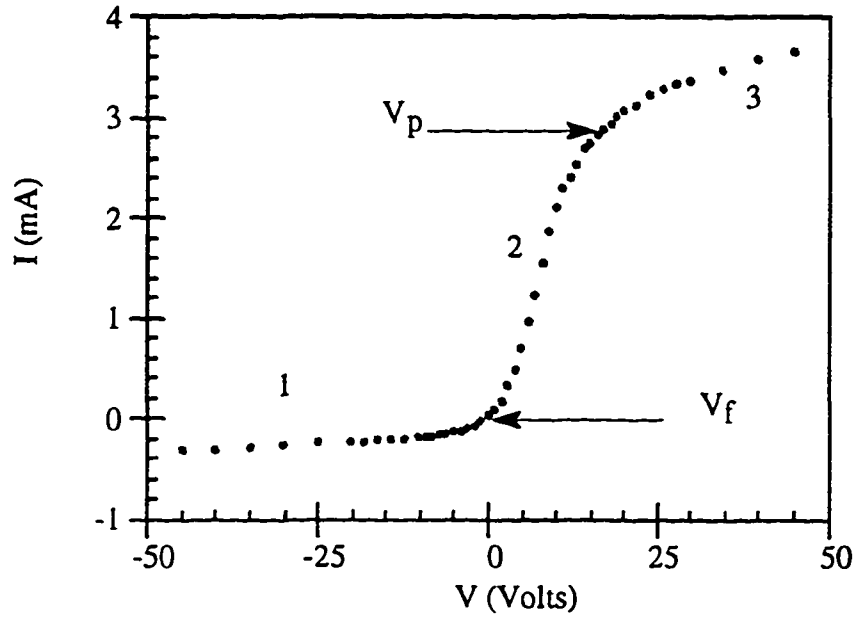

Figure 3.2. Raw data from a Langmuir probe measurement [41].

The three regions which have been labeled in the figure are:

1) Ionic region

2) Transition region

3) Electronic region

At large negative voltages (region 1-Ionic region), almost all of the electrons are repelled and the ions are attracted, causing the current in this region to be due purely to ions. A layer of positive charge due to the ions builds up until it has the same magnitude as the negative charge on the probe. This layer of charge is the sheath that was described previously. Outside of this sheath, there is very little electric field, so the plasma is not disturbed. The current is due to the random thermal motion of the ions carrying them into the sheath. Ideally, if the area of the sheath remained perfectly constant, region 1 would be flat. In practice, it turns out that the ionic region is linear with a very small slope.

At large positive voltages (region 3-electronic region), the ions will be repelled and the current will be due primarily to electrons. In this case, a negatively charged sheath, due to the attracted electrons, forms around the probe.

Region 2 is called the transition region since it connects the region where ion current dominates to the region where the current is purely due to electrons. The division between the electronic region and the transition region occurs at the plasma potential, V_P, which is defined as the voltage at the knee of the curve.

When the probe is at the same potential as the plasma, no electric fields are present due to the probe. This potential is called the plasma potential. The plasma potential is often used as an estimate of the ion energy. The current at V_P is due to the particles which hit the probe as a result of random thermal motion. The thermal velocity of electrons is much larger than the thermal velocity of the ions due to the electrons smaller mass. This results in the majority of the current collected at the space potential being due to electrons.

Another physically meaningful point in the transition region is the floating potential, V_f. The floating potential is the voltage where the current goes to zero. At this point, the voltage has been decreased from the plasma potential and enough electrons have been repelled to allow the ionic and electronic components of the current to exactly cancel.

3. Determination of Plasma Parameters

Once the plasma I-V curve has been generated, several useful plasma parameters can be extracted. The electron temperature, electron density, plasma potential, and ion current density are all easily determined [46]. The electron current can be isolated from the ion current by fitting a line to the ion current in region 1 and subtracting it from the total current ($I_e = I_T - I_i$) in all three regions. If we assume that the electron distribution is Maxwellian, the velocity is given by

$$\bar{v} = \sqrt{\frac{8kT_e}{\pi m_e}} \tag{3.2}$$

and the electron current is given by

$$I_e = \frac{AqN\bar{v}}{4} = \frac{AqN_0\bar{v}}{4} e^{\left(\frac{-qV_B}{kT_e}\right)} \tag{3.3}$$

where N_o is the electron density in the undisturbed plasma, V_B is the potential barrier seen by the electrons, T_e is the electron temperature, and A is the area of the probe [45]. As the potential is reduced from V_P towards V_f, the potential barrier, V_B, increases and fewer electrons make it to the probe. The electron temperature can now be determined by plotting

$\ln(I_e)$ vs. V as shown in Figure 3.3. The graph is linear in the transition region with a slope = $1/T_e(eV)$.

The determination of the plasma potential can be a large source of error. In order to be consistent, we have developed a standard procedure for determining V_P from the $\ln(I_e)$ vs. V graph. First a linear fit is made to the transition region without including the knee and to the electronic region without including the knee. The intersection of these two lines is the plasma potential. This procedure is illustrated in Figure 3.3.

The electron density in the plasma can be determined by using Equation 3.3 at the plasma potential (Area Sheath = Area Probe, $V=V_p$, $I=I_{eo}$). This results in the expression for the electron density given in Equation 3.4.

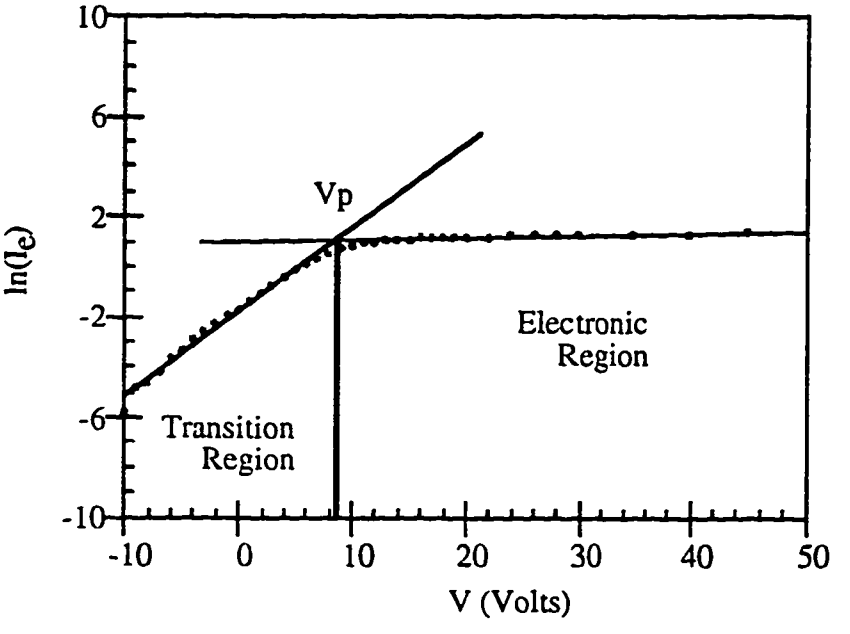

Figure 3.3. Langmuir probe data with the ionic component subtracted out [41].

$$N_e(cm^{-3}) = \frac{I_{eo}}{qA}\sqrt{\frac{2\pi m_e}{k_B T_e}} = 3.73x10^8\left[\frac{I_{eo}(mA)}{A(cm^2)\sqrt{T_e(eV)}}\right] \qquad (3.4)$$

The ion current density is determined by using the current at zero volts and the probe area.

$$J_i = \frac{I_i(V=0)}{A} \qquad (3.5)$$

B. Materials

1. Film thickness

The thickness of the semiconductor films deposited on glass substrates were measured using two different techniques. Primarily all of the film thicknesses were measured using Lambda-9 dual beam spectrophotometer. The interference peaks measured over the wavelength range of 1000 nm to 2500 nm were used to calculate the thickness using the following relationship

$$t = \frac{\lambda_1\lambda_2}{an(\lambda_1 - \lambda_2)} \qquad (3.6)$$

where a=2 for peak to peak intervals and a=4 for peak to valley intervals. The refractive index 'n' of the film was found out from reflection spectra using the following relationship:

$$n = \sqrt{n_s n_a \frac{1 + \frac{n_s - n_a}{n_s + n_a}\sqrt{\frac{R_{max}}{R_{min}}}}{1 - \frac{n_s - n_a}{n_s + n_a}\sqrt{\frac{R_{max}}{R_{min}}}}} \qquad (3.7)$$

where n_a is the refractive index of air, n_S is the reflectance of a maxima and a minima in the non-absorbing region (1000 nm < λ < 2500 nm). The index of refraction 'n' will vary with the 'Ge' content and is assumed constant over the range of the wavelength used. Because of the above assumption the thickness measured is accurate only to about ± 0.1μm.

We also used a Sloan Dektak Stylus to cross check the optical thickness measurements on several of our samples. Good agreement between the two methods was obtained.

2. Photo and dark conductivity

Because they are both important and easy to measure, photo and dark conductivities (σ_l and σ_d) are usually amongst the first set of properties measured, to characterize the electronic of the films.

Free carriers (electrons and holes) in a semiconductor reach their thermal equilibrium concentrations through a balance between the thermal generation and recombination processes. These free carriers with equilibrium concentrations n_0 and p_0 contribute to conductivity of the material as,

$$\sigma = q n_0 \mu_n + q p_0 \mu_p \qquad (3.8)$$

where μ_n and μ_p are electron and hole mobilities respectively. An estimate of the position of Fermi level can be made from the temperature dependence of conductivity. The formula for $\sigma(T)$ can be obtained from the Fermi statistics for electrons and holes densities as

$$\sigma_{n,p} = \sigma_o \exp\left[\frac{-\left(E_{c,v} - E_{fn,p}\right)}{KT}\right] \tag{3.9}$$

where $E_{c,v}$ is the conduction or valence band edge defined by the mobility gap, $E_{fn,p}$ is the quasi-Fermi level and σ_0 is the conductivity prefactor known as the minimum metallic conductivity. The above approximation is true if the mobility is only a weak function of temperature and if the presence of deep levels does not alter the occupation of band states too severely. The Fermi energy E_f can be extracted from an Arrhenius plot of the logarithm of the conductivity over a temperature range (80 to 200°C). A linear plot of $\log\sigma$ vs. T^{-1} could indicate either band-like conduction beyond a sharp mobility edge or phonon-assisted hopping between nearest-neighboring localized states. Alternatively, a concave upward $\log\sigma$ vs. T^{-1} plot could reflect either the absence of a sharp mobility edge or the predominance of variable-range hopping conduction. The upper limit of temperature is kept below 200°C to limit changes in band structure. Also, to prevent the photogeneration of charge carriers, the above measurement is performed in a closed dark environment.

Photoconductivity occurs when carriers are optically excited from non-conducting to conducting states. It relates to the photogeneration, transport and recombination of electrons and holes. The illumination excites electrons and holes to the band edges where they drift towards electrodes under the applied field. σ_l normalized against the actual amount of light absorption is equal to the product of the quantum efficiency, mobility and recombination lifetime ($n\mu\tau$) for majority carriers. The ratio of room temperature photo and dark conductivity known as photosensitivity is also an important measurement for finding out the

film property. Photo and dark conductivity measurements were made in a setup designed here at the Microelectronics Research Center (MRC). The measure photoconductivity the sample is placed on the base and the probes are connected to the sample contacts. A voltage of 100V is applied across the sample. The photo and dark conductivity is determined using the following relation:

$$\sigma_{d,l} = \left(\frac{W}{L}\right)\frac{I}{V \cdot d} \qquad (3.10)$$

where (L/W) is the length to width ratio of the metal contact which in our case is 20, 'd' is the thickness of the film and V (= 100V) is the applied voltage across the contacts. Since the light intensity is the same for all samples, the photosensitivity is an indication of how well the material can collect the photogenerated carriers.

3. Sub band gap absorption

Sub band gap absorption measurement can be used to get a first hand idea of the quality of films. The curve of absorption coefficient α versus photon energy hv yields a joint valence band-conduction band density of states, when one makes the usual assumption that the matrix element for absorption is independent of hv. However, for use of this technique to obtain the information about sub-gap states requires the measurement of low α (0.1 to 10cm^{-1}). In amorphous semiconductors such as a-Si:H alloys which are usually prepared as thin films of thickness on the order of 10μm or less, the thin film geometry limits the accurate determination of α from optical transmission and reflection data to $\alpha \geq$ 1000cm^{-1}. Thus in such cases indirect measurements that determine the spectral absorption-such as electroabsorption, photoacoustic spectroscopy (PAS), photothermal deflection spectroscopy (PDS), and constant

photocurrent method (CPM) have greater sensitivities to determine the defect state densities. Amongst these PDS is the most commonly used technique. But PDS is very surface sensitive, which is a severe disadvantage if the behavior of the surface is different from that of the bulk.

To measure the sub-gap absorption coefficient α, we have used a two-beam photoconductivity technique developed by Wronski and co-workers [46]. This approach involves the use of a high intensity dc beam of light which is always incident on the on the sample and a second low intensity ac light source. The dc beam continuously creates electron-hole pairs that keep the midgap states (traps) filled and keeps the occupancy of the mid gap states unchanged. The ac beam superimposes on the dc beam and thus modulates the photocurrent generated in the sample by creating additional electron-hole pairs.

The change in photocurrent produced in the sample as we change the energy of this ac beam can be detected by a lock-in amplifier and can be related to the absorption coefficient of the film.

The schematic of the apparatus is as shown in Figure 3.4. In this set up, the monochrometer is used to change the wavelength of the incident photons. The range of wavelength that is incident on the sample in this measurement is from 600nm to 1100nm. The output of the monochrometer is chopped.

The chopped beam is focused on to the sample through a beam splitter, the other half of which goes to a photodetector used as a reference cell. This reference cell is used to determine the photon flux incident on the sample at each wavelength. The chopper modulates the photon signal to produce a 13.5Hz square wave. This operation reduces the noise due to the ambient light and 60Hz power lines. A high pass filter is also used at $\lambda \geq 700$nm to get rid of photons of lower wavelength. The sample is provided with coplanar contacts, usually of Cr or Ti. To minimize errors due to scattering etc. [47], the contacts are 0.2mm apart. The sample is provided with a dc bias voltage of 20V, and the ac current through the sample is detected using a tuned pre-amplifier and a lock-in amplifier.

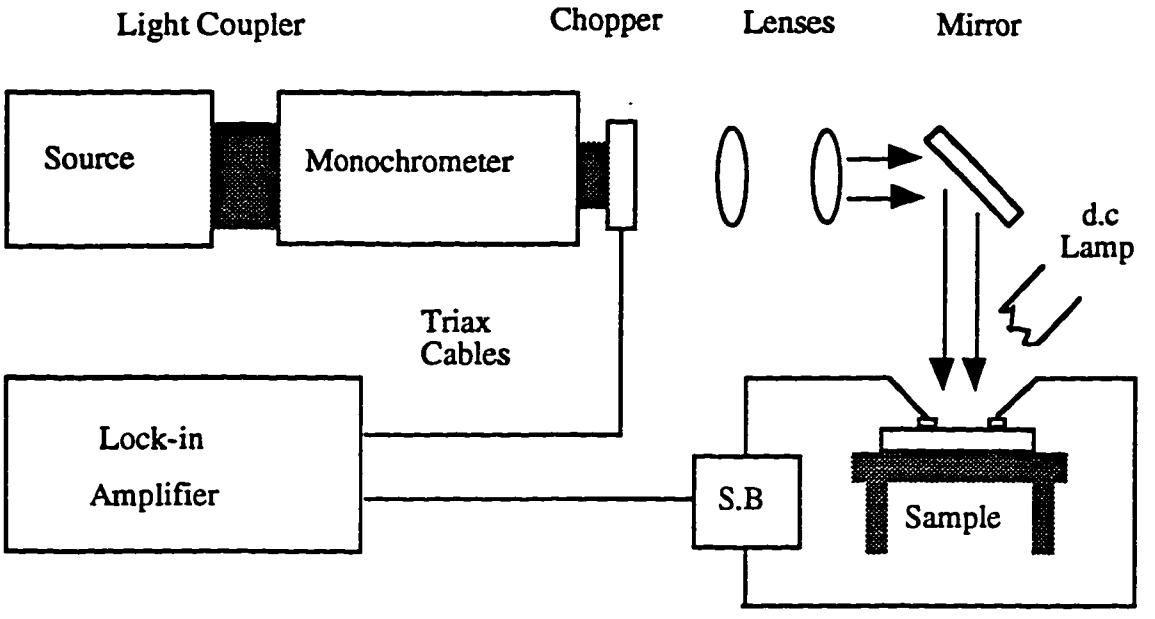

Figure 3.4. Apparatus for measuring sub-bandgap a using two-beam photocurrent technique.

Since the lifetime of the sample is constant (because of dc light with intensity of about 0.1 mW/cm^2), the photocurrent should correspond directly to the absorption coefficient α. To calibrate the apparatus, we have measured some standard glow discharge produced films provided by Dr. Wronski, along with his measured α curves. Since the absorption of each film is different, we calibrate each film by comparing the photo-conductivity absorption of the films in the region $1E3/cm < \alpha < 5E3/cm$ with the absorption from the spectrophotometer. Note that the calibration procedure needs to take account of the fact that photo-conductivity absorption depends on the assumption that the photons are absorbed uniformly in the material, but the spectro-photometric α does not. The complete procedure to derive the correction factor is shown in Appendix B.

C. Devices

1. I-V Characteristics

The performance of a solar cell under illumination can be complete described by current voltage dependence. If we consider a typical current voltage curve of a p-i-n solar cell under illumination as shown in Figure 3.5. and it equivalent circuit as shown in Figure 3.6. We can define three parameters that give a rather complete description of the electrical behavior.

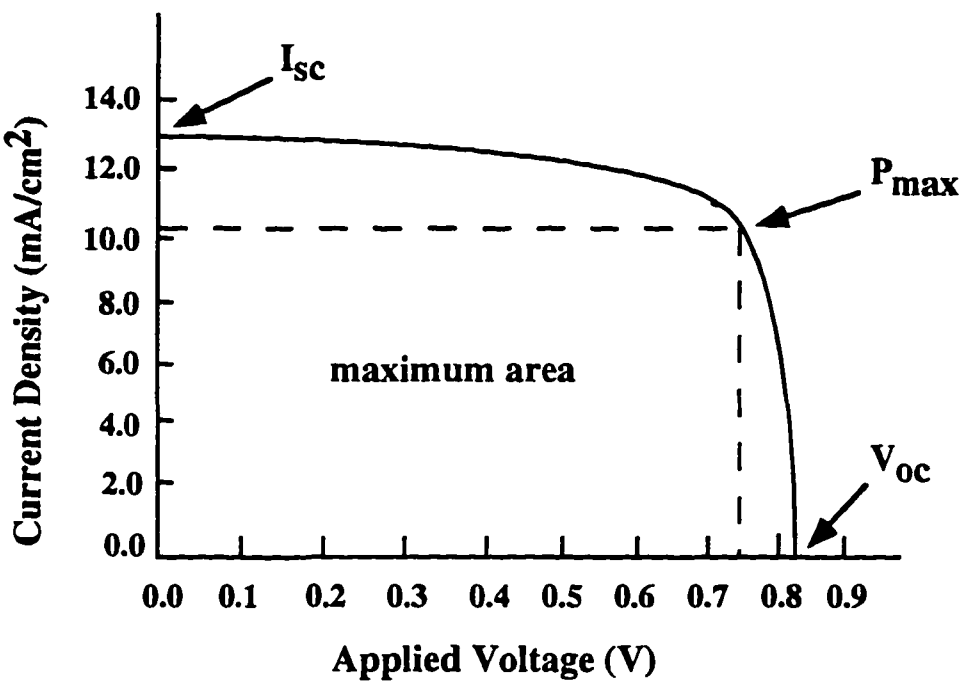

Figure 3.5. Current voltage characteristics of an illuminated p-i-n diode.

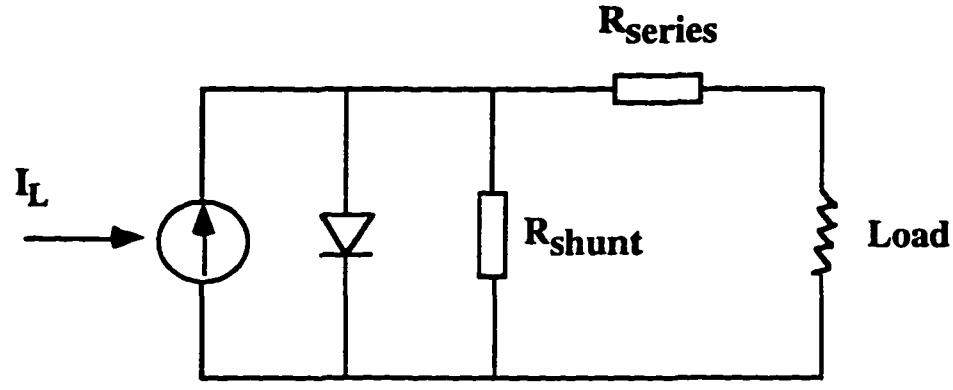

Figure 3.6. Equivalent circuit of $p^+/ i /n^+$ solar cell.

From the equivalent circuit, the current-voltage characteristics of the device is given by

$$J(V) = J_s\left[e^{\frac{qV}{AKT}} - 1\right] - J_L(V) \qquad (3.11)$$

where J(V) is the current J at voltage V, J_S is the reverse saturation current, q is the electronic charge, A is the diode factor, K is Boltzman's constant, T is the temperature and J_L is the light generated current.

The above equation which is the superposition of diode rectifier equation and the photo-induced current equation, can be rewritten as:

$$J(V) = J_0 e^{\frac{-E_g}{BKT}}\left[e^{\frac{qV}{AKT}} - 1\right] - J_L(V) \qquad (3.12)$$

where 'B' is the diode factor.

The first parameter is the short circuit current J_{SC}, which is the current of the cell under illumination for V=0. From equation (2) we see that it is equal to $J_L(V)$ i.e. the photogenerated current, if the series resistance i.e. $R_s = 0$. A finite series resistance R_s reduces the short-circuit current. The photogenerated current, also called short-circuit current, depends upon the spectrum of the incident light, the material response to the light and the collection efficiency. Thus it can be represented as

$$J_L = q\int (1-R)Q(E)S(E)dE \qquad (3.13)$$

where 'R' is the reflection co-efficient of the material, S(E) is the spectrum of the light source and Q(E) is the collection efficiency of the structure.

The second parameter is the open-circuit voltage V_{OC}, which is obtained for J(V) = 0. Thus from equation (1) we have

$$V_{oc} = \frac{AkT}{q}\ln\left[\frac{J_L}{J_S}+1\right] \qquad (3.14)$$

The above equation is valid for an ideal case where $R_s = 0$ and $R_{sh} = \infty$. From equation (3.14), we see that V_{OC} is determined by the ratio J_L/J_S and thus by the absorption and light-generation process and the efficiency with which the charge carriers reach the depletion region.

The performance of the solar cell is eventually determined by the fraction of the total power of incident light that can be converted in to the electrical power. In general, the solar cell will be operated under conditions that give the maximum power output. The maximum possible area $P_{max} = V_m I_m$ for a given current voltage curve determines the fill factor FF, which is defined by

$$FF = \frac{V_m I_m}{I_{sc} V_{oc}} \tag{3.15}$$

Evidently, FF is larger the more "square-like" the current-voltage curve is. The fill factor provides an indication of the quality of the material used in the i-layer, and how well the solar cell is designed. A high fill factor requires low loss of photogenerated carriers in the i-layer and at the interfaces, strong electric field in the i-layer, and a good ohmic contact. High quality a-Si:H cells with proper p-i interface designs have fill factor values of about 65% to 70%. This value is less than that which can be achieved in crystalline solar cells since the conductivity of the i-layer is considerably lower in a-Si:H. A good open circuit voltage is of the order of ≈ 0.85V and a good short circuit-current is of the order of ≈ 17mA/cm^2. A high open-circuit voltage requires efficient doping in the p^+ and n^+ layers (which gives higher built-in voltage) and also good interfaces. A high short circuit current requires good material quality and an optimal design of the cell to absorb and trap as many incident photons as possible.

The three parameters V_{oc}, J_{sc} and FF are sufficient to calculate the energy-conversion efficiency η of the solar cell, which is defined by the ratio of maximum power that be extracted from the cell to the total illumination power. It is represented by equation

$$\eta = \frac{I_m V_m}{\phi_{in}} \tag{3.16}$$

or

$$\eta = \frac{FF . V_{oc} . I_{sc}}{\phi_{in}} \tag{3.17}$$

where ϕ_{in} is the total power of the incident light. Considering the general expression for V_{oc} and I_{sc}, the essential material parameters that determine the efficiency of the solar cell are the lifetime and mobility of the minority charge carriers, and the surface recombination velocities. Since the technical design of a solar cell device is closely linked to the material parameters, practical solar cells will have to compromise between different aspects and will therefore have efficiencies lower than the ideal values.

Energy of the light source of one sun intensity is about $100mW/cm^2$, and the area of cells used in this project is $\approx 0.08cm^2$. The light source used for I(V) measurement is an ELH lamp biased at 110V.

2. Quantum efficiency

The quantum efficiency (QE) measurement is another useful diagnostic tool to characterize the performance of solar cell devices. Quantum efficiency is defined as the ratio of number of charge carriers collected to the number of photons incident on the sample at a particular wavelength. QE measurements provide information on how well the device absorbs photons of various wavelengths, and how well the photogenerated carriers are collected under normal forward-bias operating conditions. The internal electric field is reduced with biasing in the forward direction, and the QE results provide details as to how this reduction affects the collection of photogenerated carriers. Also, any problems in the device design that may inhibit carrier collection such as hole trapping at the p-i interface can be uncovered. Finally, the dependence of QE at a particular wavelength, on the bias voltage can be used to estimate the material transport parameters. This technique will be discussed in detail in the next section.

To measure QE, the set up used is illustrated in Figure 3.4. In this setup, the monochrometer is used to change the wavelength of the incident photons. The output of the

monochrometer is chopped. The chopped beam is focused on the sample through a beam splitter, the other half of which goes to photodetector used as the reference cell. This reference cell is used to determine the photon flux incident on the sample at each wavelength. The chopper modulates the photon signal to produce a 13.5Hz square wave. This operation reduces the noise due to the ambient light and 60Hz power lines. A high pass filter is also used at $\lambda \geq 700$nm to get rid of photons of lower wavelength. The lock-in amplifier is tuned to the chopper frequency. The photogenerated current from the devices under test for each incident photon wavelength is amplified using a current preamplifier and then measured by the lock-in amplifier. A dc light source also illuminates the sample to continuously fill the midgap states and keep the occupancy of the midgap states unchanged. This results in the splitting of quasi-Fermi levels of the carriers and thus ensuring that the carriers collected are those resulting from valence band to conduction band transitions.

The sample under test can be biased at forward or reverse voltages or be grounded. Typically, the device currents are measured over the visible wavelength range of $400\text{nm} < \lambda < 800\text{nm}$, at steps of 20nm, since this range covers the major portion of the solar spectrum. The forward and reverse bias voltages can be applied to the cell to simulate operation conditions and to enhance the internal electric field, respectively. Longer wavelengths ($800 < \lambda < 1000$nm) are used to determine the Urbach edge and Tauc gap using the techniques described in subsequent sections.

The photocurrent produced by the reference cell at each wavelength is also measured to determine the relative light intensity at various wavelengths. This intensity can change from day to day, depending upon exact positions of the lenses and conditions of the lamp. Since the reference cell is not subjected to the same number of photons as the sample under test, the $QE(\lambda)$ values are relative. A reference is chosen by arbitrarily setting the peak $QE(\lambda)$ value. Then all of the other $QE(\lambda)$ values are scaled to this reference. Care must be taken when interpreting the QE curves from one sample to the next, since they all have the same peak

reference point. This method, despite this, provides the correct relationship between the QE(λ) ratios of a particular sample, and from sample to sample.

QE measured at zero bias voltage provides important information about the cell. We can have an idea about the thickness of the p^+ layer by looking at the QE values at short wavelengths (~ 400nm). Too thick a p^+ layer would lead to a very low QE value and too thin a p^+ layer would result in unreasonably high QE. The generally accepted QE value at short wavelengths is about 0.5-0.6 for a 10nm thick p^+ layer. QE values at long wavelengths (~700nm) tells us about the collection efficiency for long wavelength photons. This is affected by the reflection due to the texture of the substrate. It is also affected by the material quality of the i-layer. A good reflector, such as the combination of ZnO/Ag, with proper texture, will yield a QE value which is above 0.2 at 700nm, given that the material quality of the i-layer is good. Finally the position of the maximum QE in the spectrum is usually associated with the thickness of the i-layer. When the thickness of the i-layer is reduced, the maximum QE position will shift towards shorter wavelengths. For a cell with about 350nm of i-layer, the maximum QE point is located at 540nm.

QE measured under bias can tell us about the electric field profile inside the cell. When the solar cell is under forward bias, the internal electric field is reduced. As a result, the carrier collection efficiency (especially of those created away from the p-i interface) is reduced since the carrier collection of a-Si:H solar cell relies on the assistance of the electric field because of low α for higher wavelengths. The electric field, in fact enhances the effective carrier diffusion length. For a high quality solar cell, the internal electric field is so strong that a small forward bias applied to the cell will not affect the carrier collection efficiency to a great extent.

The ratio of the QE(λ) values under reverse to zero bias can provide information about how well the device absorbs and collects the photons of various wavelengths at various locations i the cell. Since the photons are incident on the p-layer, the lower energy photons are absorbed farther from the p-layer than the higher energy photons. As a result, these

photogenerated holes must drift farther across the i-layer before they are collected in the p-layer. If the QE ratio at these wavelengths is high, it is an indication that the holes were being generated but were not being collected without the extra field-assist provided by the negative bias. Low QE ratio indicates that the material is of high enough quality to collect the holes even at zero bias. Also if the ratio is high at shorter wavelengths, the problem can be pinned on the p-layer or p-i interface. This will be discussed later in the device design section. Thus we see that QE ratios provide a useful method for evaluating various cell designs and also help optimize various layer thicknesses.

3. Urbach edge and mid-gap states in silicon p-i-n devices

Urbach energy of valence band tails and mid-gap defect densities are important parameters for determining the performance of amorphous silicon (a-Si:H) devices.

Amorphous silicon material, as seen in the earlier section, has two different types of defects in its energy gap, the tail states near the conduction and valence bands, and the mid-gap defect states. Both types of defects play an important role in determining the properties of p-i-n devices made from this material. In particular, the tail states limit the movement of level upon light excitation, and thereby provide a limit to open-circuit voltage that can be developed in an a-Si:H solar cell. The mid-gap states provide a very effective recombination-mechanism for excess carriers, and thus tend to limit the diffusion length of minority carriers, and hence fill-factors and open circuit voltage in solar cells. A high density of mid-gap states also reduces the electric field (E) in the middle of the device, thereby reducing the range of the minority carriers.

The traditional way to measure these parameters has been to measure them in films, not in devices. In particular, sub-gap photo-conductivity techniques, which rely on optical excitation from these states, have been widely used to estimate these parameters. However, it

is not obvious that the properties measured in films, deposited on glass substrates, are the same as in materials used in devices, which we deposited on conducting substrates such as steel or SnO_2. It is well known, for example, that the growth rates on these substrates are very different from the rates of films grown on glass, and that ion-bombardment is different, simply because glass is an insulator and the devices are deposited on conductors.

To address these problems, Crandal originated the concept of measuring sub-gap quantum efficiency (QE) of devices. This technique was later used by Wronski et.al. to measure Urbach edge and defects in a-Si:H Schottky barriers. It was recently shown by Dalal et.al. that a measurement of the sub-gap quantum efficiency (QE) of the device at zero or reverse bias provides an accurate indication of Urbach energy of the i-layer in the device.

A solar cell is a minority carrier device. In general, in most a-Si:H solar cells, the electron diffusion length is much larger than the hole diffusion length, and much longer than the dimensions of the device. Under these circumstances, except right near the p-i interface, for most of the cell, the holes can be considered to be the minority carriers, and therefore, the current is determined by the transport of holes across the cell. Therefore, when we measure QE of a device for sub-gap photon energies, it primarily measures the collection of holes generated in the bulk of the i-layer by the monochromatic beam incident on the cell. When the wavelength of incident light is very short, measuring QE amounts to measuring the collection of electrons generated near the p- i interface. For photon energies near the bandgap, the photon beam is initially exciting the electrons from the valence band tail states into the conduction band as shown by Figure 3.7, by the transition labeled A.

These holes are generated near the valence band edge and are thus thermalized i.e. in contact with the valence band. In contrast, the holes generated in the mid-gap states are not thermalized, since they are far from the valence band and the mid-gap states are not in intimate contact with the valence band.

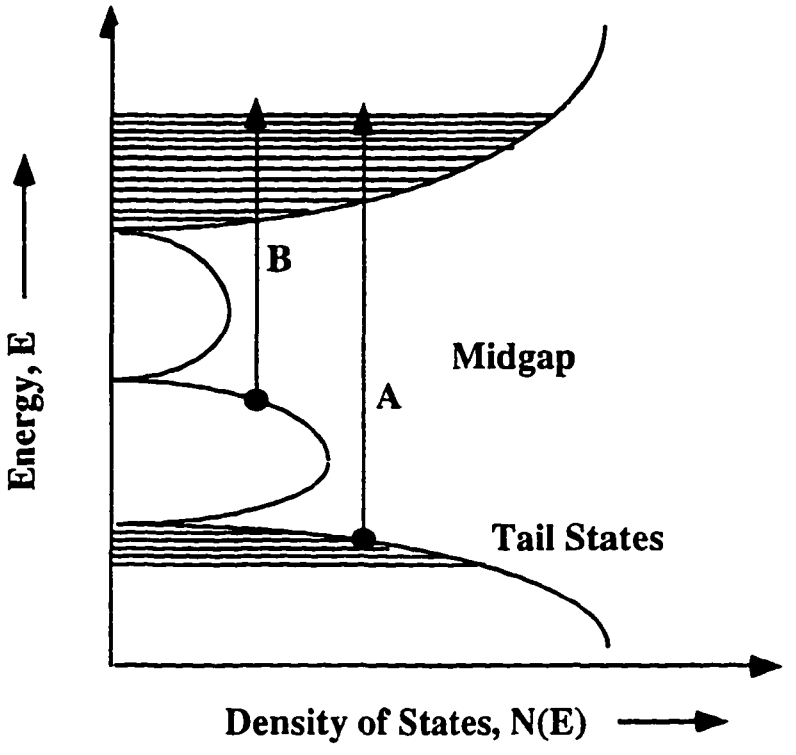

Figure 3.7. Excitation of electrons and holes by subgap photons.

Thus, we would expect that the holes generated by near-bandgap photon energies will be easily collected, whereas the deep-lying holes generated by photon energies much smaller than the bandgap may get trapped and not collected. To distinguish between these two types of holes, one can use external voltage on the device. This is based on the assumption that the shallow holes will not need significant field assistance to be collected, but the deep holes will, since they need to tunnel into the valence band from the traps, a phenomenon similar to field ionization of deep lying donors (Fenkel-Poole tunneling). Therefore, a plot of QE vs. photon energy in the tail region directly gives us a plot of absorption co-efficient vs. photon energy. The inverse slope of the natural logarithm of QE vs. photon energy gives us the Urbach energy. However , as explained earlier, when the photon energies become smaller, the

absorption is from mid-gap states to the conduction band transitions (shown by transition B in Figure 3.7), and then the holes are no longer in thermal communication with valence band and need significant field assist.

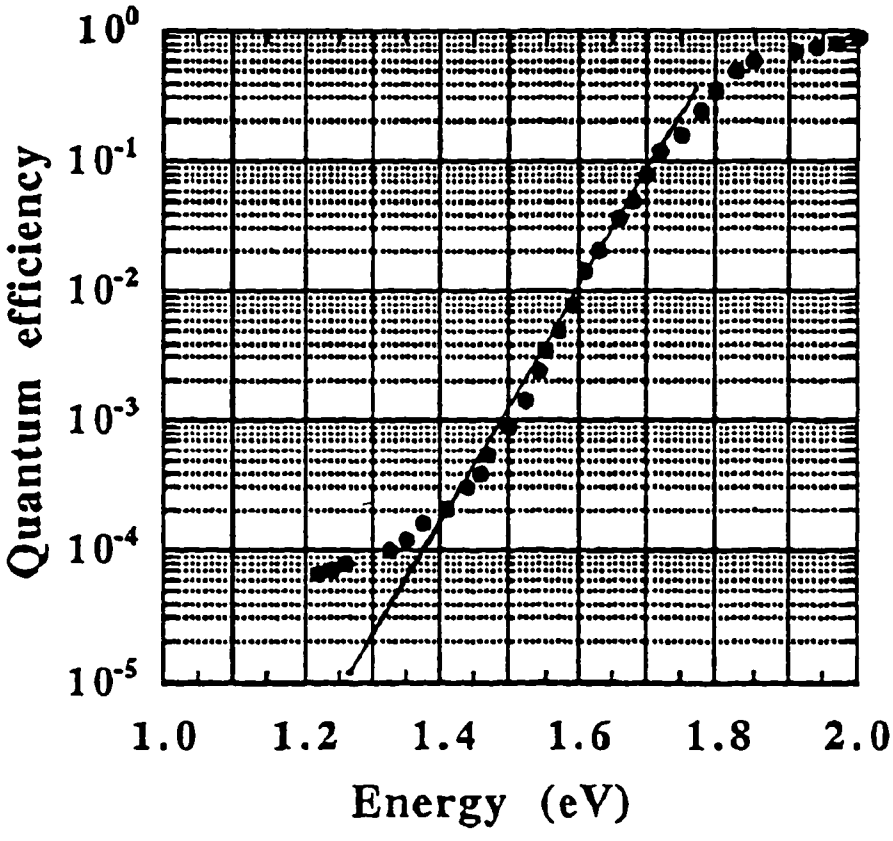

Figure 3.8. Log of QE vs. photon energy curve for a good a-Si:H device with high fill factor. The Urbach energy of the a-Si:H i-layer was 44meV.

Thus, mid-gap states cannot be calculated accurately from a measurement of sub-gap absorption, but the Urbach edge can be. For this measurement to be accurate, it is necessary that we make a series of devices all identical except for changes in the bandgap of the i -layer.

The long range photons used to calculate the Urbach edge is approximately between 800 nm and 1000nm. For illustration, in Figure 3.8, we show log(QE) vs. photon energy plot for a very good a-Si:H device, with a 66% fill-factor. As we see, the Urbach energy is in the 45meV range, whereas for a bad a-Si:H device it is 50 to 52 meV.

4. Tauc Gap

The log plot of long wavelength QE(λ) used for Urbach energy measurement can also be used to estimate the Tauc gap.

If the Tauc gap of an intrinsic material is known, and the material is incorporated into the i-layer of a constant bandgap device, then its long wavelength QE(λ) plot can be used as a reference for samples where the Tauc gap is not known. In fact, this can be an important tool for measuring the change in Tauc bandgap when Helium dilution is used instead of Hydrogen, to fabricate the intrinsic layer in the cell.

Since the absorption by the band tails begins when the photon energy drops below the Tauc gap, the plot of QE(λ) will drop off at the Tauc gap energy. Then, determining the Tauc gap of an unknown sample is accomplished by measuring the shift in the energy of QE(λ) plot compared to that of the known sample. The procedure is illustrated in Figure 3.9. All of the constant bandgap devices used for this measurement were fabricated with similar deposition parameters except for the gas flow rates and substrate temperatures used to change the material.

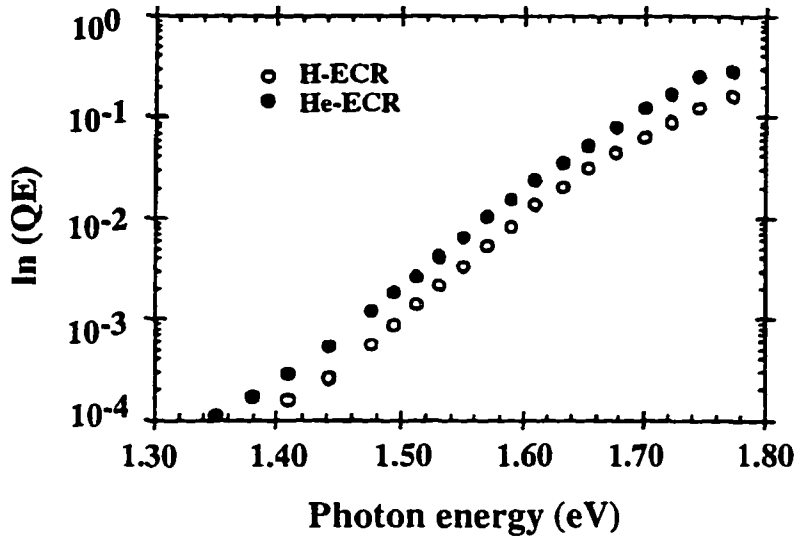

Figure 3.9. Example of the subgap quantum efficiency for a constant band gap device; the inverse of the slope is the Urbach energy and the energy shift provides an estimate of the Tauc gap for the unknown sample.

5. Hole $\mu\tau$ product

The $\mu\tau$ product of holes is a very important parameter for devices. It is the quantity which primarily determines the fill factor of the cell. This assertion arises from the fact that over most of the cell, the holes are minority carriers (the carrier with lower $\mu\tau$ product). Only near the p-i interface do the electrons become the minority carriers. Therefore, in order to have a high collection efficiency for most wavelengths of light absorbed in the cell, the hole range, $\mu\tau E$, where E is the electric field, must be large compared to the thickness of the i-layer. A ratio of 10:1 or 20:1 is desirable. In a-Si:H solar cells, this condition is easily met, since the hole $\mu\tau$ product is about $4 - 6 \times 10^{-8} cm^2/V$ and the electric field is about $1 - 2 \times 10^4 V/cm$. Thus, the range is about 5-10μm, much larger than the thickness of the i-layer (about 0.4 μm). The higher midgap defect density can severely reduce both, the electric field in the middle of

the i-layer, and the hole $\mu\tau$ product. This can result in lower collection efficiency, particularly near the maximum power point of operation of the diode, when the diode is under forward bias, and the internal field is reduced significantly. These considerations are illustrated in Figure 3.10, where we schematically show the electric field profiles in the device under zero and forward bias.

Surprisingly, this very important quantity is not normally measured in devices. There have been some measurements of hole trapping lifetimes and hence hole trapping $\mu\tau$, but it is not clear that this quantity is the same as device hole $\mu\tau$ product, since one is a transient phenomenon and the other is a steadystate phenomenon.

The basic principle of the measurement technique is quite simple [48]. We measure the quantum efficiency of the device for many wavelengths, as a function of applied voltage. Under reverse bias, the QE increases, and under forward bias, it decreases. Since this increase or decrease is due to the increase or decrease in the field in the device, one should be able to model the field profile and obtain the hole $\mu\tau$ product from the curves. For a given device one should be able to fit all the QE curves (QE vs. wavelength) using the same value of $\mu\tau$ product, except for the shortest wavelengths where p-i interface recombination becomes important and the model is invalid. But certainly, for long wavelengths, such as 600 - 800 nm, the model should be valid and yield a value for $\mu\tau$. At this time, we need to know how to model the field. The model that we use utilizes a greatly simplified algorithm for finding the internal electric field in the device structures for various biasing levels and bandgap designs. It is proven to be more versatile than more complex programs such as the AMPS programs produced by Penn State. In particular, the AMPS program does not allow the user to study different forms of output such as the electric field profile at different levels of bias voltage. The simplified program that we made and used for our work allowed us to determine the hole

transport parameters and successfully predict which device designs would have greater have greater efficiency.

The simulation of photogenerated carriers collection begins by finding the fixed charge density as a function of distance into the i-layer by integrating the defect density over the energy shift created by band bending. The energy dependent density -of-states can be given by the equation (see Figure 1.3).

$$g(E) = g_0 \exp(E/E_a) \tag{3.18}$$

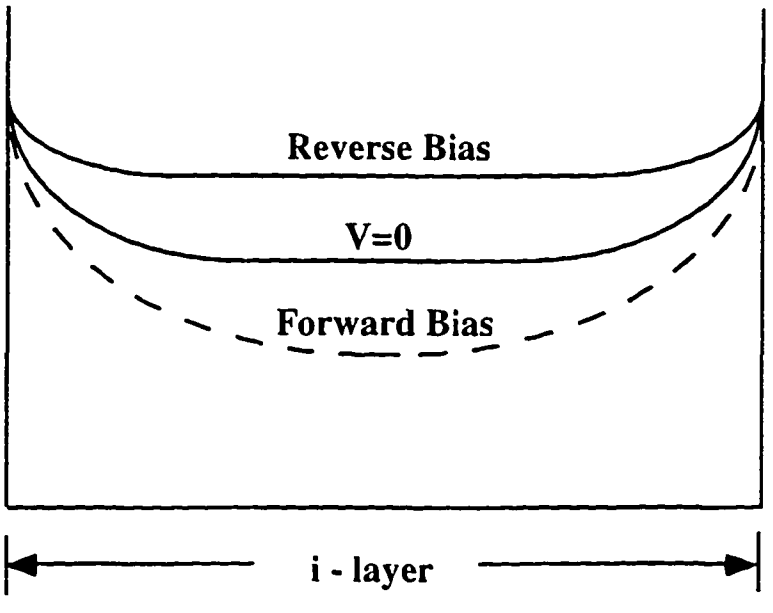

Figure 3.10. Electric field profiles in the i-layer of the device under forward, zero and reverse bias.

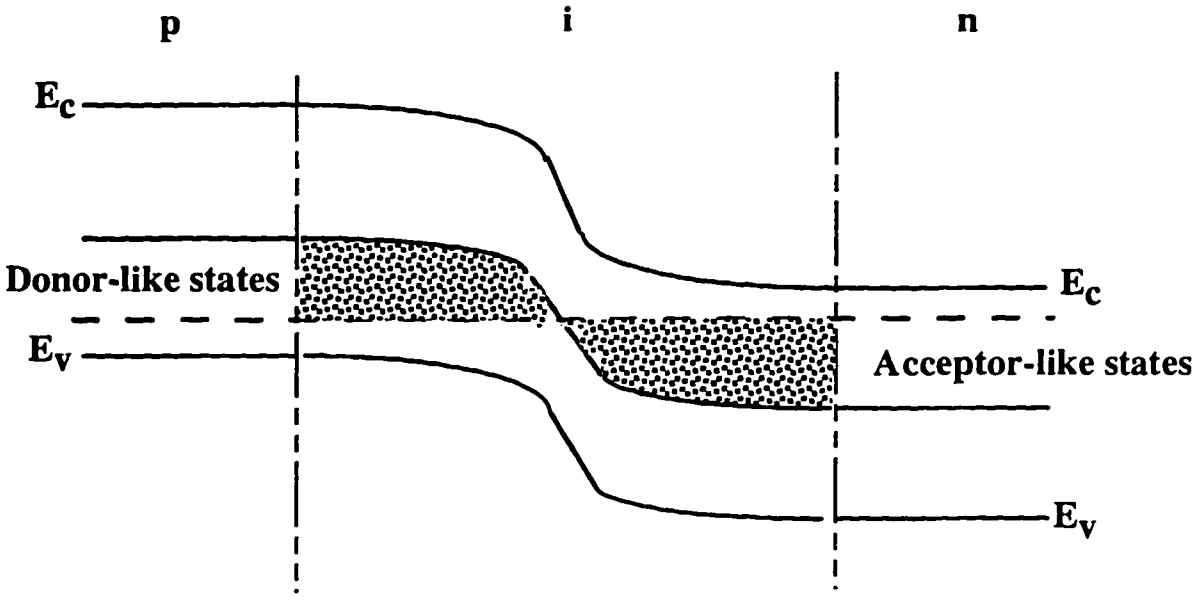

Figure 3.11. Band diagram showing occupied midgap defect states.

Here g_0 is the initial defect density. The position of g_0 marks the transition from acceptor-like states found in the upper half of the bandgap, to donor-like states in the lower half of the bandgap, and is located near the center of the bandgap. Then, for a junction with p-type or n-type material, band bending occurs in the i-layer as shown in Figure 3.11 and the donor like states give up an electron each as they move about above the level and become positively charged. These states are shown by the cross-hatched area in the left half of the i-layer in Figure 3.11.

The acceptor-like states (right half of i-layer in Figure 3.11) capture electrons and become negatively charged. Since the value of g_0 can be found directly from the value of bandgap using the equation

$$g_0 (E_g) = C_1 \exp (-C_2 E_g) \qquad (3.19)$$

where E_g is the bandgap, and C_1 and C_2 are experimentally derived values. Typical values of these parameters are 9.76 x 10^{22} cm^{-3} eV^{-1} for C_1 and 10.5 eV^{-1} for C_2. Thus the fixed charge density as a function of distance into the i-layer is given by

$$\rho(x) = qg_0 \int_{E_f}^{E} \exp(\frac{E}{E_a})dE' + qN_t \qquad (3.20)$$

Here N_t is the midgap charge density and can be determined using the model as described later.

The analysis of $\rho(x)$ assumes a zero-temperature occupation probability for the defect states. In other words, when a state moves across the level, it is immediately occupied. This approximation results in an occupation probability error on the order of kT/qE_a, which is small since E_a is normally greater than kT/q by a factor of 4 or more. As described earlier the band bending in the i-layer depends on the DOS distribution also the biasing of the device will alter the band bending which is an important effect included in this model that is neglected in other models such as AMPS.

From the fixed charge distribution found in equation 3.20 and using Poisson's equation, the electric field E(x) at any position x can be found from the equation

$$E(x) = \sqrt{\left[\frac{2g_0E_a}{\varepsilon}\left(\exp\left(\frac{qV(x)}{E_a}\right)-1\right)+\frac{2q}{\varepsilon}\left(N_tV(x)-g_0E_aV(x)\right)+E_0^2\right]} \qquad (3.21)$$

where E_0 is found by the model .

Substituting dV/dx for E, and integrating produces the equation for the energy qV at any position x,

$$x = \int_0^{V_f} \frac{dV}{\sqrt{\left[\frac{2g_0E_a^2}{\varepsilon}\left(\exp\left(\frac{qV}{E_a}\right)-1\right)+\frac{2q}{\varepsilon}(N_tV+g_0E_aV)+E_0^2\right]}} \tag{3.22}$$

The above equation is solved numerically for V and substituted back in equation 3.21.

The only adjustable parameter we used for modeling the field was the mid-gap defect density g_0, expressed in $/cm^3\text{-}eV^3$. Once the field is known, the hole kinetics can be simulated using the concepts of Smith [39]. An effective diffusion length, known as the down stream diffusion length L_d can be found from

$$\frac{1}{L_d} = \frac{1}{2L_p}\left[\left(\frac{E}{E_c}\right)^2+4\right]^{1/2} - \frac{E}{2L_pE_c} \tag{3.23}$$

where L_p is zero-field diffusion length, and E_c is a critical field defined by the relation

$$E_c = \frac{kT}{qL_p} \tag{3.24}$$

L_p is related to the carrier mobility-lifetime product $\mu\tau$ by

$$L_p = \sqrt{\mu\tau\frac{kT}{q}} \tag{3.25}$$

Once the effective diffusion length is known for every position, hole transport can be found from

$$\Delta p(x) = \Delta p_0 \exp\left[\frac{-x}{L_d}\right] \tag{3.26}$$

where D_{p0} is the photogenerated hole density at any position within the i-layer and $D_p(x)$ is the hole density at distance x from that position. This formulation for hole transport is a very effective method for accommodating the non-uniform electric fields found in the p-i-n diode. Under forward bias conditions, some i-layer configurations result in regions of zero electric field near the center of the diode; holes are transported solely by diffusion and L_d reduces to L_p.

The value of Lp depends on the density of defect states in the material. From the definition of diffusion length and the fact that the mobility is proportional to 1/g(E) in amorphous material, the following relationship is derived as

$$L_p = L_{p0} g_0^{-1/2} \tag{3.27}$$

where g_0 can be found for a given E_g as described earlier and L_{p0} is of the order of $2000 cm^{1/2} eV^{-1/2}$.

The final step before computing the quantum efficiency is to determine the number of holes generated in the i-layer. The total number of electron-hole pairs generated is assumed to be equal to the number of photons absorbed. An expression for the number of ehp's at any point in the i-layer can be derived from the definition of the absorption coefficient and is given by

$$G = G_0 \alpha(\lambda) \exp[-\alpha(\lambda) x] \tag{3.28}$$

where $G_0(\lambda)$ is the incident photon flux at wavelength λ and $\alpha(\lambda)$ is found by equations 1.1 and 1.2

Now the quantum efficiency can be computed at a given wavelength λ and voltage V as

$$QE(\lambda, V) = \int_0^L G(x)\exp\left[\int_0^x \frac{-dx'}{L_d(x', V)}\right]dx \tag{3.29}$$

where L is the length of the i-layer. The absorption coefficient α is continuous over the entire length L since the bandgap is continuous over L. How well the numerical evaluation for equation 3.29 reproduces experimental results depends primarily on the accuracy of the electric field simulation and on the estimate of the hole transport parameter $\mu\tau$.

Since the quantum efficiency depends on both the cell bias voltage and the incident photon wavelength, experimentally varying both over a range of values provide a wide variety of cell conditions. Now once the field is known, using different values of $\mu\tau$, we can model QE vs. voltage curves, and fit them to the experimental profiles .

6. Infrared Measurements

Infrared (IR) absorption measurements of the vibrational modes yield important information on a-Si:H. The peak positions indicate the bonding configurations of the hydrogen atoms as well as oxygen or nitrogen impurity contamination. The integration over certain peaks yields information on the hydrogen concentration. A single beam Fourier Transform Infrared (FTIR) spectrometer, IBM model IR98, was used in our measurements. All samples used in the IR measurements were deposited on lightly doped single crystal silicon. Other unused pieces from the same wafer substrate were used as the reference.

A variety of vibrational modes are observed in the IR spectra of a-Si:H. The major vibrational modes for hydrogen in a-Si:H were identified by Brodsky et al [33]. The corresponding bonding configurations are depicted in Figure 3.12. The three modes are (1) the Si-H stretching mode (2000-2100 cm^{-1}), (2) the $Si-H_2$ and $Si-H_3$ bond bending scissors mode (840-890 cm^{-1}), and (3) the Si-H wagging mode (640 cm^{-1}). If the hydrogen content is low, the absorption intensity will usually be weaker than the interference fringes, which complicates the qualitative analysis.

The Si bonded H content is determined from the integrated intensity of the 640 (580) cm^{-1} wagging mode, using calibration coefficient provided by Shanks et al. [34] and Catherine et al. [35]. The coefficient was shown to be insensitive to the bonding configuration and microstructure in a-Si:H. The hydrogen content determined from this absorption peak is consequently believed to be reliable. The equation used to calculate the hydrogen content is given by Cardona [36-37]:

$$N_H = A\int \frac{\alpha(\omega)}{\omega} d\omega \qquad (3.30)$$

where A is an experimentally determined constant, and $\alpha(\omega)$ is the absorption coefficient at angular frequency ω. The integral extends over the absorption band of interest. The values of A for the vibrational modes in Si are listed in Table 3.1.

The following expression gives the hydrogen concentration C_H in a-Si:H:

$$C_H(at.\%) = 1.125\frac{S_{640}}{d} \qquad (3.31)$$

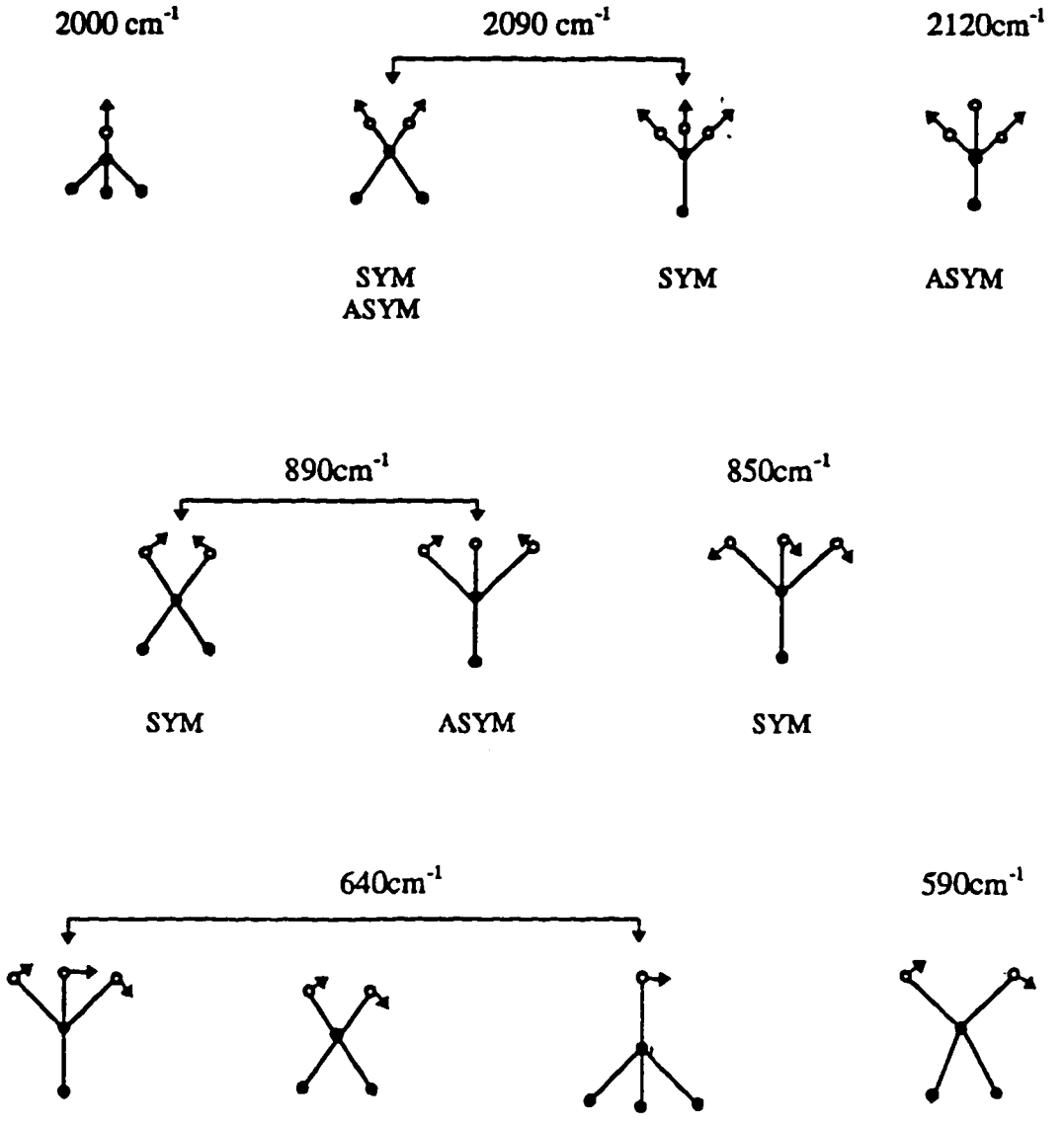

Figure 3.2. Schematic illustration of the bond stretching (top row), bond bending (middle row), and bond wagging and rocking (bottom row) modes of SiH, SiH_2, and SiH_3. SYM and ASYM indicates symmetric and asymmetric modes. The solid and open circles represent Si and H atoms respectively [33].

Where S_{640} is the area (in cm^{-1}) under the 640 cm^{-1} absorption peak and d is the thickness in microns.

The atomic percentage of Si in $Si-H_2$ and $Si-H_3$ is given by

$$N_d(at.\%) = 10.44\frac{S_{840}}{d} \qquad (3.32)$$

Table 3.1. The various vibrational modes of hydrogen in a-Si:H, their bonding configurations and the corresponding proportionality constant A [34-37].

Wavenumber (cm^{-1})	640	840-890	2000	2100	2100
Mode	Wag	Scissors	Stretch	Stretch	Stretch
Bonding	Si-H $Si-H_2$ $Si-H_3$	Si-H	Si-H (Isolated)	Si-H (Clustered)	$Si-H_2$ $Si-H_3$
A (cm^{-1}) (10^{19})	1.6	20	2.2	17	9.1

IV. RESULTS

A. Plasma

The measurements using the Langmuir probe are used to investigate the dependence of different plasma parameters on the chamber pressure and incident microwave power. The range of pressures (2 to 30 mT) al powers (50 to 100 W) were selected so as to accommodate the actual conditions used during film deposition. Most of the measurements were done using helium plasmas. Some measurement were done on hydrogen plasmas for comparison. The three stub tuner settings and the magnet field profile were the same for all measurements.

If the probe gets coated due to sputtered silicon from the walls of the reactor during the plasma measurement, large errors can be made in calculation of the plasma parameters. So the care must be taken. In our case we cleaned the reactor thoroughly, before conducting the plasma measurements.

There is a factor of two difference in the actual plasma conditions from the calculated plasma parameters. This is because of the assumptions and simplifications that one made in using the Langmuir probe. Since our goal is to understand the dependence of the plasma on our system variables, the determination of exact values for plasma parameters is not needed. Thus these assumptions does not really pose a problem for our application.

The variation of the ion current density with pressure is shown in Figure 4.1. The ion current density decreases as the pressure is increased for pressure below 15mT. However the current density increases once again about 20mT before being reduced due to the reduced mean free path at high pressure. This is in direct contrast with H_2 plasma results [41].

In case of hydrogen plasma, the current density is seen to decrease linearly with pressure [41].

The electron density as a function of pressure is shown in Figure 4.2 for two different incident power levels. Each of the curves shows a maximum in the density occurring at about 25mT. The saturation pressure has been found to shift slightly to higher pressures as the microwave power is increased. In case of H_2 plasma [41] this maximum occurs between 5mT and 10mT.

The dependence of plasma potential on the pressure is shown in Figure 4.3. We also see the variation of plasma potential with power in Figure 4.5. One can estimate the ion energy from the magnitude of plasma potential. We see that it is hard to accurately point the actual magnitude of the plasma potential but never the less we see a distinct pattern. The plasma potential tends to decrease rapidly as the pressure is increased and it shows a linear increase with increased power of the microwave. The magnitudes in no uncertain terms were greater than that for H_2 plasma [41]. This is suggestive of the fact that there may be an increase in ion energies for helium plasma.

Figure 4.4 shows dependence of electron temperature on the pressure. We see that it decreases with increase pressure. This is because of the mean free path of the electron temperature with microwave power. The values measured once again for helium plasma were some what greater than that for hydrogen plasma [41]. The dependence of T_e on microwave power is shown in Figure 4.6. It is observed from the plot that the electron temperature seems to peak around 150 W.

For the comparison the variation of plasma potential and electron temperature with pressure, for hydrogen and helium plasmas is as shown in Figures 4.7 and 4.8 respectively. These plots clearly indicate that despite of the similarities in trend, the two plasma's have significantly different properties.

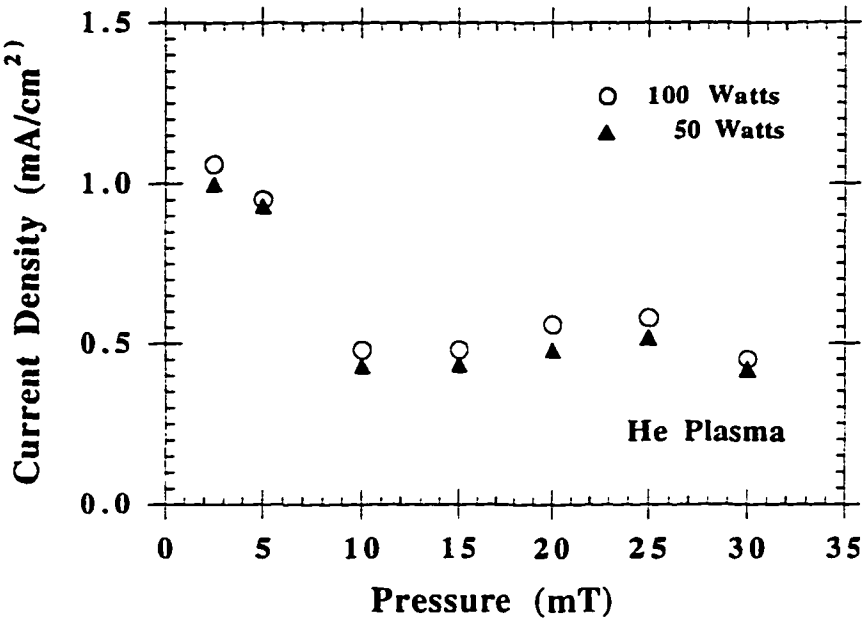

Figure 4.1. Variation of the current density with pressure in a helium plasma.

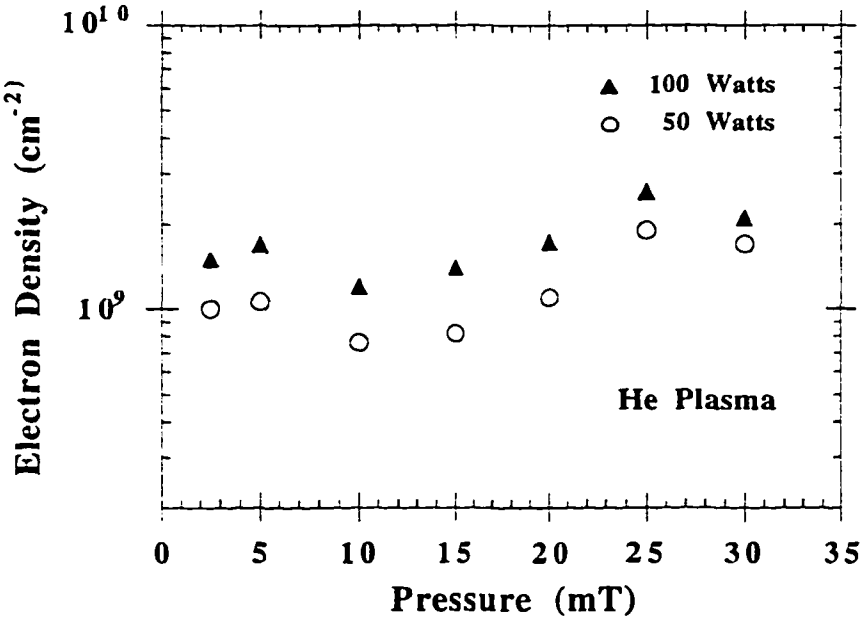

Figure 4.2. Variation of the electron density with pressure in a helium plasma.

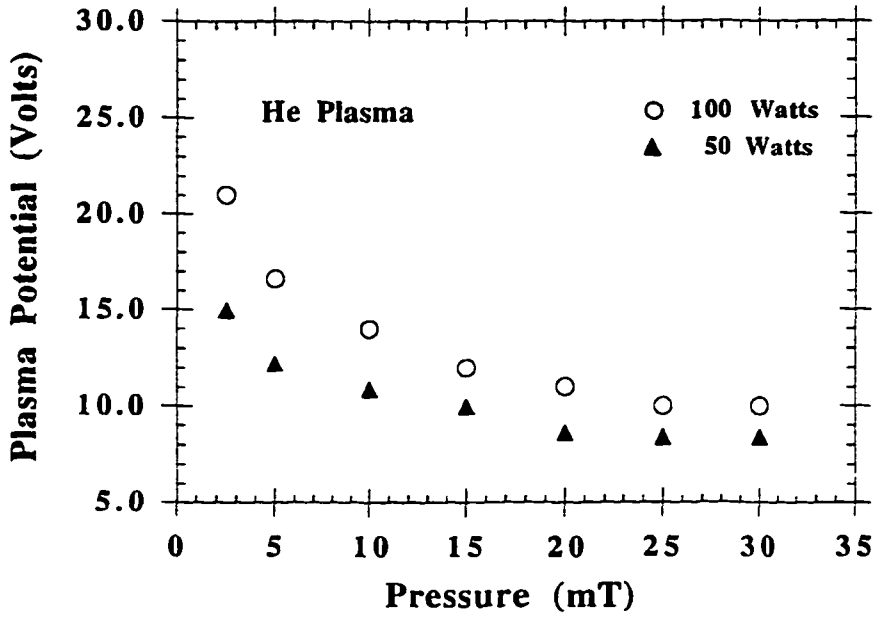

Figure 4.3. Variation of the plasma potential with pressure in a helium plasma.

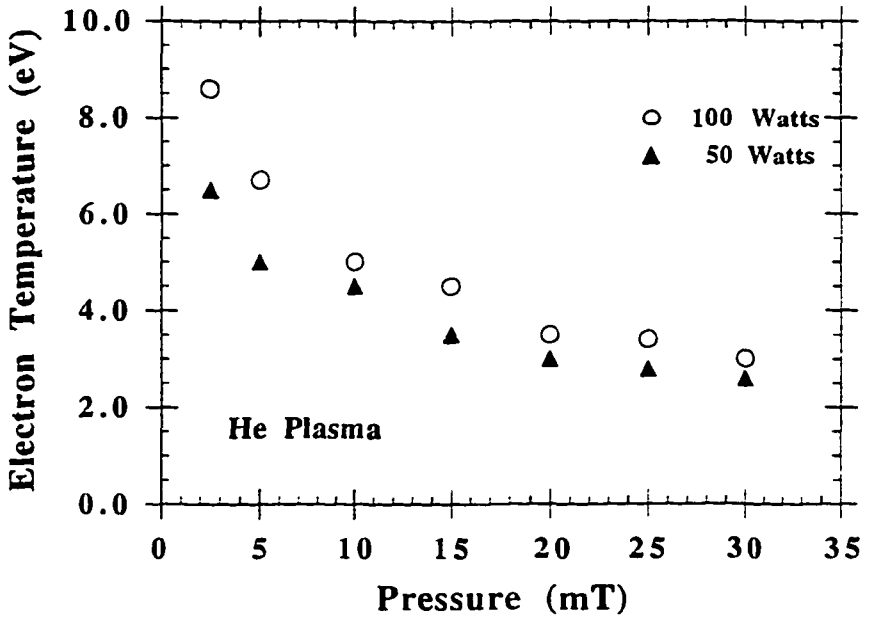

Figure 4.4. Variation of the electron temperature with pressure in a helium plasma.

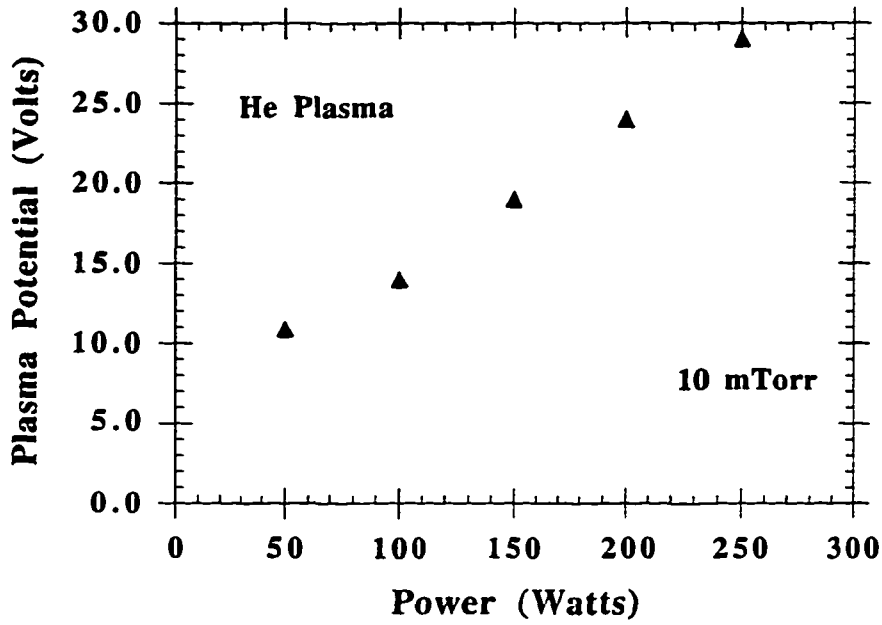

Figure 4.5. Variation of the plasma potential with microwave power in a helium plasma.

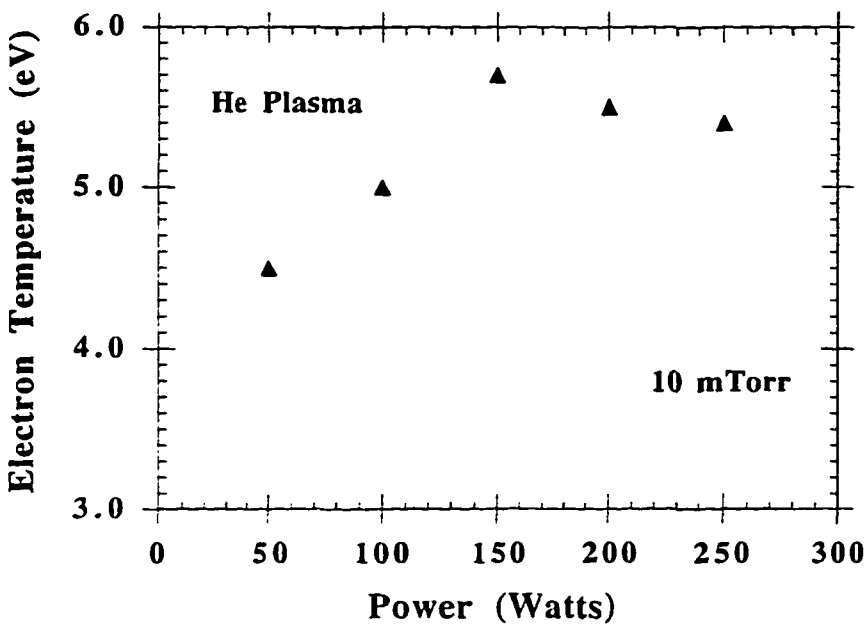

Figure 4.6. Variation of the electron temperature with microwave power.

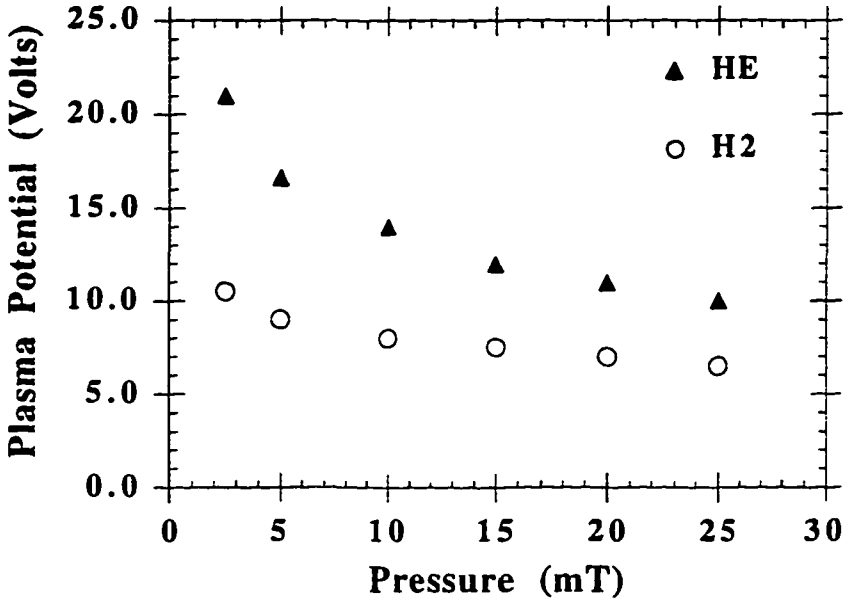

Figure 4.7. Variation of plasma potential of helium and hydrogen plasma with pressure.

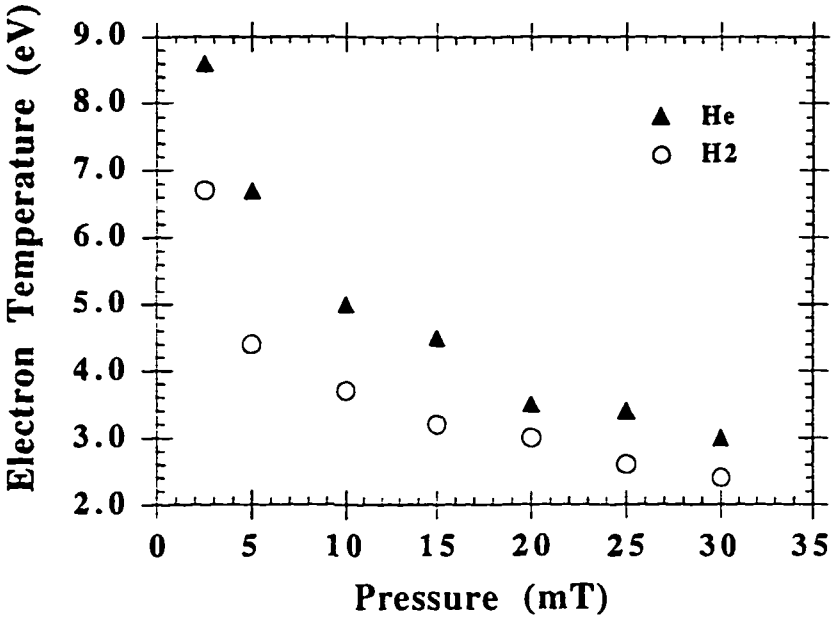

Figure 4.8. Variation of electron temperature of helium and hydrogen plasma with pressure.

B. Material

1. Hydrogen Content

To determine the hydrogen content, the films were deposited on both side polished Si wafers with resistivity ranging from 6-10 Ωcm. The single beam Fourier Transform Infrared (FTIR) spectrometer, IBM model IR98, was used in our measurements. Blank pieces from same wafer substrate were used as reference. The conditions used for the films were the one's used for growing the i-layer in p-i-n devices. These films were grown both with hydrogen and helium dilution and at temperatures ranging from 300°C to 425°C. Table 4.1 indicates the parameters used to grow the material for FTIR measurements.

Table 4.1. Deposition parameters of a-Si:H films for FTIR analysis.

					Gas Flow Rates			
					100%	100%	100%	
Sample #	Pressure (mT)	Temp (°C)	Power (Watts)	Time (min)	SiH4 (%)	He (%)	H2 (%)	C_H (%)
2/1958	25	425	45	120	10	100	-	4.6
2/1959	25	425	45	120	20	100	-	5.4
2/1960	25	375	45	120	10	100	-	5.8
2/1961	25	375	45	120	20	100	-	6.8
2/1962	25	300	45	120	10	100	-	7.2
2/1963	25	300	45	120	20	100	-	7.8
2/1964	10	425	140	140	20	20	20	8.2
2/1965	10	375	140	140	10	20	20	8.6

Since the hydrogen content in the films were low, especially in the films deposited using He dilution, the absorption intensities were not very strong as compared to the interference fringes. This made the calculation for the area slightly less accurate, thereby giving some error in the calculations of the hydrogen concentrations, which was done using equation 3.7. We observe that hydrogen content in the films grown with helium dilution is appreciably lower (4-5%), compared to the films deposited with hydrogen dilution (7-9%), both grown under similar conditions of growth rate (1-2°A/sec) and temperature. The FTIR plots of films 2/1958 and 2/1959 are as shown in Figure 4.9 and 4.10 respectively.

This suggests that with He dilution it is possible to achieve a lower band gap of the material. We have reported previously that this observation holds even for a-(Si,Ge):H films using ECR conditions[49].

The above observation also indicates that ion bombardment by He ions produced by the intense ECR discharge can lead to improvement in the film properties such as low disorder and sub-gap α. These observations are consistent with the results published earlier [50]. This fact was independently confirmed in the ECR deposited p-i-n cells with hydrogen and helium dilution. The thickness of the i-layer in both the cells were very similar (within 10%). As indicated in Figure 4.11, there is a shift in the quantum efficiency to lower energies when He is used, indicating a lower bandgap. The magnitude of this shift is about 35meV. The Urbach energy of the valence band tails which can be determined from such curves is in the range of 43-44meV, which indicates a good quality material for i-layer.

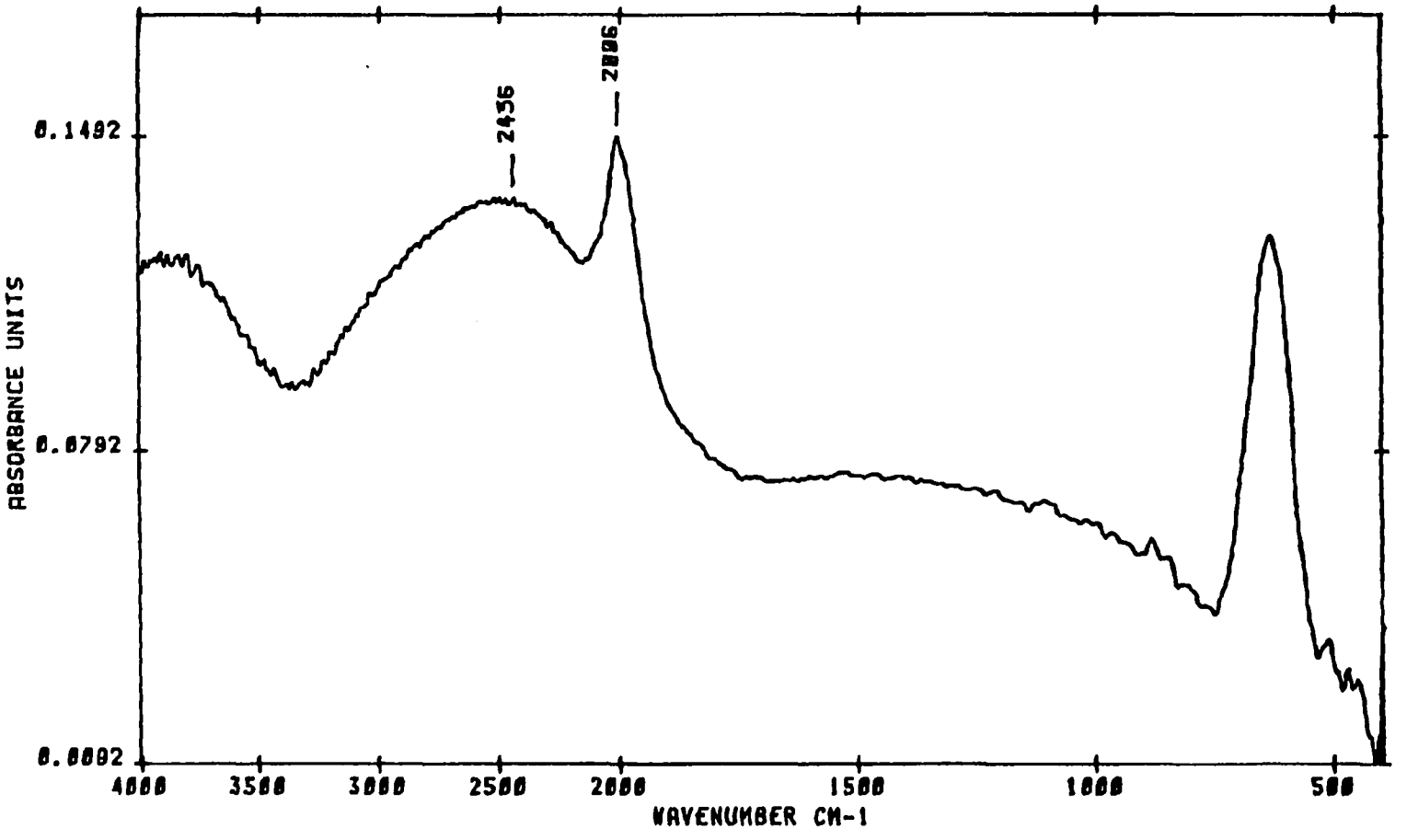

Figure 4.9. The IR absorption spectra of sample 2/1958.

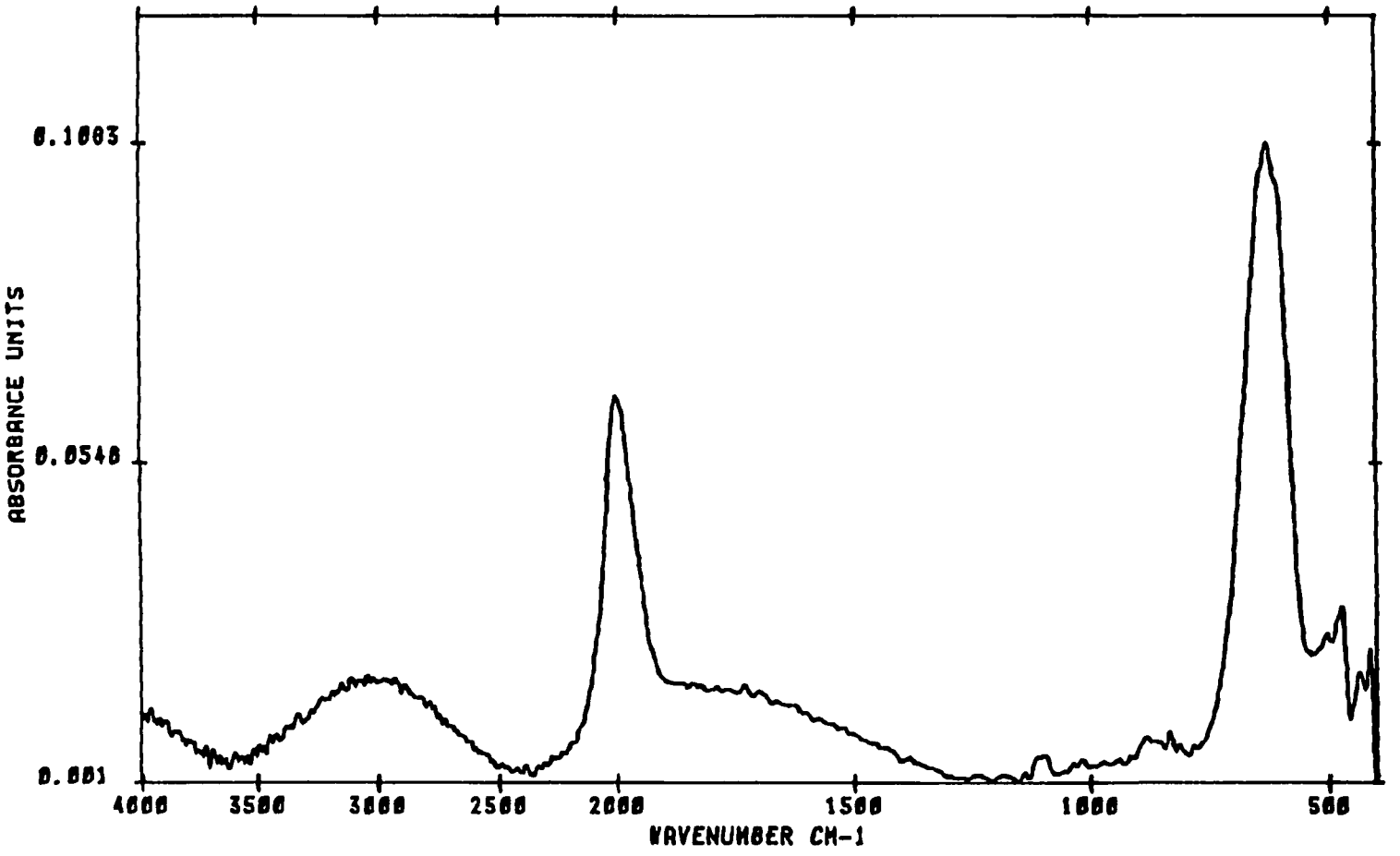

Figure 4.10. The IR absorption spectra of sample 2/1959.

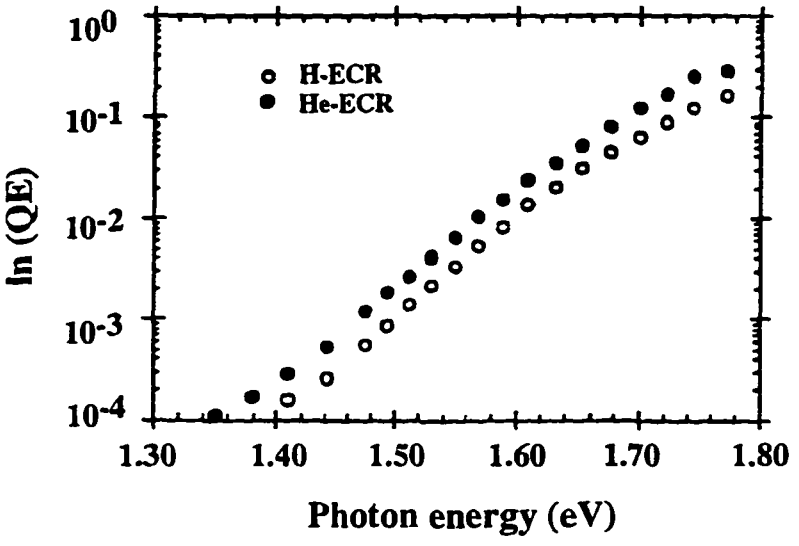

Figure 4.11. Comparison of subgap QE FOR He-ECR and H2-ECR cells of identical thicknesses. The shift to lower energies of He-ECR cell by about 35-40 meV indicates a lower bandgap. Urbach energy was found to be 43-45 meV.

2. *Microstructure*

The transmission electron microscopy was used to evaluate the film quality grown using ECR PECVD technique. TEM analysis require thin (t<200nm) samples with no substrate to allow the electron beam to pass through the sample. This limitation on film thickness requires a special method for film preparation.

Initially, the films were deposited on the silicon wafers. The samples were then cut in small square pieces (1 cm^2) and then stacked together with the help of a synthetic glue. The samples were then sliced with a diamond saw to produce approximately 3mm wide strips of deposited material. They were subsequently milled to reduce the thickness. During the sawing process, the films would always flake off the substrate and the samples would be destroyed. The method that we used finally to do the job was to grow the film of a-Si:H material of 50nm

thickness directly on a 3mm copper grids coated with approximately 10nm of carbon. A new substrate holder was made to hold the copper grids in the deposition chamber, on which the thin a-Si:H layer was deposited with the same parameter as the one used for the i-layer in the devices. It is expected that the growth on these carbon coated substrates will not exactly simulate the film growth on the large glass or tin-oxide substrates due to small sample size and proximity of the mask. However, this method is very useful for comparing the microstructure of a series of alloy compositions all deposited on these same substrates.

The parameter for deposition for the film for this study are listed in Table 4.2. The films series included a range of substrate temperature, and different plasma gases viz. hydrogen and helium. It is expected that higher temperatures should increase surface mobility of the incident ions and radicals and promote the growth of a more homogeneous network. Helium plasma induced ion bombardment should have similar effect since the incident ions provide excess energy to the growing surface.

Table 4.2. Deposition parameters of a-Si:H films for TEM analysis.

				Gas	Flow	Rates
				100%	100%	100%
Power	Pressure	Temp.	Time	SiH4	He	H2
(Watts)	(mT)	(°C)	(min)	(%)	(%)	(%)
45	25	425	8	20	100	-
45	25	375	8	20	100	-
45	25	425	8	10	100	-
45	25	375	8	10	100	-
140	10	425	10	20	-	20
140	10	375	10	20	-	20

But to our surprise, when we observed the selected area diffraction patterns(SAD) of the films grown with He-ECR, the non-homogeneity of the microstructure was very evident. We could observe diffused ring SAD pattern at one position and could also observe a double diffraction SAD pattern at some other location on the same film indicating the embedded crystallites in the amorphous structure. One such SAD pattern of the film grown at 425°C using He-ECR is as shown in Figure 4.12. With added curiosity we then observed the SAD pattern for the film grown using H-ECR at 425°C. This SAD pattern is shown in Figure 4.13. To investigate thoroughly we recorded SAD patterns at various locations on this film. We could not see any double diffraction patterns or diffused ring pattern but consistently we observed the similar pattern as in Figure 4.13 on all the selected locations of the film indicating a uniform micro/poly crystalline film. Thus we conclude that with hydrogen dilution we get better homogeneity in the microstructure of the film.

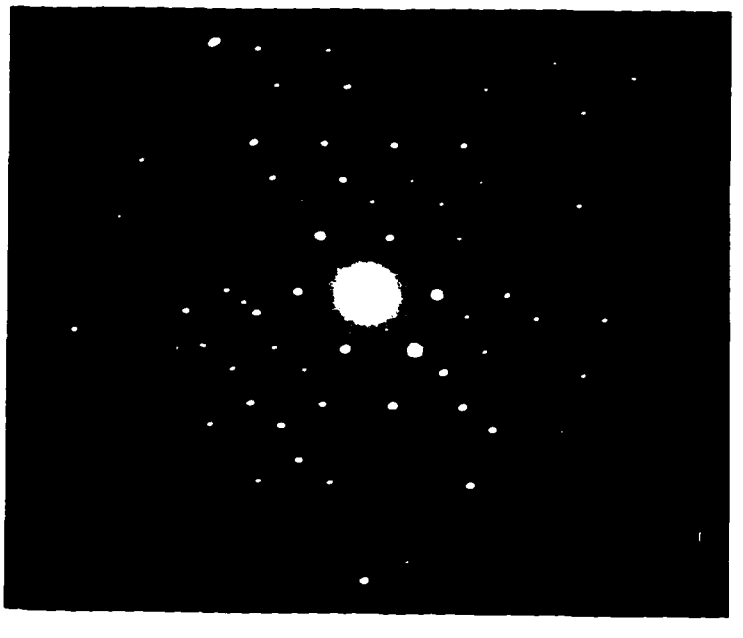

Figure 4.12. SAD pattern of the a-Si:H film grown using He dilution.

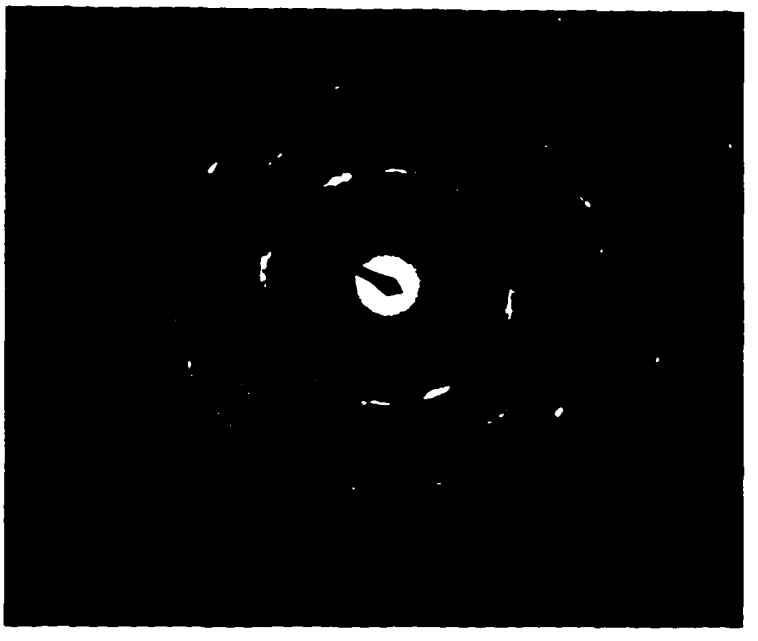

Figure 4.13. SAD pattern of the a-Si:H film grown using H_2 dilution.

C. Devices

1. Superstrate a-Si:H Solar Cells

The degradation of a-Si:H solar cells under light soaking is a major technological problem. To overcome this degradation, new material growth techniques such as ECR deposition and hot wire deposition are being used, both of which show some improved stability of the material when measured in a film. However, there is no previous data on the stability of good quality devices prepared from these materials. Indeed, the deposition techniques used for depositing these materials, such as the use of high temperatures, often make device fabrication difficult. We shall show that a systematic approach to device fabrication, which recognizes the peculiar problems associated with high temperature

fabrication, can lead to devices with good fill factors and efficiencies, and that these devices indeed are more stable then comparable glow discharge devices.

The superstrate cells used in this study were deposited on tin oxide-coated glass. The structure was the usual SnO_2 / p-i-n / Al cell as shown in Figure 4.14. We do not use a highly reflective ITO/Ag back contact because our ITO/Ag contact technology is not very reliable. In particular, we run into fill factor problems (ohmic contacts) with such contact, even though the contact does lead to significant increases in currents. The p-layer was a-(Si,C):H. The i-layer had a buffer layer, followed by the constant bandgap i-layer. All these were fabricated using remote, low pressure ECR discharge technique. As described earlier, in the low pressure ECR technique, an energetic beam of H ions and radicals, produced by the discharge, is directed at the substrate, where Silane is introduced. The energetic H ions and radicals react with Silane, producing SiH_3 radicals, which then leads to the growth of the material.

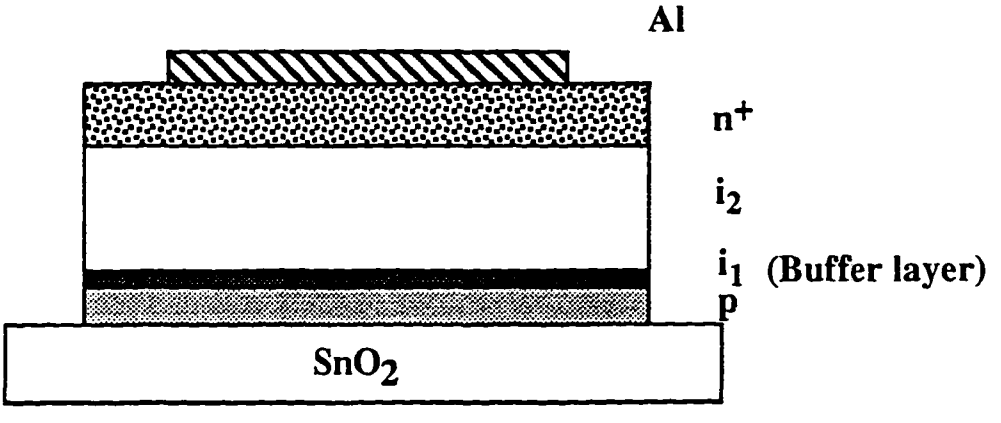

Figure 4.14. Schematic diagram of the superstrate device structure.

Indeed, the typical temperatures for producing the best, most stable films are between 350 and 400°C, significantly higher than that for the case of glow discharge deposition. The combination of high temperatures, and the presence of energetic H ions and radicals, makes device fabrication difficult for standard superstrate p-i-n structures. The problems that we faced in making devices in this high temperature, high plasma density regimes were:

a. *Reduction of SnO_2 at higher temperatures*

At higher temperatures, the H ions and radicals produced by the ECR beam reacted with the SnO_2 substrate, reducing it to metallic tin, which would then diffuse through the device and degrade the performance. This is a non trivial problem even at low temperatures for ECR systems, because the plasma densities one deals with, in the low pressure regime characteristics of the material deposition are very high(10^{10} cm^{-3} range or higher in the ECR one). The high H flux, combined with the high H ion energies, leads to a rapid etching of SnO_2. As an example, in Figure 4.15, we show the ion energies (plasma potential) incident on the substrate of a H-ECR plasma as a function of pressure in the reactor. It is obvious from these figures that the low pressure conditions can provide high fluxes and high energies to the substrate.

To overcome this problem, we make the p-layer using He instead of H_2 as the plasma gas. With He, the only H present comes from the dilution gas of the diborane mixture, and from decomposition of Silane and Methane used to deposit the a-(Si,C):H. Typical dilution ratio with He was 10:1 during the p-layer growth. Also, with He, we can use a much lower power (100 W), and higher pressures (20 mT) than in the case with H plasmas, because the He metastable atom, which is responsible for the fractionation of Silane into the Silyl radical, has a much longer mean free path than the H radical at a given pressure. We find that the combination of low power and higher pressures allows us to deposit the p-layers in a way which is compatible with the SnO_2 substrate.

To make sure that we do not reduce SnO_2 during the deposition of the p-layer, we keep the temperature of the deposition low (about 190°C to 200°C). The growth rate of p-layer was about 0.5°A per second. The typical conductivity vs. bandgap curve for the ECR deposited p -layers is shown in Figure 4.16. We also found that if we increased the temperature of the p-layer (say to the 300°C range), the open-circuit voltages of the devices decreased precipitously. We believe, this is a consequence of catalytic CVD of Silane by Diborane, a reaction whose rate increases with temperature. In such a case, one ends up with a low bandgap mixed B-Si layer, which probably causes problems at the p-i interface, leading to lower voltages.

b. *Boron diffusion from p-layer into the i-layer*

Boron is known to diffuse rapidly into a-Si:H. When a significant amount of B goes into the i-layer severe recombination problems can arise for the electrons generated in the i-layer. To see this, consider the two band diagrams as shown in Figure 4.17. The solid curve shows what the band profile will look like when no B is present in the i-layer, and the broken curve shows the band profile when B has diffused into the i-layer. Therefore when a significant amount of B is present in the i-layer, the electric field in p-i interface region will be less, leading to a reduction in the drift velocity of electrons away from the interface and thus increasing recombination. In addition, the presence of B will lead to the creation of positively charged centers in the i-layer near the p-i interface region and these centers will likely have a higher capture cross-section for electrons and therefore, also lead to increased recombination of electrons in this region. So for both of these reasons, it is not useful to have B in this region.

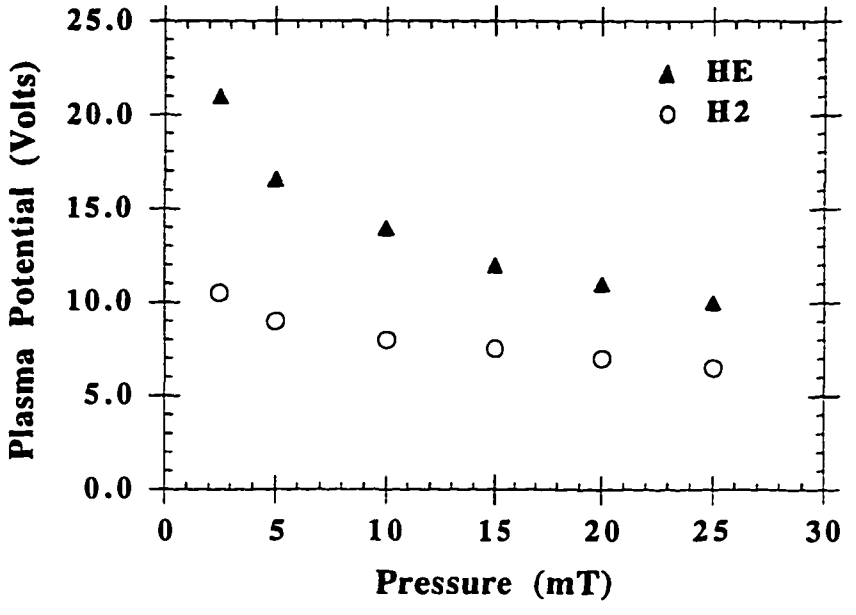

Figure 4.15. Plasma potential in H-ECR discharge as a function of pressure and power.

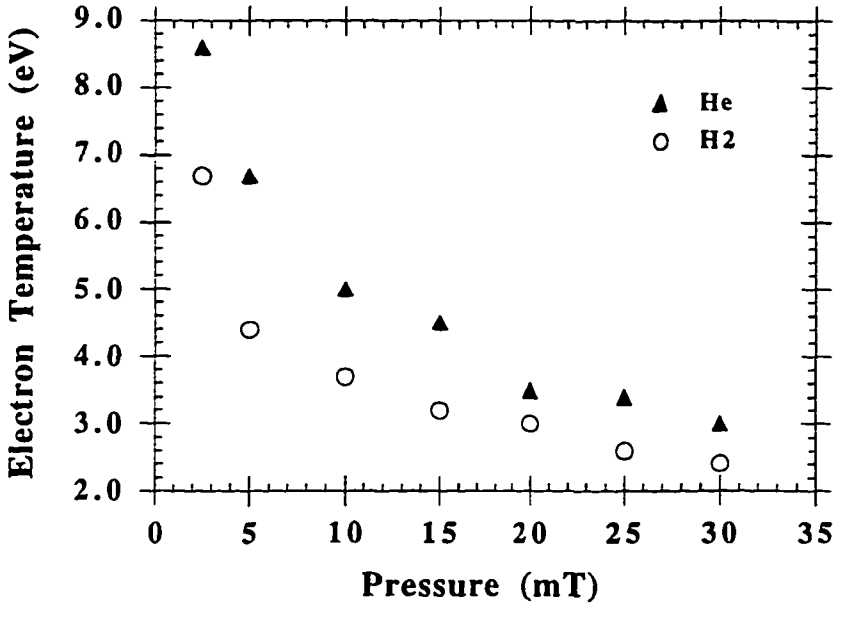

Figure 4.16. Conductivity of B-doped ECR deposited a-(Si,C):H film [52].

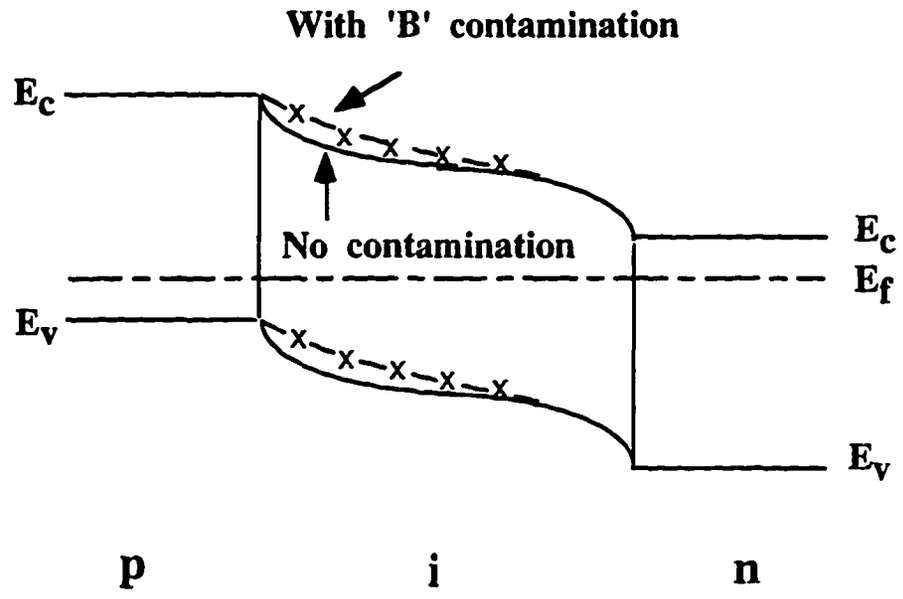

Figure 4.17. Band bending near p-i interface with and without B contamination.

These considerations are borne out by measuring QE of devices, particularly under different bias conditions. As described earlier, one typically finds increased ratio of QE under reverse to zero bias, in this region, when significant B contamination exists. An example of such a QE ratio curve is shown in Figure 4.19, and the corresponding I(V) curve is shown in Figure 4.18. To reduce the B diffusion into the i-layer from the p-layer, we used a high C content (Si,C) buffer layer. We found that diffusion of B is substantially suppressed in a-(Si,C):H compared to the diffusion in a-Si:H . The a-(Si,C):H buffer layer is graded between the bandgap of p-type a-(Si,C):H and i-type a-Si:H.

The design of the buffer layer is critical, in that too little C or too thin a layer leads to diffusion of B, but too much C or too thick a buffer layer leads to inflection points in the I(V) curves, as shown in Figure 4.20. To understand this curve, we measured the QE ratio under zero and forward bias for such a device. Under forward bias, the electric field is reduced significantly in the device, and any recombination problems should be immediately evident.

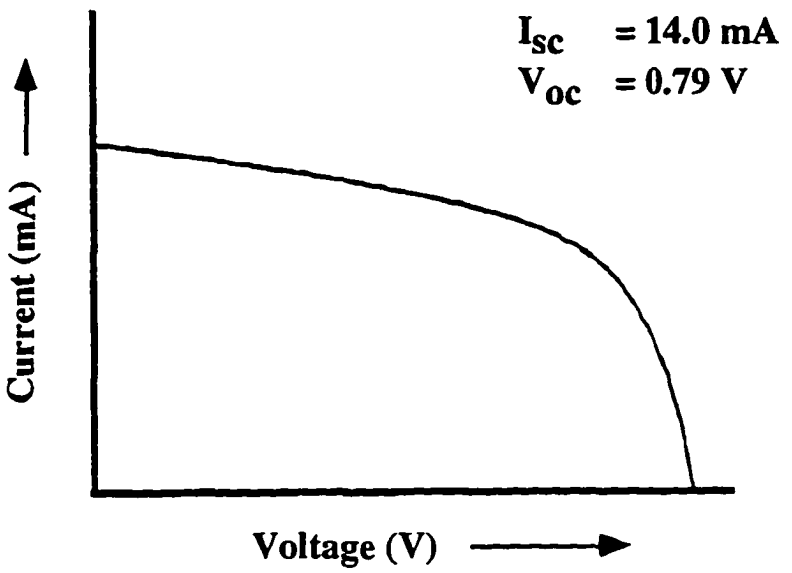

Figure 4.18. I(V) curve of a device with excessive B diffusion.

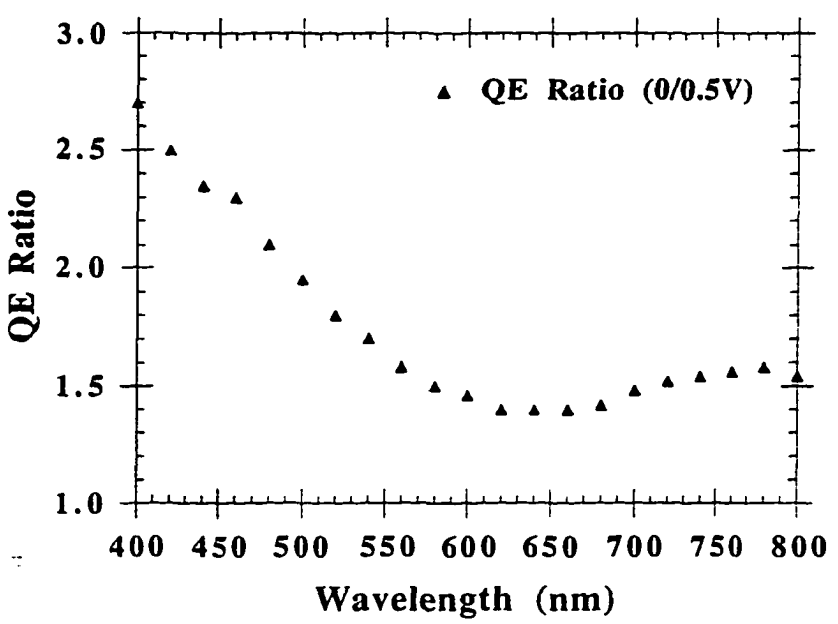

Figure 4.19. QE ratio of the device with the I(V) shown in Figure 4.18.

In Figure 4.21, we show the QE ratio for this device. It is apparent from the curves that a reduction in the field causes a reduction in the carrier collection over almost the entire wavelength range of interest, except for the very short wavelength photons. These short wavelength photons are strongly absorbed in the first few 10nm of the i-layer, whereas photons of longer wavelengths are absorbed over longer distances into the i-layer. From this observation, we can conclude that there appears to be a problem in collecting carriers generated by photons which are absorbed beyond a few 10nm into the i-layer.

This fact is suggestive of a hole-trapping phenomenon as shown in Figure 4.22 [51]. When the bandgap of the buffer layer is too high there may be a notch developing in the valence band between the buffer layer and the i-layer, leading to trapping of holes. Under reverse bias, the field is high enough for the holes to tunnel through the buffer layer, but under forward bias, the decrease in field may result in hole-trapping. Under still stronger forward bias, the holes are being injected from the p-layer into the i-layer and the notch plays no part in the current. Therefore, we get an inflection point in the I(V) curve. A thicker buffer layer makes the problem worse, by reducing the tunneling of holes across the barrier created by the notch.

Thus one has to be very careful when making devices with buffer layers, particularly at high temperatures. The two conflicting requirements of preventing B diffusion, and allowing good hole transport are not always met. Sometimes despite using high C in the a-(Si,C):H layer to block B diffusion, we sometimes get inflection point in the I(V) curve. To overcome this problem of B diffusion and interfacial trapping of holes due to non-matching of valence band between either the buffer and p-layer, or the buffer and i-layer, we thought of using a tapered B profile in the p-layer. What we do is to simultaneously reduce the bandgap of the p-layer and the B content, during the final stages of the p-layer. By doing this, we achieve a graded bandgap that potentially enhances electron collection and also reduces B diffusion by reducing the B content in the source. Then, a very thin, high C buffer layer is deposited to

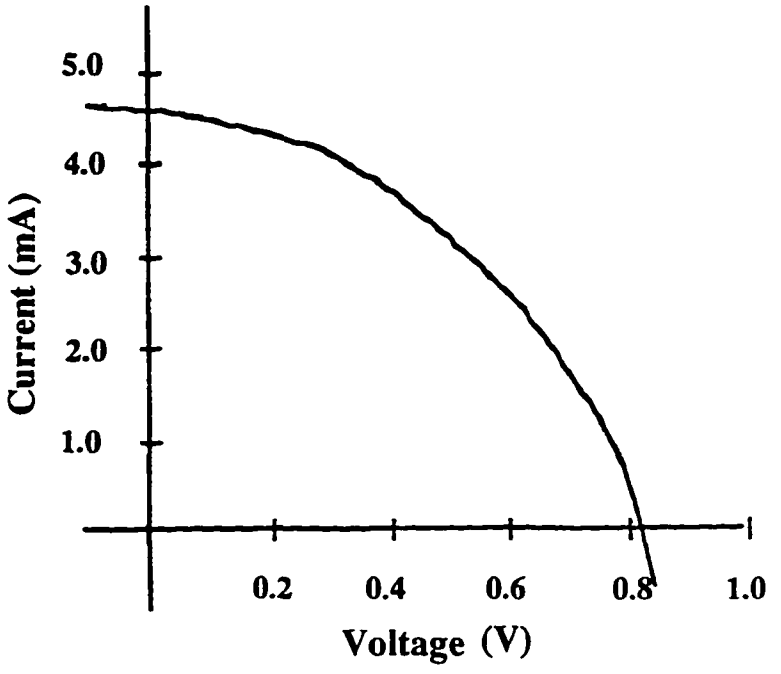

Figure 4.20. I(V) curve of a device with a buffer layer which is too thick. It shows a point of inflection.

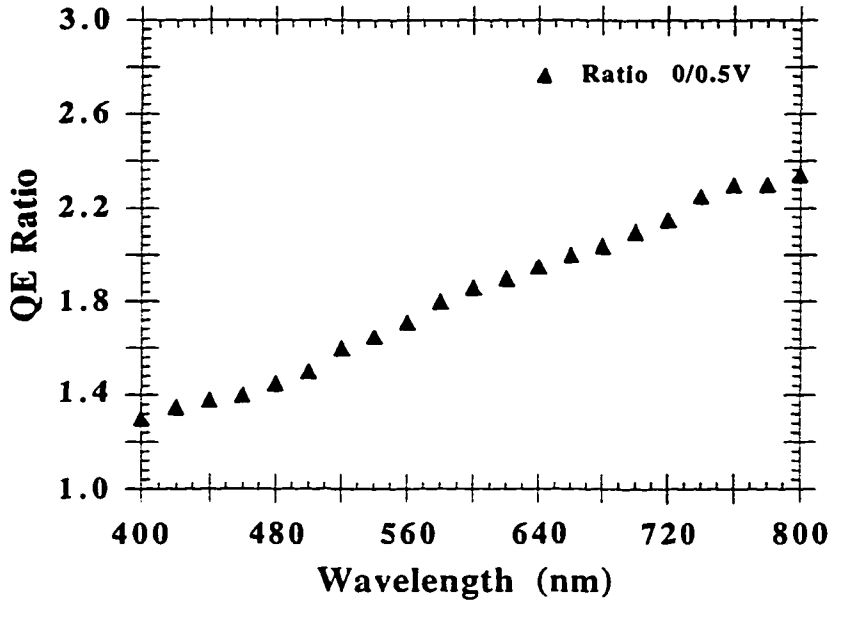

Figure 4.21. QE ratio (0V/+0.4V) for device shown in figure 4.20, showing problems with carrier collection.

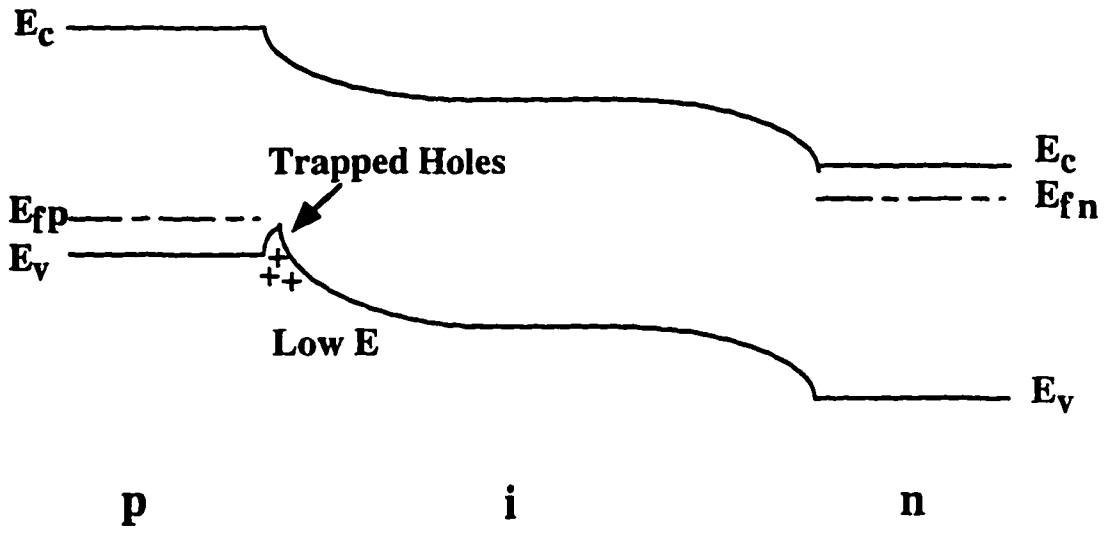

Figure 4.22. Explanation of I(V) curve of Figure 4.7, and QE curve of Figure 4.8, by postulating a notch in the valence band at which holes can get trapped under forward bias [51].

connect the graded p-layer, with the i-layer. This buffer layer is itself graded in bandgap from a high gap near the p-layer to a low a-Si:H gap near the i-layer. We also found that it helps to do a short (15-30 min) controlled diffusion of B at a higher temperature than that of the succeeding i-layer. In general, the fill factor is higher when we do such a diffusion, probably because the B diffuses through any thin interfacial step, thereby, smoothly connecting the p and the buffer layers. Using such careful grading of the p-layer and the buffer layer, we have been able to increase the open-circuit voltage and the fill factor of the cell. Current open-circuit voltages are in the range of 0.8V and the fill factor in the range of 0.66 for i-layers deposited at 350 - 370°C. In Figure 4.23, we show I(V) curve for such a cell of 0.08cm^2 area (V_{OC} = 0.795V, I_{SC} = 11.614mA, F.F = 0.642), and in Figure 4.24 and Figure 4.25, we show the corresponding QE and QE ratio curves. A flat ratio curve is a good indication of the device with good carrier collection i.e a good fill factor.

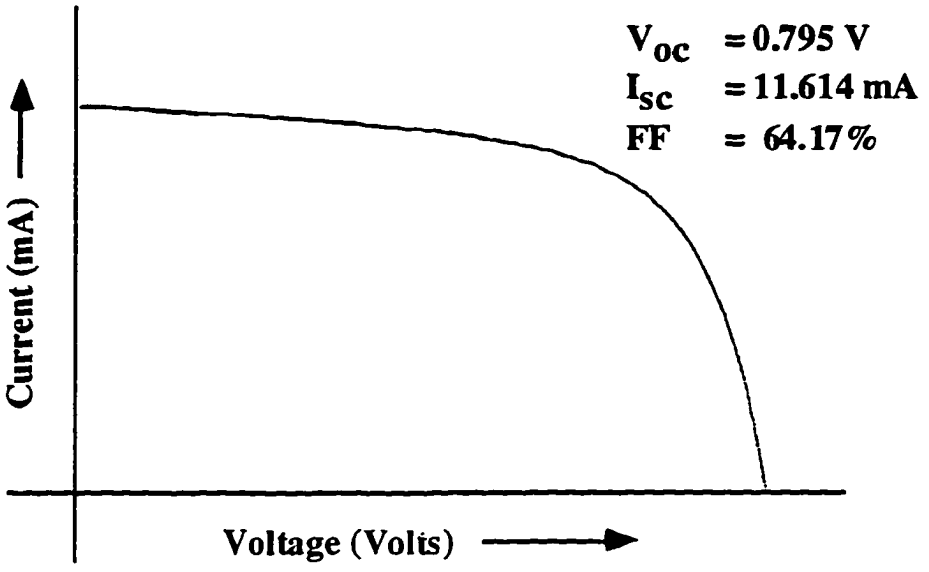

Figure 4.23. Device I(V) curve for a good device.

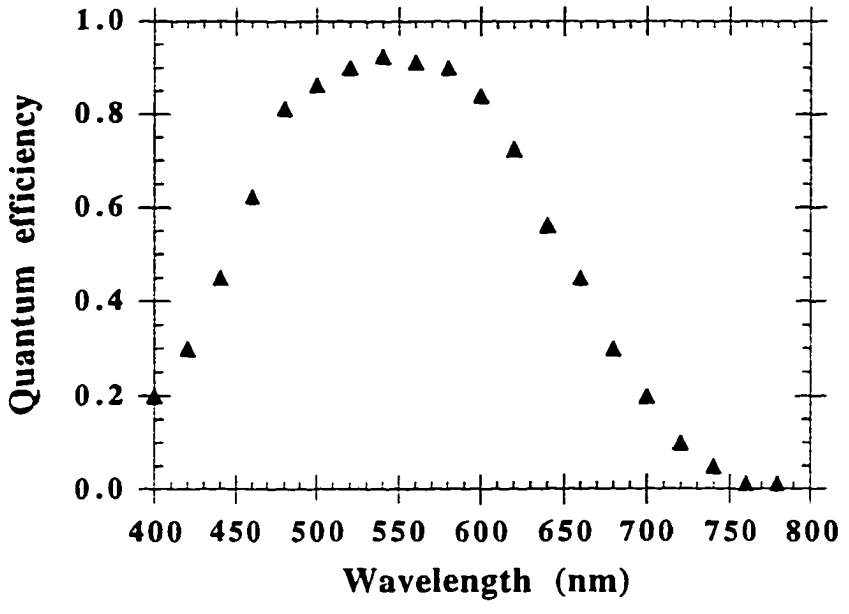

Figure 4.24. Quantum efficiency for device of Figure 4.23.

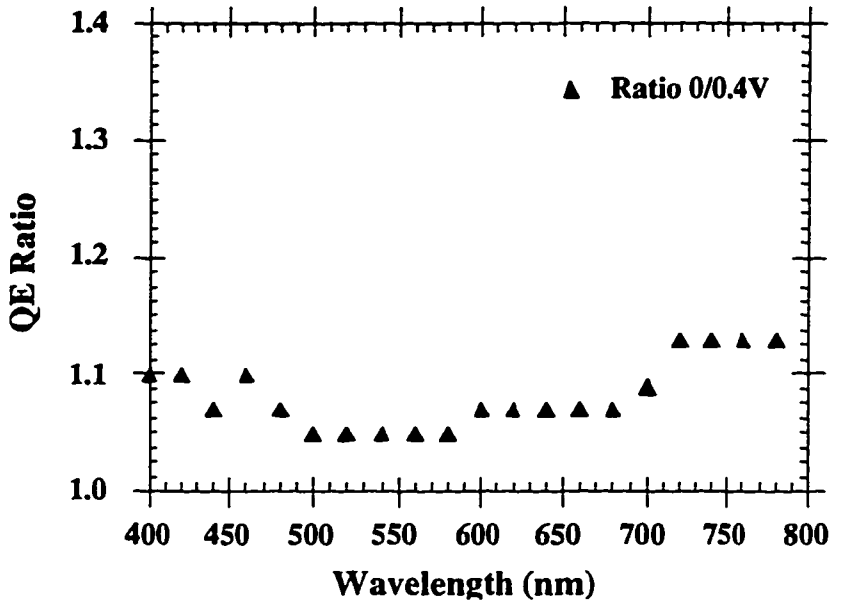

Figure 4.25. QE ratio (QE(0)/ QE(+0.4V) for a device of Figure 4.23.

c. *Problems with tunneling across SnO_2 / p-layer*

Traditionally it has been assumed that a suitable tunnel junction exists between the heavily n-doped SnO_2 substrate layer and the adjacent p a-(Si,C):H layer. However, the limited conductivity of the high gap p-type a-(Si,C):H layer (which is typically used to make the best devices) can lead to serious resistance problems at the interface. In particular, as one goes to non-textured SnO_2 substrates, the resistive loss problem becomes worse. In the worst case, a double diode exists in the device, as illustrated in I(V) characteristics shown in Figure 4.26.

This phenomenon can be better understood by plotting the band diagram of the p-SnO_2 interface (see Figure 4.27). We have used the appropriate work functions or electron affinities described in the literature, for drawing this diagram. It is immediately obvious from the diagram, that the limited conductivity of the high gap p a-(Si,C):H layer leads to a schottky

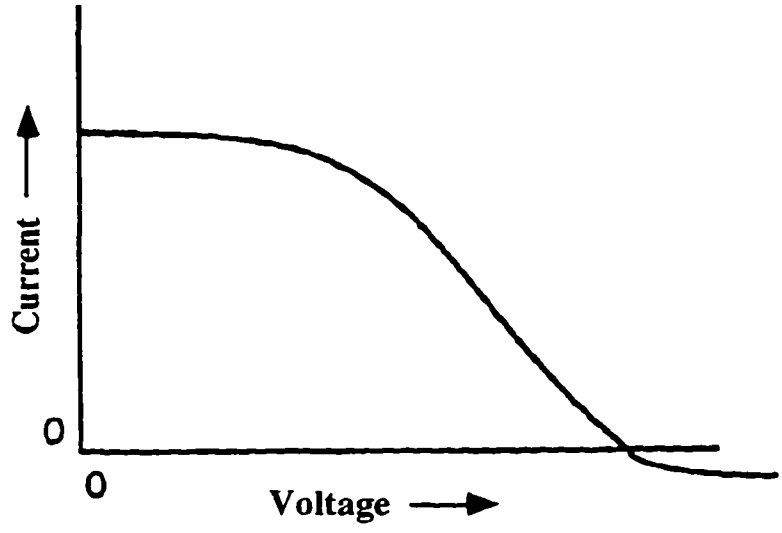

Figure 4.26. A classical double diode type I(V) characteristic.

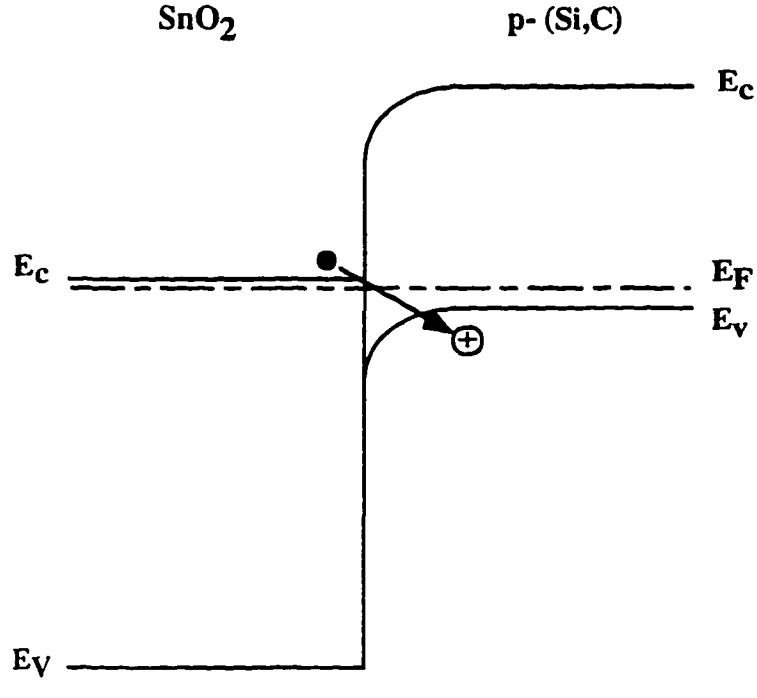

Figure 4.27. Band diagram of p-(Si,C):H/n SnO_2 interface, showing potential tunneling problems which can lead to non-ohmic contact [51].

barrier at the interface whose depletion width extends some substantial amount into the p-layer. As a result, the tunneling of holes from the p-layer into the SnO_2 is impeded, leading to a non ohmic contact to the p-layer. To overcome this problem, we have devised a new structure for the p-layer, where the band gap of the p-layer is kept smaller at the SnO_2 interface and then graded up by changing C:Si ratio as the layer grows (see Figure 4.28). The p-layer next to SnO_2, being of a narrower gap, has s higher conductivity, and hence, the depletion width is shorter, leading to efficient tunneling of holes from the p-layer into SnO_2. Finally, the optimal p-layer design is shown in Figure 4.29. We use such layers for all our devices, whether textured or non-textured substrates.

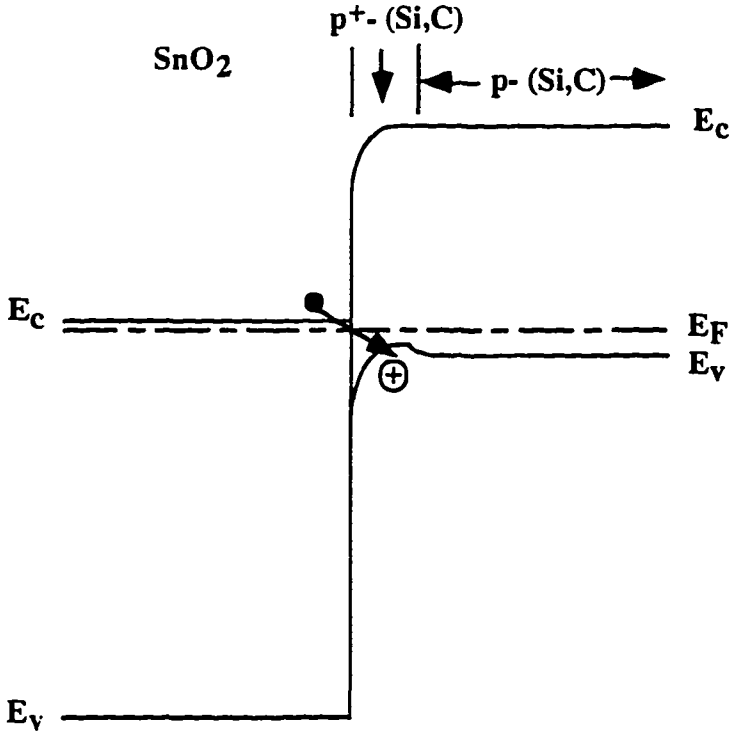

Figure 4.28. Band diagram of a new device structure, interposing a narrower gap p- layer next to the tin oxide. which eliminates double diodes [51].

Since we started using such layers, all the double diode problems have disappeared. In our understanding, this new device structure, which Dr. Dalal has described at NREL team meetings, has now been adopted by many of the university and industrial groups for solving their diode problems.

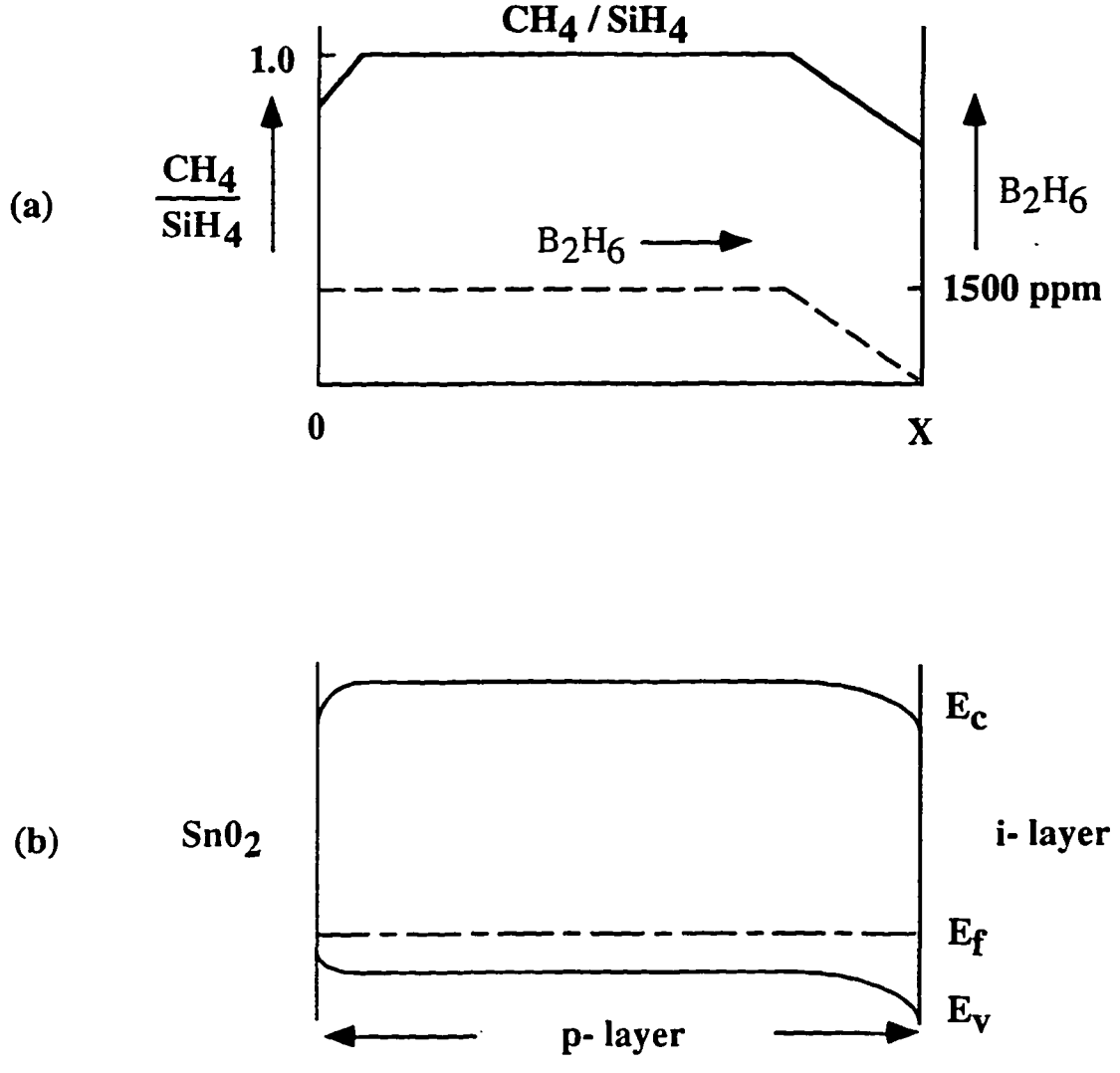

Figure 4.29. (a) Diborane and methane grading in p-layer.

(b) Band diagram of p-layer

2. Device Stability

We have measured the stability of superstarte devices prepared using ECR deposition techniques. At this stage, it is appropriate to comment on how one should measure stability and compare the stability of a new material with the stability of a standard glow discharge deposited cell. The following points should be taken care of before we do any meaningful stability measurements:

1. If we want to compare the stability of a new material for the i-layer in a cell, with that of the i-layer in a glow discharge cell, the two cells must have a comparable thickness of the i-layer. Only then can one compare measurements such as QE and QE ratios, which give us valuable insight into the hole $\mu\tau$ product and electric field profile.

2. It is also essential that the fill factors of the solar cells under comparison be comparable. It makes little sense to compare a cell having 40% fill factor, with another having 70% fill factor. The 40% fill factor cell may show less degradation, but it is already bad to begin with.

3. To study realistic degradation, the amount of light reaching the layers of the cells must be comparable. In particular, this means, using Schottky barriers to measure stability of new material cells, is inconclusive, and may give rise to meaningless results, because light transmission through Schottky barriers varies from one cell to the next. It is only when the green and red external QEs are comparable in the two cells, can one be reasonably sure that approximately, the same number of photons are reaching the i-layer in case and therefore, the recombination is similar in each case.

4. While interface recombination is not generally a major factor in causing instability in normal glow discharge cells, this assumption must be carefully tested for each new material. As an example, for a-(Si,C):H i-layer cells, this assumption may not be valid.

5. Finally, the spectrum of illumination may also matter, especially, if the interfacial instability is important in a given cell. In particular, having a blue-poor spectrum lamp for light soaking, may give a false reading for certain kinds of cells.

We now describe the results of light soaking tests performed on two nearly identical cells, one prepared using glow discharge deposition, and the other using ECR deposition. We tried to keep the two cells comparable, by having the same voltages, fill factors, and QEs. We also tried to match the red QEs of the two cells, by keeping the thickness of the i-layer the same in each case. Each cell had similar Tauc gap of 1.75 eV. In Figures 4.30 and 4.31, we show the initial I(V) curves of the two cells, and in Figures 4.32 through 4.35, the QE and QE ratios. It is clear from this comparison, that the two cells are very similar. Each cell has a good fill factor of about 67%. Each cell had an Al back-contact.

The two cells were light soaked using ELH lamp at 3000 W/m^2 intensity. The changes in the parameters of the cells after the light soaking are shown in Table 4.3. In the Figures 4.36 to 4.39 we show the relative degradation in current, voltage, and F.F, for each cell.

Table 4.3. Comparison of degradation of ECR and glow-discharge cells.

		Jsc (mA/cm^2)	Voc (Volts)	FF	Power (mW/cm^2)
GD	Annealed	13.1	0.76	0.67	6.67
	Degraded	11.8	0.725	0.53	4.53
	Degradation	9.9%	4.6%	20.9%	32.1%
ECR	Annealed	11.2	0.76	0.665	5.66
	Degraded	10.5	0.765	0.605	4.86
	Degradation	6.3%	0.7%	0.9%	14.1%

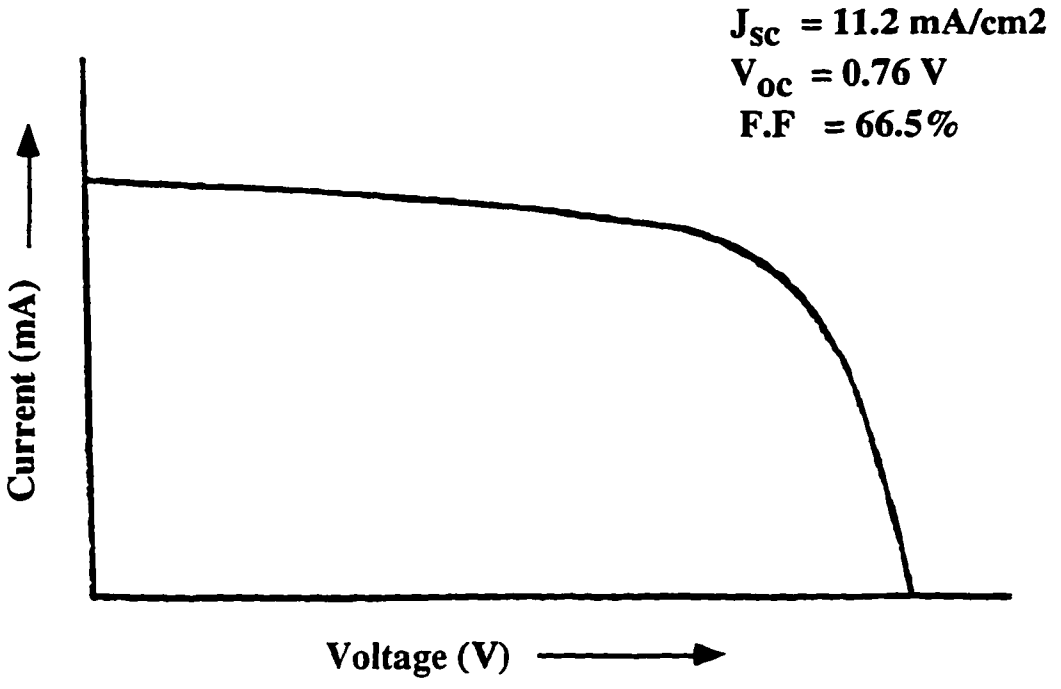

Figure 4.30. Initial I(V) curve of ECR cell selected for stability measurements.

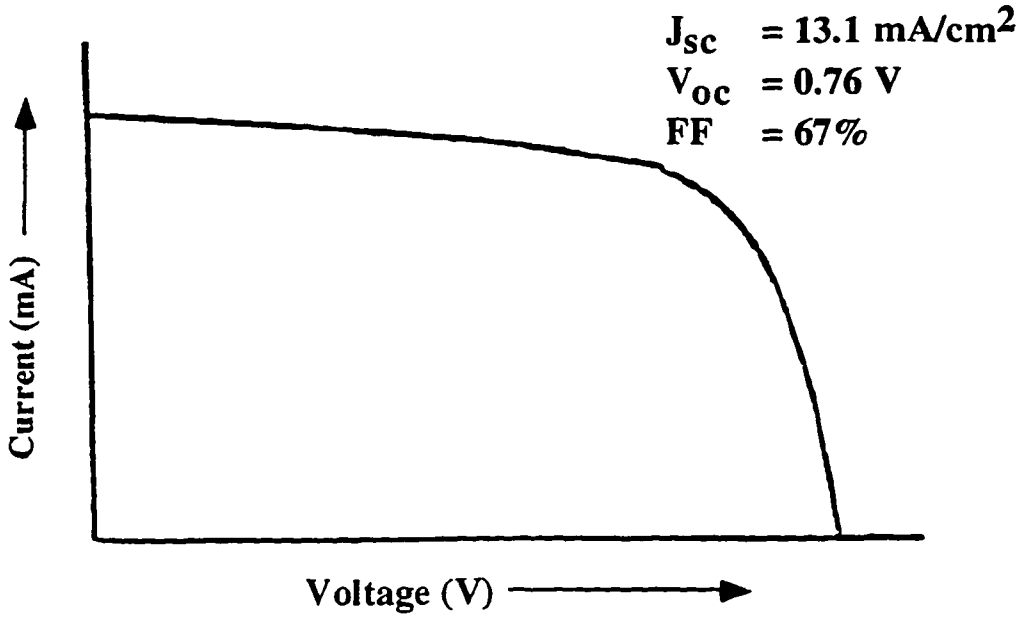

Figure 4.31. Initial I(V) curve of glow-discharge cell selected for stability measurements.

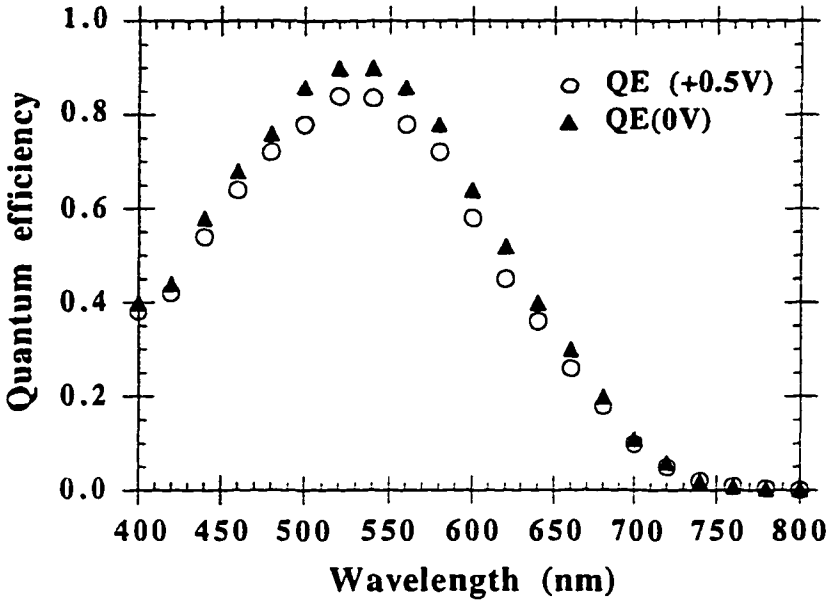

Figure 4.32. Initial quantum efficiency curve for the ECR cell.

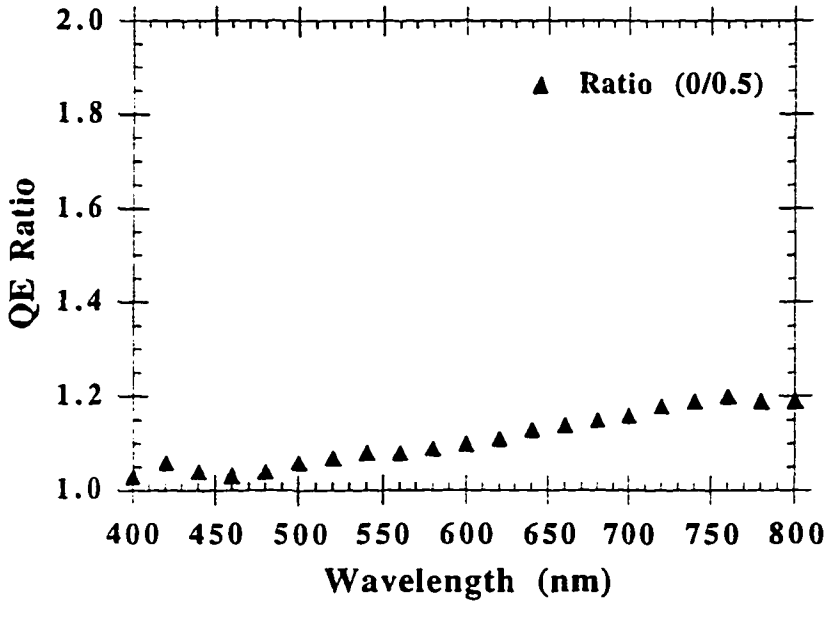

Figure 4.33. Initial quantum efficiency ratio curve for the ECR cell.

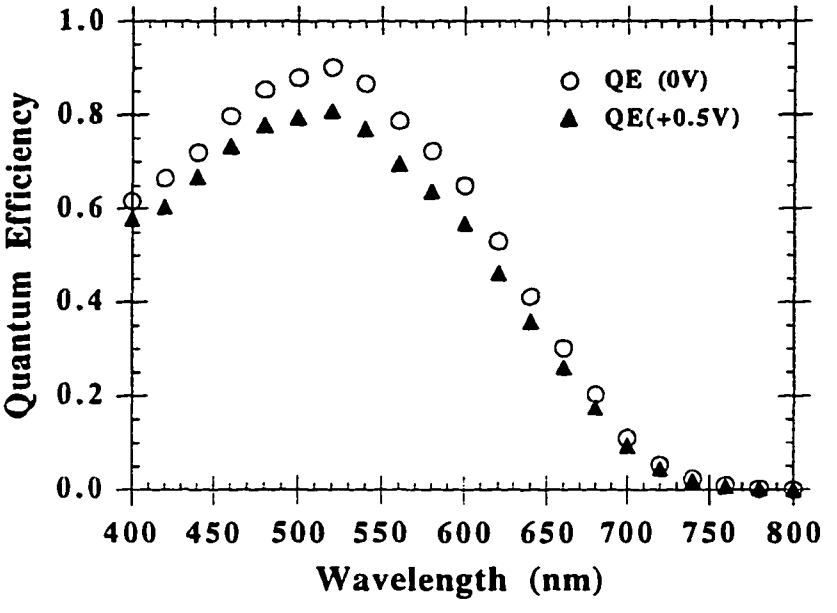

Figure 4.34. Initial quantum efficiency curve for the GD cell.

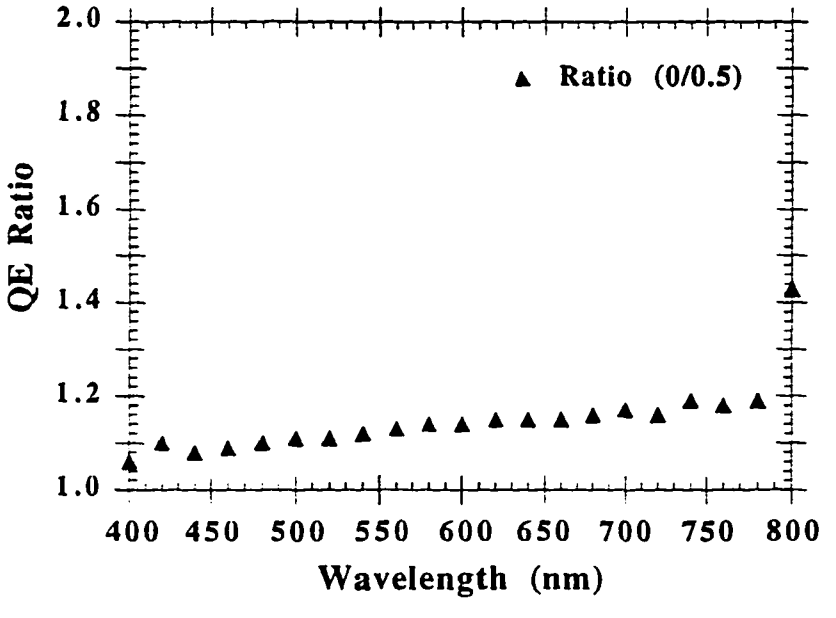

Figure 4.35. Initial quantum efficiency ratio curve for the GD cell.

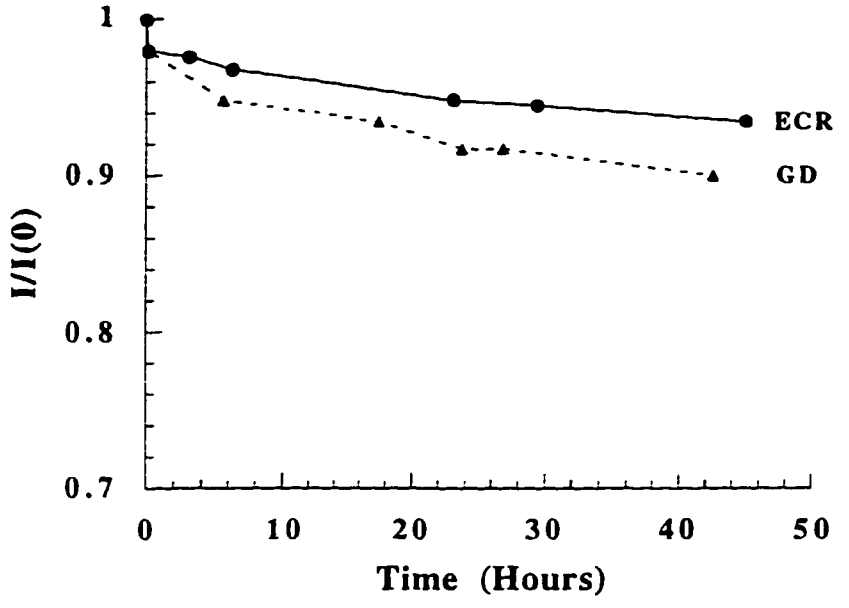

Figure 4.36. Changes in current of ECR and GD cells as a fuction of light soaking time .

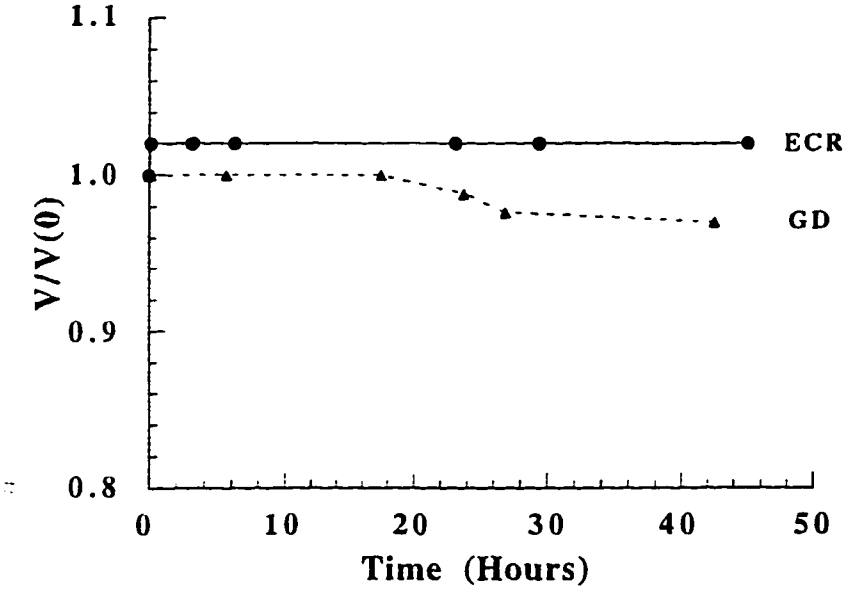

Figure 4.37. Changes in voltage of ECR and GD cells as a fuction of light soaking time .

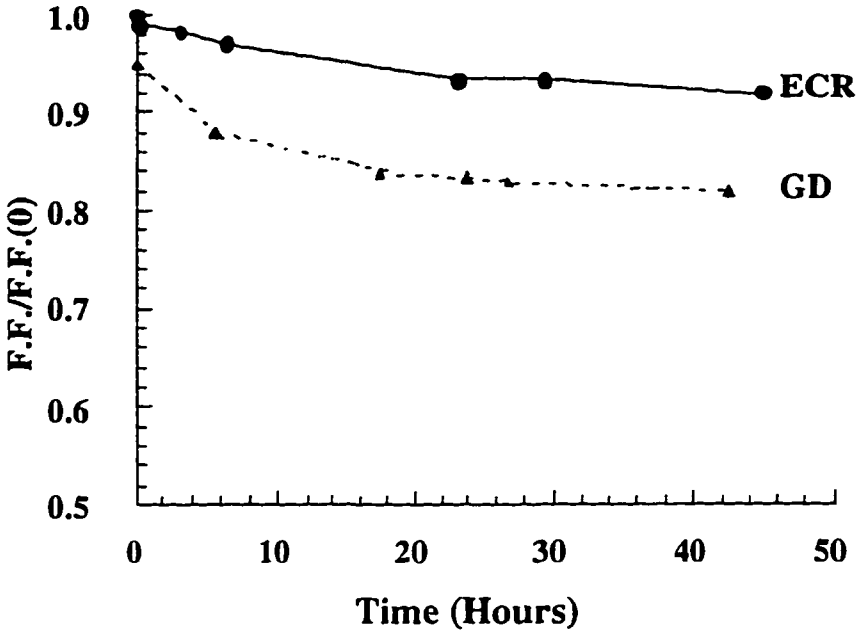

Figure 4.38. Changes in fill factor of ECR and GD cells as a function of light soaking time .

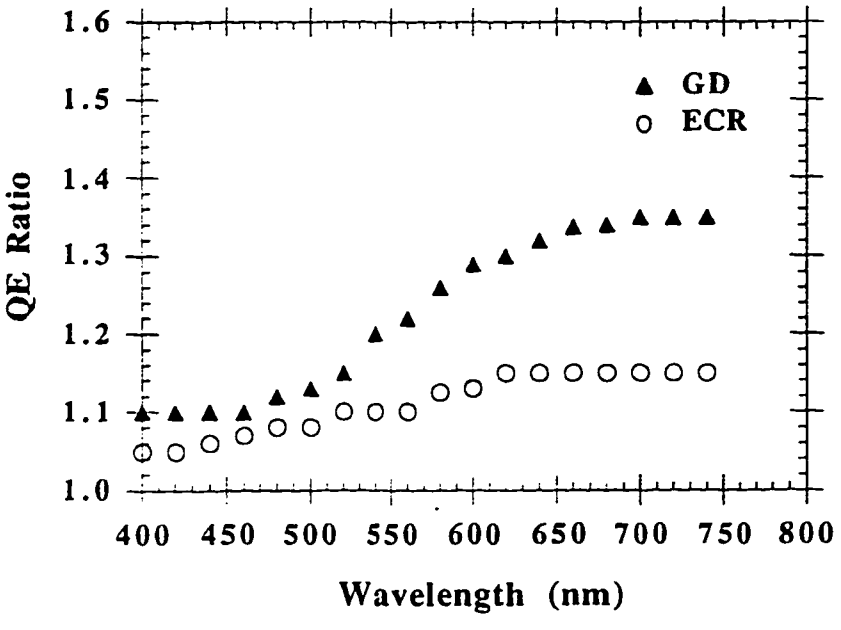

Figure 4.39. Quantum efficiency ratio for GD and ECR cells after degradation.

It is seen that the cell produced using ECR deposition is much more stable than the glow discharge produced cell. In Figure 4.39, we show the QE ratio (ratio of QE at 0V to QE at +0.4V) for each of the two cells, after degradation. It is clear from Figure 4.39 that the ratio for the glow discharge cell is much higher than that for the ECR cell, a clear indication that the holes in the glow discharge cell needs a greater field-assist for collection. This fact suggests that the hole $\mu\tau$ product has degraded more in the glow discharge cell than in the ECR cell. This, in turn, means that the i material in the ECR cell has degraded less than the i material in the glow discharge cell. Thus, indeed, the ECR material is more stable than the glow discharge material even when incorporated in a cell.

3. Substrate a-Si:H Solar Cells

We had discussed the design of a-Si:H solar cells made using ECR deposition on superstrates(tin oxide substrates) in the previous section. We obtained good fill factors (67 %) but the voltages were low (0.8V). It was also seen that the cells appeared to be more stable than comparable glow-discharge solar cells with the same thickness of i-layer and the same fill factor. We had also come to a conclusion that there were several problems that were to be solved before solar cells could be made at higher temperatures on superstrates. Among these problems were:

(a) Reduction in tin oxide by high intensity hydrogen plasma

(b) Diffusion of Boron from p-layer into i-layer

While we had successfully solved these problems at lower temperatures (up to about 360°C), it became progressively more difficult to solve the diffusion problem as the growth temperature was increased. In particular the low voltages led us to believe that perhaps something else was happening (eg. diffusion of Na from the glass into a-Si, which would lead to lower conductivity in the p-layer, and hence a lower voltage). We also know that the best

voltages are obtained using microcrystalline p layers, but these layers are very difficult to make on the tin oxide substrate, since the very thin p-layer used for solar cells almost always tends to be amorphous when deposited directly on tin oxide.

While one can think of creative solutions to these new problems (eg. new Na blocking layers between tin oxide and the glass substrate), it is perhaps more appropriate to prove that good voltages, fill factors and stability can be obtained using ECR deposition on substrates where the diffusion problems do not exist. Therefore we decided to investigate the design and optimization of the substrate cell structure: stainless steel /n/i/p/ semi- transparent contact (see Figure 4.40).

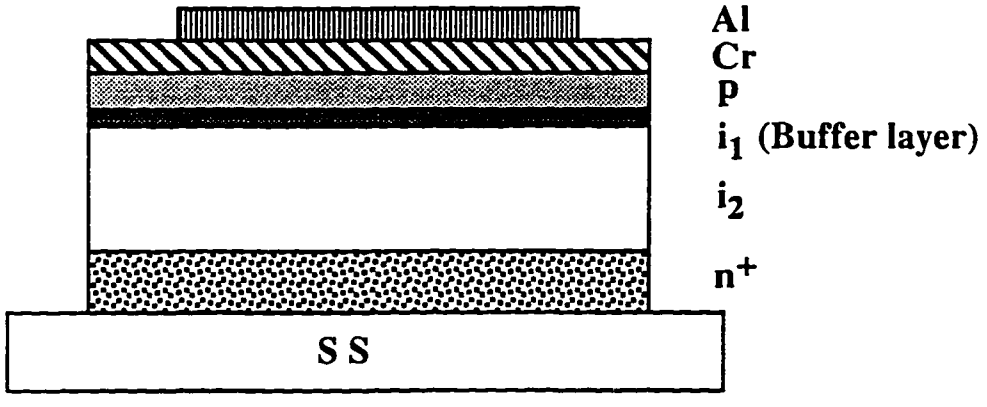

Figure 4.40. Device structure for substrate cells.

In such a design, there is no problem with diffusion of B since the p-layer is the last layer deposited before contacting, and it can be deposited at a low temperature(eg. 200°C), following the rest of the layers which are deposited at higher temperatures. The problem with diffusion of Phosphorous from the n-layer into the i-layer is much less acute than the problem of Boron diffusion because of two reasons:

(a) The diffusion coefficient of Phosphorous is less than that of Boron

(b) Any small (eg. 100°A) diffusion of Phosphorous into the rear of the i-layer will not critically impact the cell, unlike the catastrophic effects of B diffusion into the first 100°A of the the i-layer as discussed earlier.

Using the stainless steel as the substrate also avoids the problems associated with Na diffusion from a glass substrate.

a. Device fabrication procedure

We use the structure as shown in Figure 4.40, namely: learning from the experience of fabricating substrate cells on GD system , the following structure is used for deposition in ECR system: ss / pre deposited n^+ layer / thin in-situ n layer / i / buffer / p /Cr / Al.

The cells were made at temperatures ranging from 300°C to 425°C , on bright polished (but not electroplated) 200 μm thick stainless steel substrates. The deposition process that seemed to work best was:

(1) Pre-deposit n^+ layer of about 1000°A in a separate step (usually in the glow discharge reactor) . This is done so that we can reduce the contamination to controllable limits in our single chamber ECR reactor .

(2) Follow this n-layer with an in-situ n-layer of about 2 minutes duration (about 100 - 120°A). This step is undertaken so as to overcome any thin interfacial oxide layer formed during the transfer of substrate from one reactor the other.

(3) Do a thorough purge and evacuation cycle to remove PH_3.

(4) Do a plasma etch with Hydrogen, followed by a dummy 2 min. p-layer deposited on the reactor walls with the shutter closed. The effect of this will be illustrated when we discuss the device results.

(5) Do another thorough purge and evacuation cycle to remove B_2H_6.

(6) Do a low power Hydrogen plasma etch for 2-3 min with shutter open, followed by a plasma clean of the reactor for about 25-30 minutes.

(7) Deposit i-layer: the deposition conditions:

Silane flow: 10% / 20%

H_2/He flow : 20% /100%

Temperature : 300°C - 425°C

Pressure : 10mT for H_2 as plasma gas / 25 mT for He as plasma gas

Growth rate : 1-2°A/sec

Total thickness of i-layer : 3500°A - 4000°A

(8) Deposit a graded gap a-(Si,C) buffer layer at 300°C

(9) Deposit p layer at 200°C

(10) Deposit Cr dot (~ 100°A) followed by Al busbar (1000°A)

b. Device results

In Figure 4.41 we show the I(V) curve of the cell which was fabricated using hydrogen-ECR discharge with a straight forward procedure i.e. we did not make any dummy p-layer or use any kind of sub p-p-m compensation. Note in particular, the voltage (0.79V) , through a 20% (or less) transmitting Cr layer. This means that the voltage through an appropriate ITO layer would be at least 1.5kT/qln5, or about 62mV higher, for a total 852 mV. (The above equation used a diode factor of 1.5). This is significantly higher than what we obtained in our best superstrate cells and this without optimization of p-layer. We can estimate what the voltages would be in a cell subjected to full illumination by measuring V_{oc} vs.log(Jsc). Such a plot is shown in Figure 4.42. The curve also gives us the diode ideality factor which in our case is 1.2.

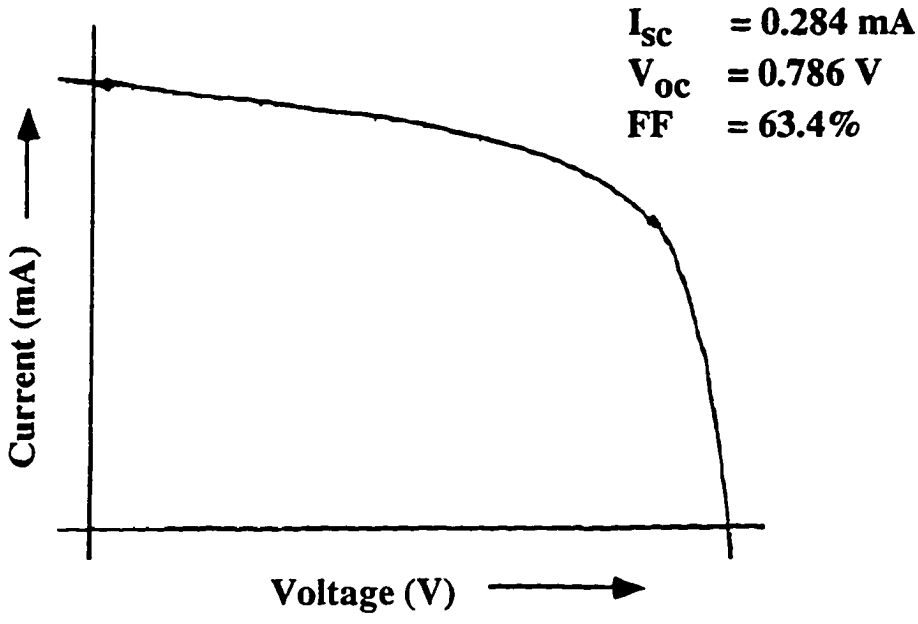

Figure 4.41. I(V) curve of ECR cell. The Cr is only about 20% transmitting.

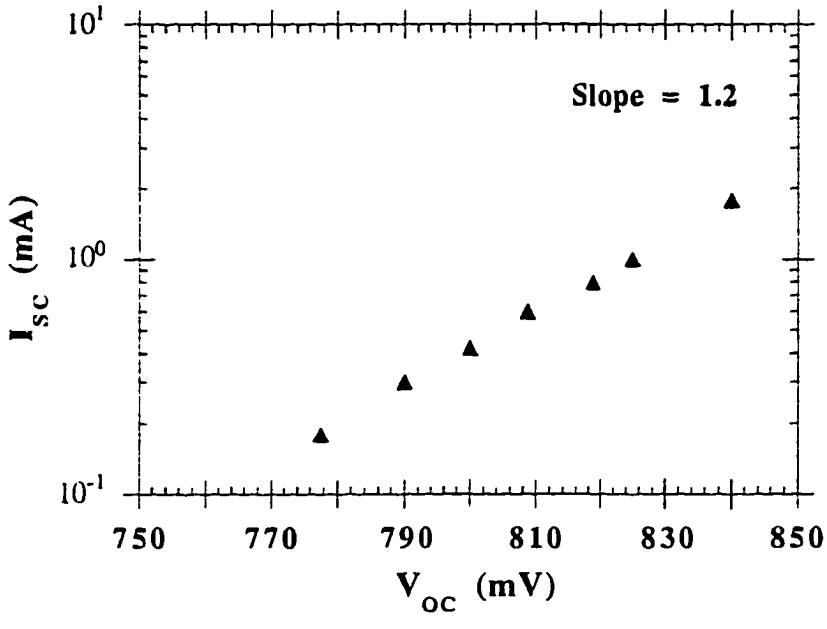

Figure 4.42. Log of short circuit current vs. voltage. The slope gives a diode factor of 1.2.

The fill factor (63%) is somewhat less than the comparable superstrate cell. To see the reason why, we show the QE and QE ratio curves in Figure 4.43 and Figure 4.44 respectively. The QE ratio curve is not flat, but it increases towards longer wavelengths and specifically it increases to about 1.2 in the 700nm range. This is usually an indication of problem with hole collection. Since superstrate cells made at the same temperature had high fill factors and did not have any phosphorous contamination in the reactor , we are motivated to conclude that the very energetic ECR plasma is still getting some phosphorous off the walls of the reactor and incorporating it in the i-layer during deposition. Further support for the supposition that the i-layer by itself is good, comes from the subgap QE results. It will be recalled that a measurement of QE vs. photon energy gives an indication of the Urbach energy of the valence band in the material, a fundamental material constant.

For best cells, as discussed earlier, we need low Urbach energies, since higher values indicate higher defect densities. In Figure 4.45 we show the subgap QE curve of this device as a function of photon energy, with an estimated Urbach energy of about 43meV, a value similar to what we obtained in superstrate cells with good fill factors. Thus the material itself appears to be very good, but somewhat contaminated with low levels of P. Quite clearly we had to develop an appropriate reactor cleaning technique to eliminate this problem.

Basically, we decided to minimize P contamination by minimizing the growth time of the n-layer in the reactor. As such, we do two n-layers, a thick (0.1μm) layer in a glow discharge reactor, followed by an in-situ 100°A n-layer in the ECR reactor. Then we do a thorough purge and a hydrogen plasma etch of the reactor, and the substrate holder, prior to depositing the i-layer. This hydrogen etch is a critical step in the process. By using such techniques, we could minimize the phosphorous contamination to a certain extent but more was desirable.

The innovative solution that we came up with so as to get best results involved adding 100% 10ppm TMB during plasma clean. We found that to get the best results, we had to

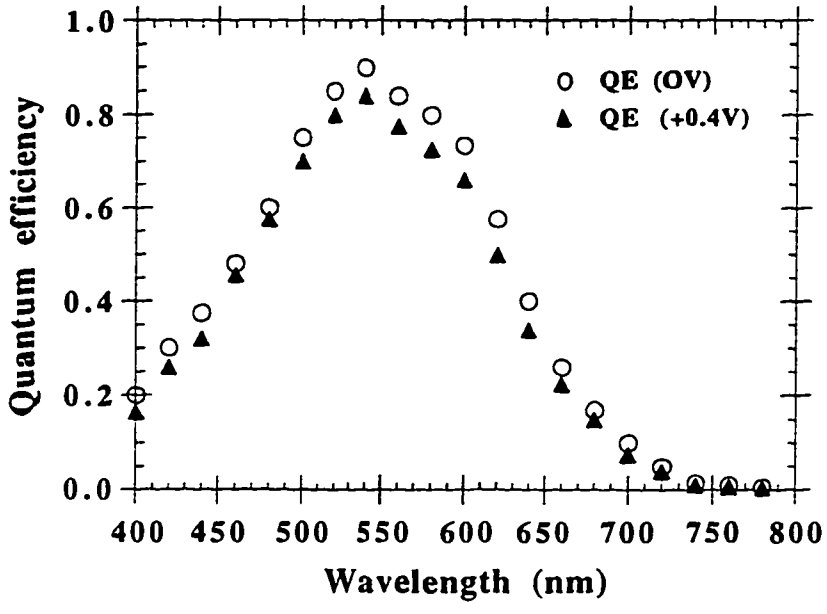

Figure 4.43. Quantum efficiency of a ECR cell whose I(V) is shown in Figure 4.41.

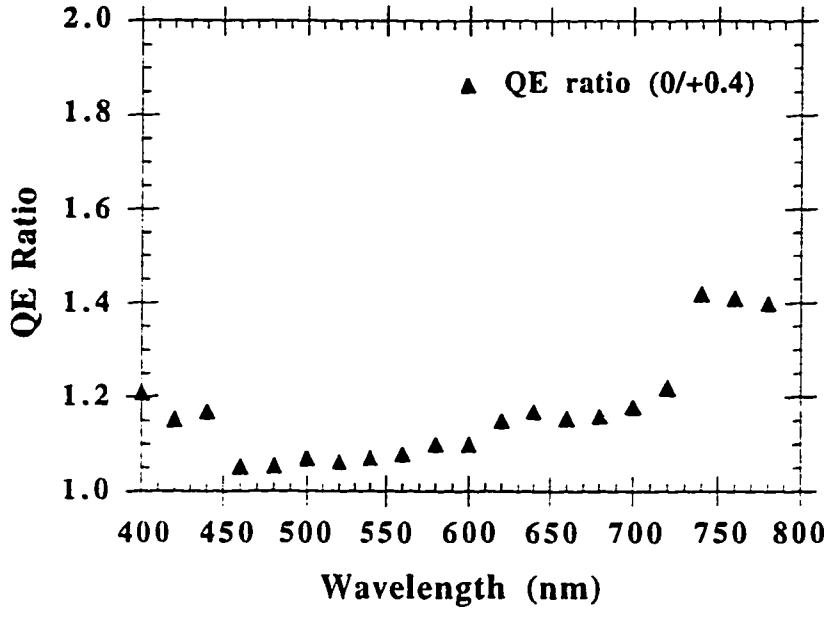

Figure 4.44. Quantum efficiency ratio of a ECR cell whose I(V) is shown in Figure 4.41.

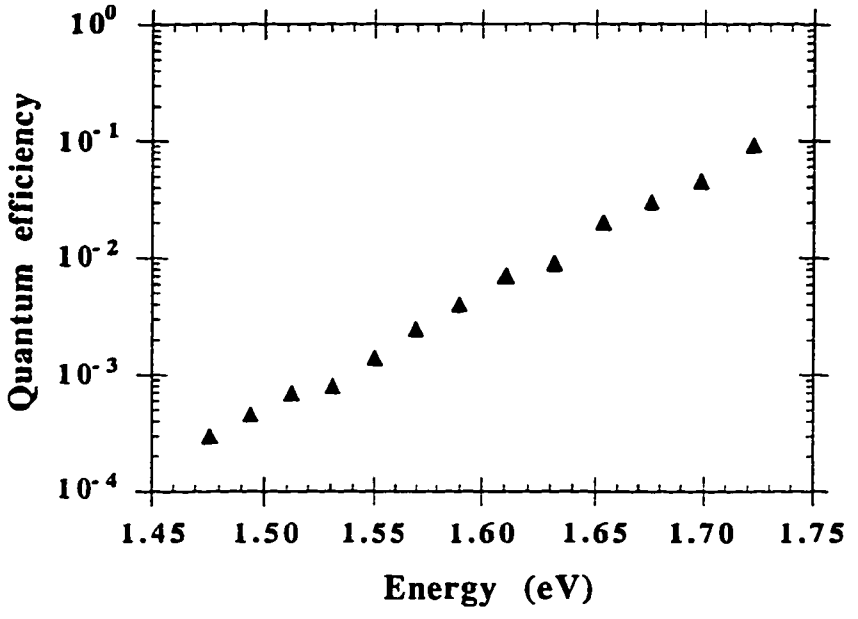

Figure 4.45. Subgap QE of ECR ss/n/i/p device.

compensate the i-layer with very small amounts of B, using trimethyl Boron diluted in hydrogen as the compensating gas. Typically, the compensation was at the sub-ppm levels (0.2-0.4 ppm), similar to the results we reported some time ago on stability of compensated films [52]. We noticed immediate improvement in the results. For instance, the cell , namely 2/1854 with everything the same as the cell 2/1845 discussed earlier, except that in this case 20%, 10ppm TMB compensation was used during the deposition of i-layer. This made a remarkable difference in fill factor as shown in its I(V) curve (Figure 4.46). The fill factor improved to 68% i.e. an increase of about 5%. We also see that now the QE ratio curve (QE curve of this device is shown in Figure 4.47) as shown in Figure 4.48 is flat throughout the wavelength range of interest. The Urbach energy was about 44meV, indicating a high quality i-layer material. We then fabricated a series of devices shown in Table 4.4 to optimize the amount of compensation needed to give the best results.

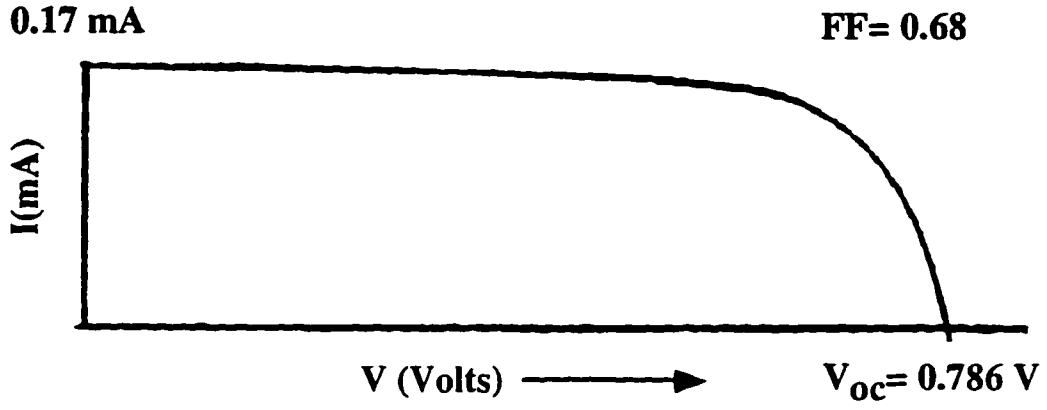

Figure 4.46. I (V) curve of a Cr/p/i/n/ss solar cell deposited using Hydrogen ECR technique. The fill factor and voltage are meaningful; the current is not, because of absorption in the top Cr contact.

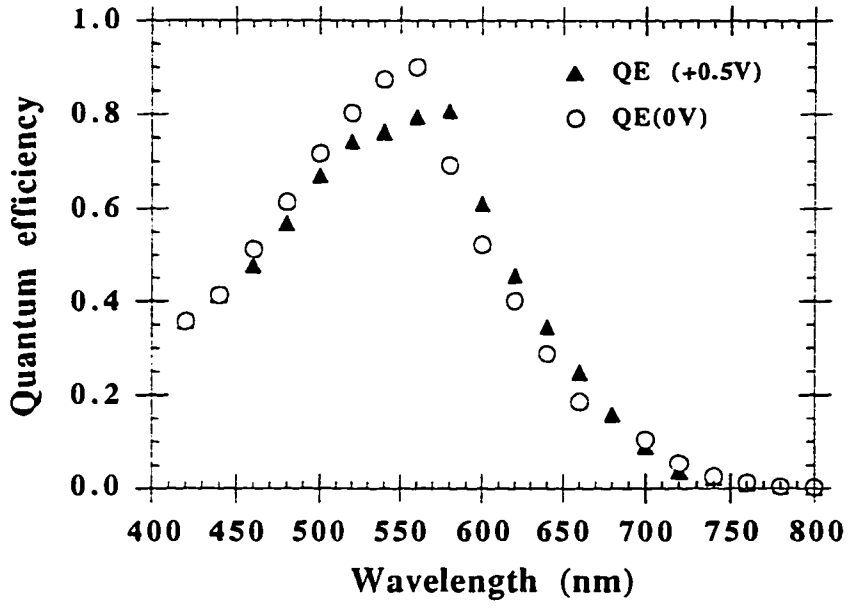

Figure 4.47. Quantum efficiency curve of a substrate cell whose I(V) is shown in Figure 4.46.

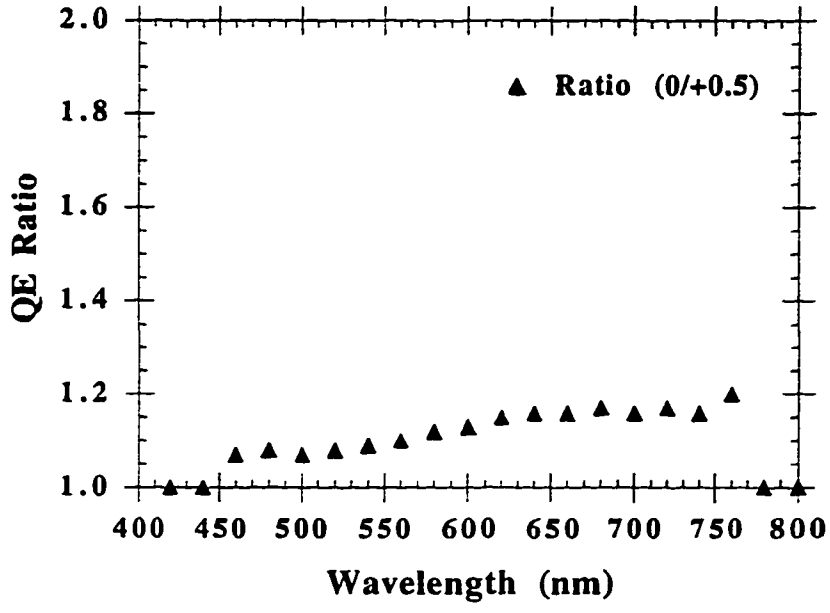

Figure 4.48. QE ratio curve of a substrate cell whose I(V) is shown in Figure 4.46.

Table 4.4. Devices fabricated for compensation studies.

Device #	I-layer Parameters			V_{oc}	FF
	SiH4	H2	10ppm TMB	(V)	(%)
2/1859	20%	17%	15%	0.8	64%
21854	20%	16%	20%	0.786	68%
2/1858	20%	15%	30%	0.8	62%

From Table 4.4, we see that if we overcompensate, the fill factor deteriorates. Thus we conclude that a limited amount of ppm TMB could be used to enhance the performance of the substrate solar cell. We can explain these results by invoking Redfield's rehybridized two site model. He suggested that the native impurities like P, N etc. act as donors. They can be

bonded either in 4-fold coordinated bond or as a 3-center bond. If they are bonded as a 3-center bond , they lead to increase in both initial and light soaked defect densities. We suggest that by incorporating B, during growth, we are compensating these donors, and that it may be forming a donor-acceptor pair, thereby preventing the formation of a 3-center bond, and therefore reducing the initial and light-soaked defect densities. Too much B leads to overcompensation, formation of B based 3-center bonds, and more defects. Clearly the results that we have seen can be supported by this hypothesis.

We also did a series of runs to see the effect of temperature of growth of i-layer on the performance of the substrate solar cells. The results are presented in Table 4.5.

Table 4.5. Devices faricated for temperature studies.

Device #		I-layer	Parameters	V_{oc}	FF	E_u
	T(°C)	$SiH4/H_2$	10ppTMB	(V)	(%)	(meV)
2/1871	350	17/20	15	0.78	63	46
2/1874	375	17/20	15	0.78	64.5	47
2/1891	300	17/20	15	0.78	65	43

From above we can see that the change in temperature does not affect the initial characteristics of the solar cells very much. But we are yet to conduct the stability tests to comment on the effect of temperature of growth on the performance of the cells. It is expected that devices grown at high temperatures will be more stable.

The next step in the development of the substrate solar cells was their fabrication using He ECR discharge. As explained earlier, using He we can reduce the bandgap of the i-layer to about 1.66eV , which has its own advantages. But this reduction in bandgap and the different plasma characteristics of He discharge presented us with distinctly new problems. We found

that we had to alter the buffer layer between the p and the i-layers slightly in order to get better matching between the lower gap i-layer and the standard p-layer. If we did not do that, we obtained poor I(V) curves. When we measured the QE and QE ratio curves, we found that the problem lay not in the i-layer, but at the p-i interface, as shown in QE ratio curve plotted in Figure 4.49. There, we clearly observe that QE ratio is high for short wavelength photons, a classic signature of excess recombination of electrons at p-i interface. In contrast, when p-i buffer layer is adjusted to account for the lower sap of the i-layer, normal I(V) curves with very high fill factors (72%) are obtained (Figure 4.50). The corresponding QE, and QE ratio curves, shown in Figures 4.51 and Figure 4.52, clearly show that there is no collection problem with either holes or electrons in this case. Details of above devices are shown in Table 4.6.

Table 4.6. Devices fabricated for bandgap studies.

Device #	I-layer	parameters		V_{oc}	FF
	T(°C)	SiH_4	He	(V)	(%)
2/1934	425	20%	100%	0.77	66
2/1947	425	10%	100%	0.76	65

To see if indeed the bandgap shift is also observed in devices, and to study the quality of devices, we measured subgap quantum efficiency in the devices made using hydrogen or helium. We have shown earlier that subgap QE gives an accurate measurement of Urbach energies of the valence band tails[53], and can also be used to find out the shift in the bandgaps. As the bandgap decreases, the subgap QE, for a device with an identical i-layer thickness, should also shift to lower energies, with the two curves remaining parallel. In Figure 4.9, we show the subgap QE for the two cells, with identical thicknesses of the i-layer,

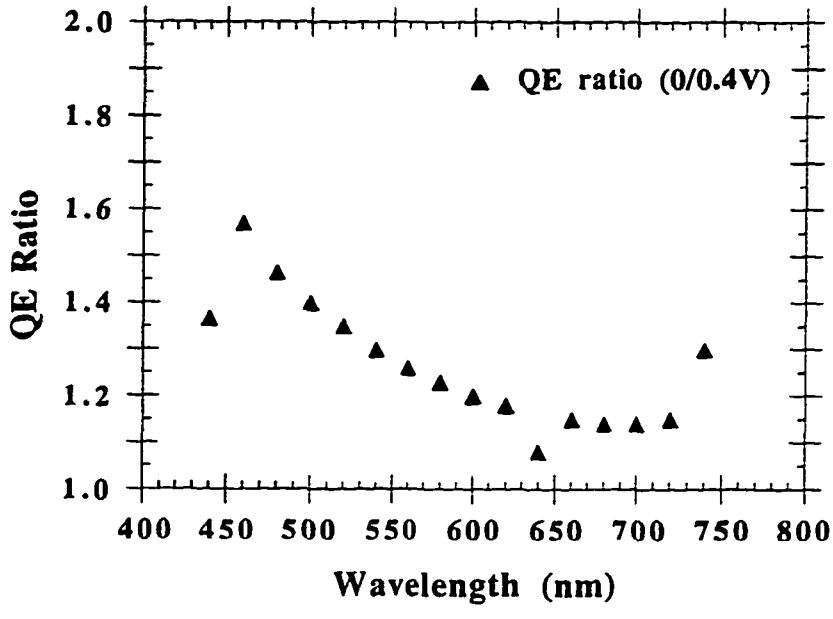

Figure 4.49. QE ratio for a He-deposited ECR cell when an improper buffer layer was used between the low gap i-layer and the higher gap p-type a-(Si,C):H layer.

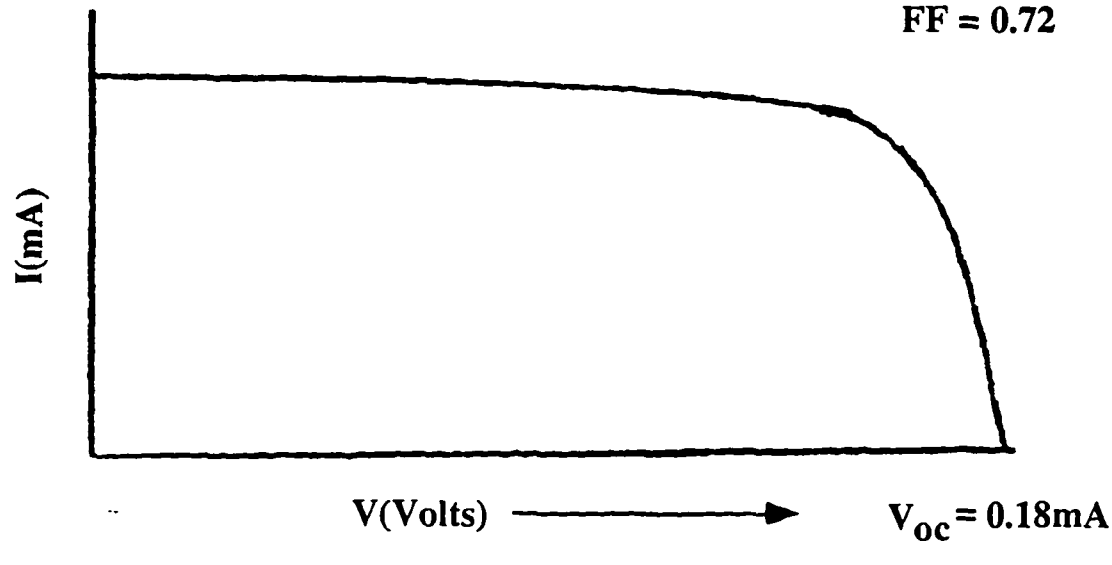

Figure 4.50. I(V) curve for a cell made using He ECR when the buffer layer was appropriate.

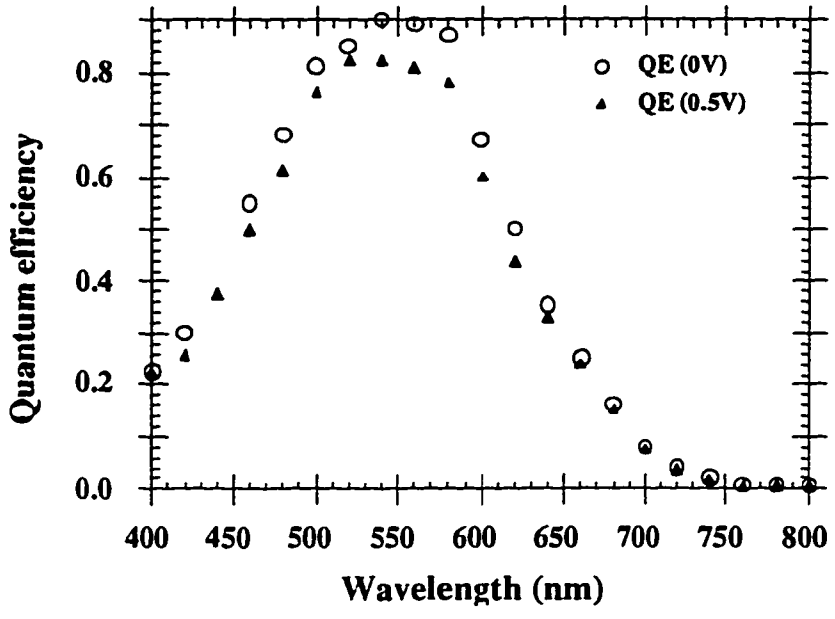

Figure 4.51. QE curve for the cell whose I(V) curve is shown in Figure 4.50.

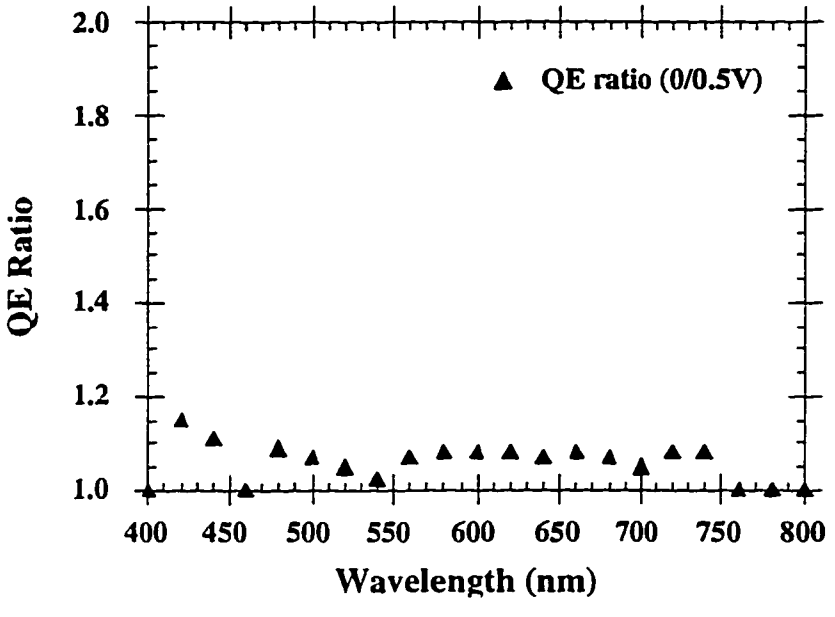

Figure 4.52. QE ratio of the cell whose I(V) is shown in Figure 4.50.

, one made using Hydrogen, and one made using helium. It is apparent from the examination of Figure 4.9 that indeed, the device made using helium as the plasma gas has a lower bandgap, by about 35meV, than the device made using hydrogen, thus confirming the results obtained in the study of the films. The low values of Urbach energies imply low defect densities, an observation which agrees with excellent hole collection and high fill factors.

4. Hole $\mu\tau$ Product

The $\mu\tau$ product of holes is a very important parameter for devices as discussed earlier. It is the quantity which primarily determines the fill factor of the cell. This assertion arises from the fact that over most of the cell, the holes are minority carriers (the carrier with lower $\mu\tau$ product). Only near the p-i interface do the electrons become the minority carriers. Therefore in order to have a high collection efficiency for most wavelengths of light absorbed in the cell, the hole range $\mu\tau$ E, where E is the electric field, must be large as compared to the thickness of the i-layer. A ratio of 10:1 or 20:1 is desirable. In a-Si:H solar cells, this condition is easily met, since the hole $\mu\tau$ product is about 4-6x10^{-8} cm^2V^{-1} and electric field is about 1 to 2x10^4V/cm. Thus the range is about 5-10μm, much larger than the thickness of the i-layer.

The basic principle of the measurement technique as explained earlier is quite simple. We measure the quantum efficiency of the device for a set of wavelengths as function of applied voltage. The details of the relavent parameters used for this study is tabulated in Table 4.7. A typical set of measured curves for a-Si:H substrate type device (2/1951) is shown in Figure 4.53. Under the reverse bias, the quantum efficiency increases and under the forward bias, it decreases. Since this change in quantum efficiency is due to the increase or decrease of the field in the device, one should be able to model the field profile and obtain $\mu\tau$ product from

Table 4.7. Devices fabricated for hole μτ studies.

Device #	I-layer parameters			V_{oc}	FF	$\mu\tau_h$	E_u
	T(°C)	SiH4	He	(V)	(%)	(cm^2/V)	(meV)
2/1950	400	10%	100%	0.778	62.4	3.6x10-8	48.5
2/1951	375	10%	100%	0.787	63	4.4x10-8	47.6
2/1952	425	10%	100%				
2/1955	425	20%	100%	0.786	61.4	2.0x10-8	48.0
2/1954	400	20%	100%	0.78	63.2	3.4x10-8	48.0
2/1953	375	20%	100%	0.764	64	4.2x10-8	46.5

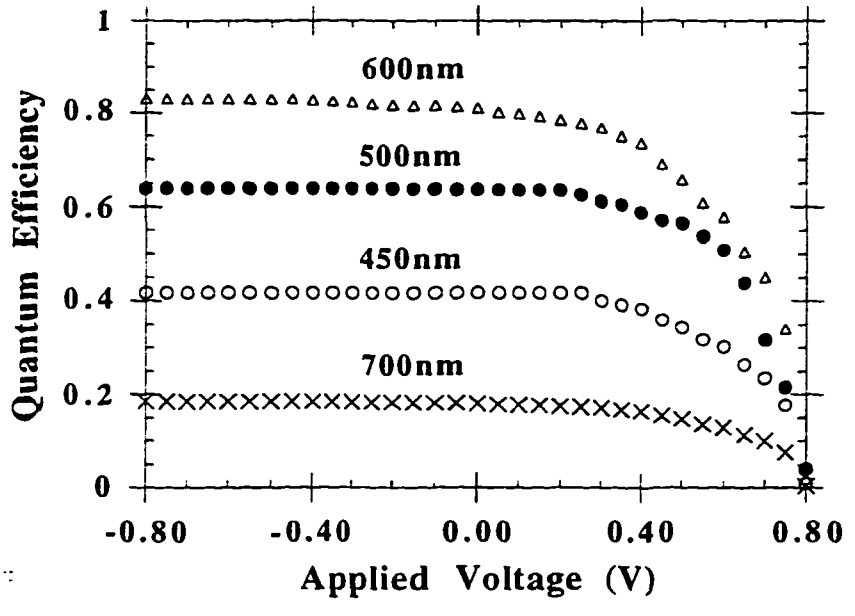

Figure 4.53. The quantun efficiency values at four wavelengths from sample 2/1951.

the curves. For a given device one should then be able to fit all the QE values (for different wavelengths) using the same value of mt product, except for the shorter wavelengths where p-i interface recombination becomes important and the model is no longer valid. But certainly, for long wavelengths in the range of 600-800nm, the model should be valid and give a reasonably accurate value of $\mu\tau$.

In order to determine the value for the $\mu\tau$ product in the constant bandgap devices, an accurate model of internal electric field in the i-layer must therefore be found. The method that we used to determine the correct electric field profile and subsequently the $\mu\tau$ is described next. We chose to model the field using the defect density profile used by Hack and Shur many years ago[54]. The electric field profiles were then obtained from equation 2.32 in a way which was similar to the earlier approach adopted by Greg Baldwin. Figure 4.54 shows a typical electric field profile in the device under zero and forward bias. Note that our model specifically includes the non-uniform field profile, and hence, a non-uniform range over the thickness of the cell. The collection efficiency is then calculated using a field assisted diffusion length, as defined by equation 3.23. This diffusion length is a function of the location of the absorbed photon and therefore one has to use a double integration over the distance to derive the collection efficiency for any given wavelength according to the equation 3.29.

The fits of experimental data and the model for the device 2/1951 is as shown in Figure 4.55. We see that the model fits reasonably well with experimental data. The only adjustable parameter that we used for modeling the field was the mid gap defect density g_0 expressed in $\#/cm^3\,eV$($2x10^{15}$ cm^{-3} eV^{-1} used in our case). Once this was selected we tried fitting the experimentally obtained QE vs. voltage curves using different values of $\mu\tau$. In contrast to the previous work done by Greg Baldwin (who developed this model), the interface electric field was not used as an additional parameter to fit the QE curves as shown in Figure 4.55. We used the exponential distribution with different characteristic energies for both conduction and

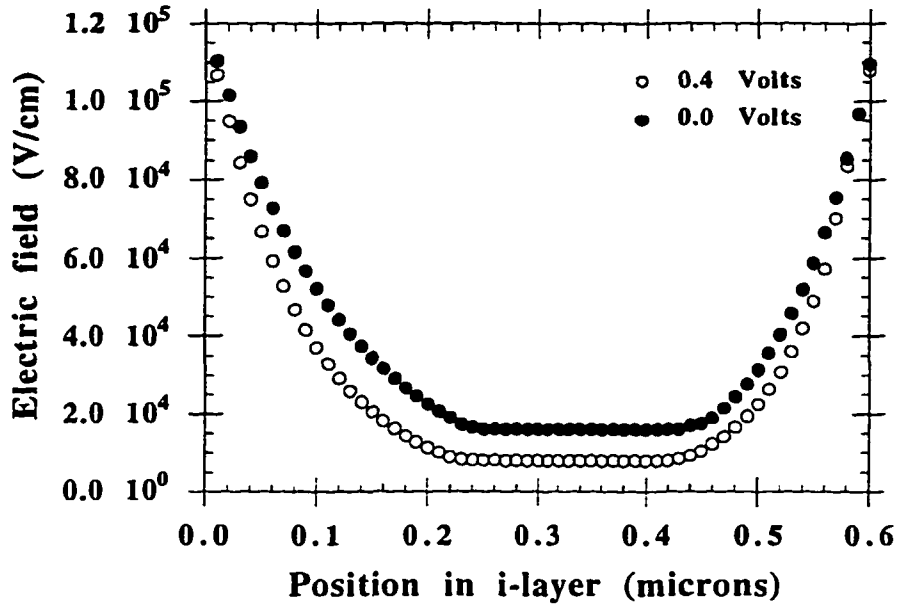

Figure 4.54. Simulated electric field profile in the i-layer at two different voltages.

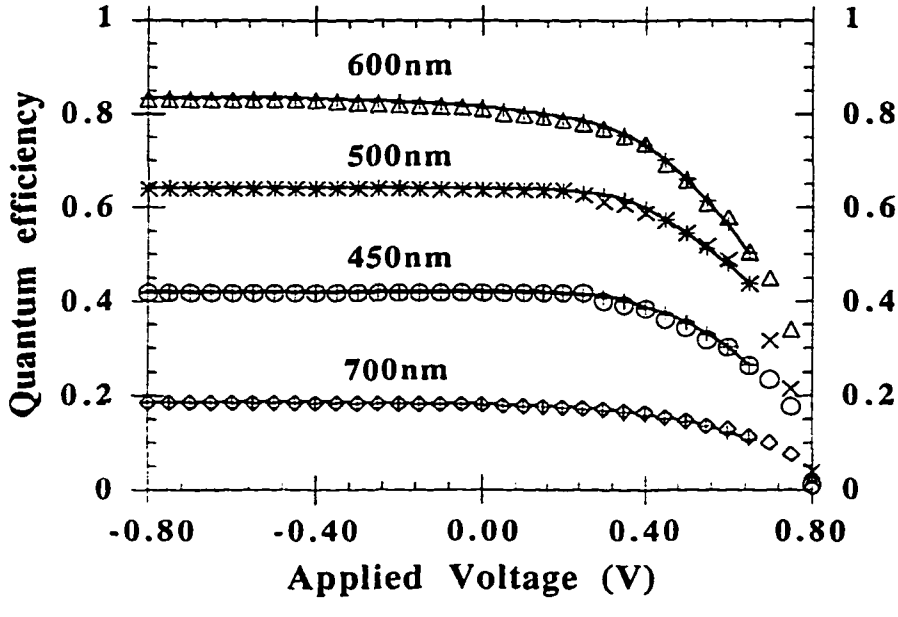

Figure 4.55. Non-uniform electric field approximation (solid lines) for the quantum efficiency values (points) at four wavelengths for the sample 2/1951.

valence band tail, these being 25 meV for conduction band tail and 46-49meV for valence tail as experimentally determined from the sub bandgap measurement on each cell. In comparison Baldwin in his model used the same linear characteristic slopes for both valence and conduction band tails. This modification in the model gave us a more accurate profile for density of states and thus led to an accurate field profile. When the model was thus modified, the difficulty that he faced in terms of his model predicting consistently higher QE values disappeared, resulting in a better fit without using the tailoring of electric field an additional parameter to fit the experimentally obtained data. This effect can be well explained in terms of equation 3.29. Note that it is still not possible to fit the data accurately for strong high forward biases (beyond maximum power point) using such simple models, since forward injection changes the field profile.

Using such fits, we have calculated the values of hole $\mu\tau$ products for various substrate type devices made using He-ECR discharge. The details are as shown in Table 4.7. All the devices had the thickness of i-layer between 0.46μm to 0.54μm. In summary, we can say that by performing a systematic study of material and device properties, one can obtain significant information on the performance of the devices.

5. Device Stability

For our experiment we selected three nearly identical substrate type cells, one deposited using H-ECR, one with He-ECR, and one using glow discharge. All had nearly the same initial fill factors and V_{OC}, with very similar i-layer thickness (within 10%). The fill factors were in the range of 67%-68%. All these cells were grown on stainless steel substrates, and had the top Cr contacts. We subjected these three cells to the light soaking from an ELH lamp which was focused down to give incident intensities of about 6xsun, which is about 1.6 sun

into the cell. The cells were maintained at temperature of 20°C using a water cooled mounting block.

The results for the degradation of the fill factor, which is the primary indicator of the material quality degradation, for these three cells are as shown in Figure 4.56. From Figure 4.56, we can conclude that H-ECR cell degrades much less than either the glow discharge or He-ECR cells whose relative degradations are very similar. This is a striking result. What it says is that, H content by itself is not an indicator of material stability. Even though the He-ECR film has less bonded H (~4-5%) as compared to H-ECR film (~8%) or GD film (~8%), it degraded in a similar way as the glow discharge device did. We therefore come to the conclusion that only by changing the localized microstructure, and therefore the H bonding, can we change stability. Hydrogen etch during growth does change the microstructure, and presumably makes it more robust against degradation [55].

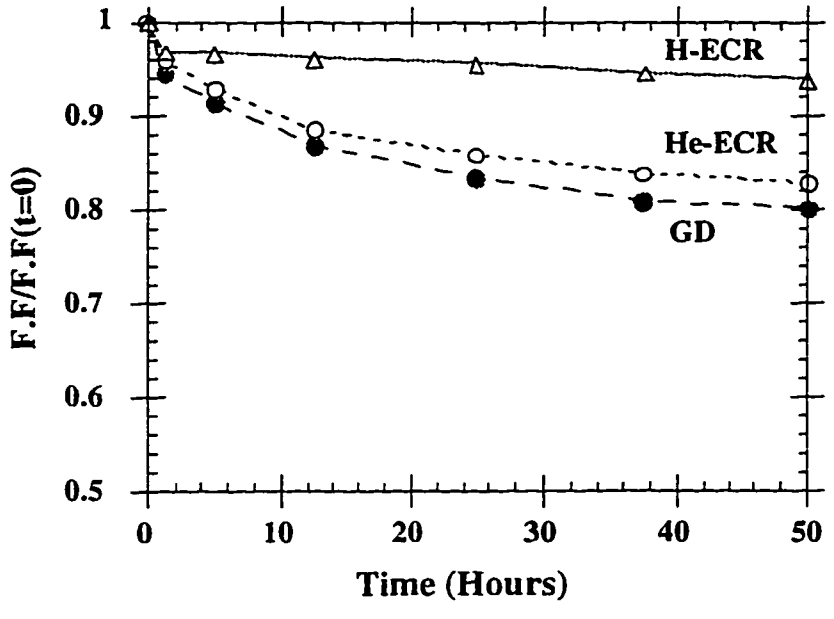

Figure 4.56. Degradation in fill factor for H-ECR, He-ECR and GD cells[55, 58].

Recently Dalal et.al.[56] explained this phenomenon from the basic considerations chemical growth mechanisms. To recap, let us first consider the growth chemistry of films without any dilution with H. There is considerable evidence (McCaughey and Kushner, 1989) that SiH_3 and SiH_2 radical are important precursors for film growth and that ion (SiH^{3+}) bombardment plays a critical role in film growth. A simple model of surface shown in Figure 4.57, is that it consists of active sites, containing at least one dangling bond , and passive sites, containing either silicon or hydrogen atoms at all four bonds. The dangling bonds are created by ion bombardment, which also removes hydrogen from the surface. SiH_2 radical can insert itself into the lattice upon impact with the surface at either active or passive sites, leading to film growth in a manner similar to that of physical vapor deposition.

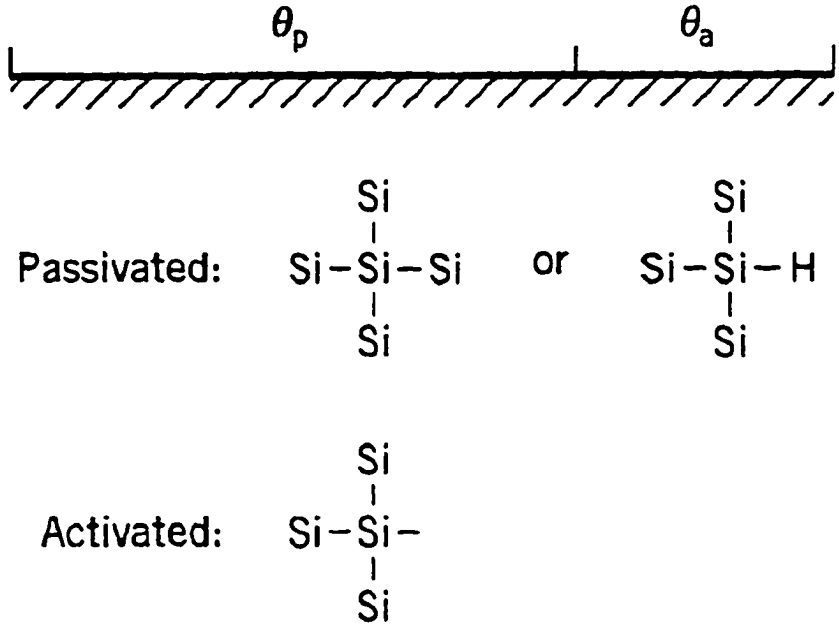

Figure 4.57. Surface coverage model for amorphous silicon deposition. θ_a and θ_p are the fractions of the surface that are active and passive, respectively [57].

Such films are generally of poor quality, having voids, undesired surface roughness, and other surface defects. Adsorbed SiH_3 radicals can diffuse along the surface but can insert in to the lattice only at active sites, filling in the surface roughness and contributing to growth of smooth, high quality film. Thus we see that those sites which get SiH_2, remain active after insertion of the radical, but the sites which receive SiH_3 become inactive (there is no free electron to bond to) after insertion of the radical. Since further growth can take place at active sites, the inactive site will first have to have its H removed, e.g. by reaction with the small amounts of H produced in the discharge. Thus the active site requires a single step for bonding, whereas a passive site requires two steps for bonding. This will result in to non-homogenous microstructure, which plays a significant role in the Staebler Wrouski effect. In order to have a reasonably good homogenous growth it is necessary that either nearly all sites be active, or they remain active for same fraction of time, on the average.

This is what a high dilution rate of H does. Having a high H dilution during growth ensures that there is an abundance of H radicals present. The dilution ratio in our ECR system is typically is 20:1. The high flux of H compared to the flux of SiH_2 and SiH_3 arriving at the surface means that all the surface sites are presumably passive (bonded with H) initially. The first step in the growth is the removal of this H from the surface, by another H radical, making it an active site.

$$H + \theta_A \rightarrow \theta_P \tag{4.1}$$

$$H + \theta_P \rightarrow \theta_A + H_2(g) \tag{4.2}$$

Since there is abundance of H around, most sites undergo this active passive transition. Thus, on the average, the fraction of time for which the site is active is the same for most of the sites. Thus H dilution should, in principle, be leading to more homogenous growth on

microstructural scale. As explained earlier hydrogen also has a second beneficial effect. The effective ratio of production of SiH_3/SiH_2 increases, perhaps by as much as a factor of 10, when H is present. This, of course leads to a better microstructure, since now, predominantly, one type of radical is presented to induce growth. One of the logical conclusion from the above discussion is that, having He as the dilutent gas should not lead to a better growth chemistry(except for the beneficial effects of ion-bombardment), since He does not do any chemical bonding with silicon during growth. Thus, it is not surprising that the solar cells produced using He-ECR did not lead to high stability, when compared to solar cells produced using H-ECR. These results are consistent with the results on the microstructure that we obtained through the selected area diffraction patterns using TEM as shown earlier, on the material grown using both H_2 and He dilution.

V. CONCLUSIONS

In conclusion, in this thesis, we have shown how to make more stable a-Si devices using ECR deposition. Previous work in our group had shown the ECR technique, using H beams, can be used to deposit more stable a-Si:H films. We have extended this work to the fabrication of high quality p-i-n solar cell devices in two different geometeries, substrate and superstrate, and have shown that these devices are also more stable than the devices deposited using the glow discharge technique. This is the first thesis reporting the development of such devices using the ECR process.

In order to fabricate high quality superstrate devices using the ECR process, we had to address the problem of high-temperature induced B diffusion at the p/i interface. We solved this problem by using innovative (Si,C) buffer layers, in combination with graded doping and graded bandgap in the p-layer. Once the devices were fabricated, they were tested for stability against similar glow discharge-produced devices. For such comparison, very careful criteria related to similarities of voltages, fill factors and thickness of i-layer were used to make sure that the devices were comparable, so that the results of the tests would be meaningful and unambiguous.

In order to further improve the devices, we went over to a different geometry, the substrate geometry, where the problems of B diffusion could be avoided. In order to make good devices, we had to develop novel techniques for reducing the effects of residual P contamination of the reactor, which we did by using a double-n layer approach, combined with a thorough reactor flush and plasma cleaning procedure. These substrate devices had higher voltages and fill factors than the devices produced using the superstrate geometry. The very high fill factors achieved (72%) indicate a very high quality for the i-material in the p-i-n

device. We compared the stability of these devices against the stability of the similar devices made using the glow discharge (GD) process, and found that these devices were more stable than the GD-device, a result similar to the one obtained for the devices in the superstrate geometry. Careful measurements of quantum efficiency, before and after degradation, revealed that the improved stability of the devices could be directly traced back to the improved stability of the i-material in the device.

During the course of this work, we discovered that good materials and devices could be made using either He or H_2 as the plasma gas. Using He as the plasma gas led to material with significantly lower H content than was the case for the material made using H2 as the plasma gas. The lower H content for He-ECR material led to a smaller Tauc gap than for the H-ECR material. When we compared the stability of H-ECR vs. He-ECR devices, we found that the H-ECR device was much more stable than the He-ECR device, a very surprising result, since the standard model held that it was the H content that determined the stability of the material. We definitively show that it is not the H content per se, but, rather, what H does during growth which affects the stability of the device.

We also measured, for the first time, the mobility-lifetime ($\mu\tau$) product for the hole in H-ECR deposited a-Si:H. The $\mu\tau$ product was measured using the technique of quantum efficiency spectroscopy as a function of applied voltage. To deduce the $\mu\tau$ product, we had to develop a model for the electric field in the device. To do this, we modified the earlier model developed by Greg Baldwin in a way which better fits our E field profile to the more exact numerical calculations of Hack and Shur. The $\mu\tau$ product is in the range of 4.4×10^{-8} cm^2/V, indicating a high quality material.

In summary, we have succeeded in growing high quality devices in ECR produced a-Si:H material, and have shown that the material is of high quality and more stable than glow discharge produced a-Si:H. We have also shown that high H dilution during growth plays a major role in improving stability.

APPENDIX A. ELECTRON MOTION IN A STATIC MAGNETIC FIELD

Free electrons in the plasma generation region spiral around the static magnetic field lines, due to the Lorentz force.

$$\vec{F} = q(\vec{v} \times \vec{B}) \tag{A-1}$$

If we assume that $\vec{B} = B_o \hat{a}_z$, this can be written as shown in Equation A-2.

$$m \frac{d^2x}{d^2t}\hat{a}_x + m \frac{d^2y}{d^2t}\hat{a}_y + m \frac{d^2z}{d^2t}\hat{a}_z = qB_o\left(v_y \hat{a}_x - v_x \hat{a}_y\right) \tag{A-2}$$

By equating components, we get the results shown in Equation A-3.

$$m\frac{d^2x}{d^2t} = qB_o v_y \qquad m\frac{d^2y}{d^2t} = -qB_o v_x \qquad m\frac{d^2z}{d^2t} = 0 \tag{A-3}$$

Now by integrating with respect to t, we get Equation A-4.

$$\frac{dx}{dt} = \frac{qB_o y}{m} + C_1 \qquad \frac{dy}{dt} = -\frac{qB_o x}{m} + C_2 \qquad \frac{dz}{dt} = C_3 \tag{A-4}$$

The result in Equation A-4 can be put back into Equation A-3 to get separated differential equations. For example, the equation for x is

$$\frac{d^2x}{dt^2} + \omega_o^2 x = x_o \omega_o^2 \tag{A-5}$$

where $\omega_o = \frac{qB_o}{m}$ and $_ox = \frac{C_2}{m\,\omega_o}$. The solution to this equation is

$$x = x_o + R\cos(\omega_o t + \phi) \tag{A-6}$$

where R and F are the constants of integration. By taking the derivative of Equation A-6 we get the x-component of the velocity.

$$v_x = \frac{dx}{dt} = -R\omega_o \sin(\omega_o t + \phi) \tag{A-7}$$

This result can then be substituted back into Equation A-4 in order to get

$$y = y_o - R\sin(\omega_o t + \phi) \tag{A-8}$$

and

$$v_y = \frac{dy}{dt} = -R\omega_o \cos(\omega_o t + \phi) \tag{A-9}$$

where $y_o = \frac{C_1}{m\,\omega_o}$. Now if we square and add Equations A-6 and A-8 we see that the motion of the electron in the plane perpendicular to the magnetic field is circular with radius R.

$$(x - x_o)^2 + (y - y_o)^2 = R^2 \tag{A-10}$$

From Equations A-7 and A-9 we can solve for the radius.

$$R = \frac{\sqrt{v_x^2 + v_y^2}}{\omega_o} = \sqrt{v_x^2 + v_y^2}\left(\frac{m}{qB_o}\right) \tag{A-11}$$

Since the velocity of the electron in the z-direction (parallel to the magnetic field) is constant, the electron spirals around the z-axis with a frequency of

$$\omega_o = \frac{qB_o}{m} \tag{A-12}$$

and a radius given by Equation A-11 above.

APPENDIX B. CALIBRATION OF α_{subgap}

To calibrate the α_{subgap} obtained from sub-gap photo-conductiviity measurements, we have to be aware of the approximations used in obtaining α_{subgap}.

We are assuming that sub-gap photo-conductivity is proportional to the number of absorbed photons. The number of absorbed photons N_{abs}, is given by:

$$N_{abs} = \left(1 - e^{-\alpha t}\right) \qquad \text{(B-1)}$$

where 't' is the thickness of the film.

For regions of photon energy where 'α' is very small, e.g. 1.0E2 cm^{-1}, $N_{abs} = \alpha t$. However, in spectrophotometric measurements, this is not true. Here 'αt' can be 0.2 or even larger. Hence, we have to make a correction for 'α' obtained from subgap photoconductivity measurements. The procedure is as follows:

(1) Measure α from spectro-photometric measurements. Typically, α will be in range of 1E3 cm^{-1} and 'αt' may be 0.2-0.3. Call this α_R, for real α.

(2) Calculate α_{pc} using the relationship given by

$$\alpha_{pc} = \frac{\left[1 - \exp(-\alpha_R t)\right]}{t} \qquad \text{(B-2)}$$

This is the photo-conductivity 'α' which corresponds to the 'α' being measured in the subgap regime when 'α' is very small.

(3) Calibrate the subgap curve to actual 'α' curve by comparing α_{pc}, calculated above, with the measured 'α' from subgap photoconductivity measurements at the same

photon energy. This comparison should be done at several photon energies to reduce calibration errors, and should give the correct multiplier factor for the subgap photoconductivity curve. Note that the correction factors will be different at different photon energies (i.e., the correction for 1.7eV photons may be different from 1.75eV because of the non-small $\alpha\tau$ at 1.75eV). However, only one calibration factor for the low energy photoconductivity curve should result if measurements are made carefully, and the above procedure applied correctly.

REFERENCES

[1] Carlson, D.E., and Wronski, C.R., "Amorphous Silicon Solar Cells," *Appl. Phys.* Lett. **28**, 11 (1976).

[2] "Production of PV Modules Worldwide Soars 25% to Reach Record 35 MW in 1988," *Photovoltic News* **8**, 2 (1989).

[3] Loferski, J.J., "Conversion efficiencies in amorphous silicon solar cells," *J. Appl. Phys.* **27**, 277 (1956).

[4] Whisnant, R.A., Champagne, P.T., Wright, S.R., Brookshire, K.C., and Zuckerman, G.J., "Comparison of Required Price for Amorphous Silicon, Dendritic Web and Czochralski Flat Plate Modules and a Concentrating Module," *Proceedings of the 18th IEEE Photovoltic Specialist Conference* 1537-1544 (IEEE, New York, 1985).

[5] Carlson, D.E., "Amorphous Silicon Solar Cells," *Trans. Elec. Dev.* **ED-24**, 449-453 (1977).

[6] Carlson, D.E., "Recent Develpments in Amorphous Silicon Solar Cells," *Sol. Energy Mater.* **3**, 503-518 (1980).

[7] Hamakawa, Y., Okamoto, H., and Tawada, Y., "Valency Control of Glow-Discharge Produced a-SiC:H and its Application to Heterojunction Solar Cells," *Int. J. Solar Energy* **1**, 125 (1982).

[8] Catalano, A., D'Aiello, R.V., Dresner, J., Faughman, B., Firester, A., Kane, J., Schade, H., Smith, Z.E., Schwartz, G., and Triano, A., "Attainment of 10% Conversion Efficiency in Amorphous Silicon Solar Cells," *Proceedings of the 16th IEEE Photovoltaiic Specialist Conference* 1421-1422 (IEEE, New York, 1982).

[9] Catalano, A., U.S. Patent #4, 782,376 (1972).

[10] Catalno, A., Arya, R.R., Fortmann, C., Morris, J., Newton, J., and O'Dowd, J.G., "High Performance, Graded Bandgap a-Si:H Solar Cells," *Proceedings of the 19h IEEE Photovoltaiic Specialist Conference* 1506-1507 (IEEE, New York, 1987).

[11] Bennett, M.S., and Rajan, K., "Stability of Multi-Junction a-Si Solar Cells," *Proceedings of the 20th IEEE Photovoltaiic Specialist Conference* 67-72 (IEEE, New York, 1988).

[12] Moller, J.H., *Semiconductors for Solar Cells* (Artech House Inc., MA, 1993).

[13] Wolford, D.J., Reimer, J.A., and Scott, B.A., "Hydrogen evolution studies in amorphous silicon," *Appl. Phys.* Lett. **42**, 369 (1983).

[14] Adler, D., *Semiconductor and Semimetals* **21**, (Academic Press, New York, 1984).

[15] Tiedje, T., *Semiconductor and Semimetals* **21**, (Academic Press, New York, 1984).

[16] Winterling, G., and Muller, G., " Doping efficiencies in amorphous Silicon," *Physica Scripta* **T13**, 45 (1986).

[17] Muller, G., Mannsberger, H., and Kalbitzer, S., "Substitutional doping of amorphous Silicon, A comparision of different doping mechnisms," *Phil. Mag.* **B53**, 257 (1986).

[18] Street, R.A., Biegelsen, D.K., and Knights, J.C., "Defect states in doped and compensated a-Si:H," *Phys. Rev.* **B24**, 969 (1981).

[19] Wronski, C., and Staebler, D., "Optically induced conductivity changes in discharge produced hydrogenated amorphous silicon," *J. Appl. Phys.* **51**, 3262 (1980).

[20] Wronski, C., and Staebler, D., "Reversible conductivity changes in discharge produced amorphous silicon,"*J. Appl. Phys. Lett.* **31**, 292 (1977).

[21] Dresner, J.B., Goldstein, B., and Szostak, D., "Diffusion length of holes ina -Si:H by the surface photo voltage method," *Appl. Phys. Lett.* **38**, 998-999 (1981).

[22] Stutzmann, M., Jackson, W.B., and Tsai, C.C., "Annealing of metastable defects in hydrogenated amorphous silicon," *Phys. Rev.* **B 34**, 63-72 (1986).

[23] Stutzmann, M., Jackson, W.B., and Tsai, C.C., "Kinetics of the Staebler-Wronski effect in hydrogenated amorphous silicon," *Appl. Phys. Lett*. **45**, 1075-1077 (1984).

[24] Crandall, R.S., Carlson, D.E., Catalano, A., and Weakliem, H., "Role of Carbon in Hydrogenated Amorphous Silicon Solar Cell Degradation," *Appl. Phys. Lett.* **44**, 200-201 (1984).

[25] Carlson, D.E., Catalano, A., D'Aiello, R.V., Dickson, C.R., and Oswald, R.S., "Optical Effects in Amorphous Semiconductors," *Proc. Int. Top. Conf. on Opt. Eff. in Amorphous Sem.* (Snowbird, Utah, 1984).

[26] Catalano, A., Bennett, M., Arya, R., Rajan, K., and Newton, J., "Impurity and Temperature Effects on the Rate of Light-Induced Degradation," *Proceedings of the 18th IEEE Photovoltaic Specialist Conference* 1378-1382 (1985).

[27] Nakano, S., Tarui, H., Haku, H., Takahama, T., Matsuyama, T., Isomura, M., Nishikuni, M., Nakamura, N., Tsuda, S., Ohnishi, M., and Kuwano, Y., "Material Investigation for High-Efficiency and High Reliability a -Si Solar Cells," *Proceedings of the 19the IEEE Photovoltaic Specialist Conference* 678-683 (1987).

[28] Bube, R.H., Echeverria, L., and Redfield, D., "Evidence for a Stretched-Exponential Description of Optical Defect Generation in Hydrogenated Amorphous Silicon," *Appl. Phys. Lett.* **57**, 79-80 (1990).

[29] Park, H.R., Liu, J.Z., and Wagner, S., "Saturation of the Light-Induced Defect Density in Hydrogenated Amorphous Silicon," *Appl. Phys. Lett.* **55**, 2568-2660 (1989).

[30] Tawada, Y., Kondo, M., Okamoto, H., Hamakawa, Y., "a-SiC:H as a Window Material for High Efficiency a-Si Solar Cells," *Sol. Energy Mater.* **6**, 299-314 (1982).

[31] Swartz, G.A., "Computer Model of Amorphous Silicon Solar Cell," *J. Appl. Phys.* **53**, 712-719 (1982).

[32] Crandall, R.S., "Modeling of Thin Film Solar Cells: Uniform Field Approximation," *J. Appl. Phys.* **54**, 7176-7186 (1983).

[33] Faughnan, B.W., and Crandall, R., "Determination of Carrier Collection Recombination Arising from a Fall-Off in Length and Prediction in Fill Factor in Amorphous Silicon Solar Cells," *Appl. Phys. Lett.* **44**, 537-539 (1984).

[34] Hack, M., and Shur, M., "Physics of Amorphous Silicon P-I-N Solar Cells," *J. Appl. Phys.* **58**, 997-1020 (1985).

[35] Schwartz, R.J., Park, J.N., Gray, J.L., and Turner, G.B., "Numerical Modeling of a-Si:H Thin Solar Cells," *Tech. Dig. of the PVSEC-4* 607-613 (Sydney, Austrailia, 1989).

[36] Wronski, C.R., *Semiconductor and Semimetals* **21**, (Academic Press, New York, 1984).

[37] Hack, M., and Shur, M., "Analysis of the Light-Induced Degradation in Amorphous Silicon Alloy p-i-n Solar Cells," *J. Appl. Phys.* **58**, 1656-1661 (1985).

[38] Uchida, Y., Kamiyama, M., Ichikawa, Y., Hama, T., and Sakai, H., "Light-Induced Change in pin and nip-based a-Si:H Solar Cells," *Tech. Dig. of the PVSEC-1* 217-220 (Kobe, Japan, 1984).

[39] Smith, Z.E., and Wagner, S., "A Carrier Lifetime Model for the Optical Degradation of Amorphous Silicon Solar Cells," *Mat. Res. Soc. Symp. Proc.* **49**, 331-338 (1985).

[40] Kaushal, S.K., *Growth of high Quality a-(Si,Ge):H films using low pressure, remote ECR plasma technique* **17**, (ISU, Thesis, 1995).

[41] DeBoer, S.J., *Low temperature epitaxial silicon growth using ECR plasma deposition* **11**, (ISU, Thesis, 1995).

[42] Popov, O., *ECR Plasma Sources and their use in Thin Film Deposition* (currently unpublished)

[43] Knox, R., Dalal, V.L., and Popov, O., "Characterization of electronic and optical properties of a-Si:H films grown using ECR plasma," *J. Vac. Sci. Tec.* **A9**, 474 (1991).

[44] Kettani and Hoyaux, *Plasma Engineering* (John Wiely and Sons, New York, 1973).

[45] Chen, F., *Plasma Diagnostic Techniques* (Academic Press, New York, 1965).

[46] Dalal, V.L., and Fuleihan, C., "Stability studies on a-Si:H films" *Mat. Res. Soc. Symp. Proc.* **149**, 601 (1989).

[47] Baldwin, G.C., *Design and modeling of graded bandgap a-(Si,Ge) solar cells fabricated by plasma enhanced chemical vapor deposition* **47**, (ISU, Thesis, 1994).

[48] Dalal, V., "Comprehensive research on stability and electronic properties of a-Si:H and a-(Si,Ge):H alloys and devices." *Final Subcontract Report NREL/TP-411*, 7695 (1995).

[49] Kaushal, S.K., Dalal, V.L., and Xu, J., "Growth of high quality silicon-germanium f ilms using low pressure remote ECR discharge," *J. Non Crys. Solids* **198**, 563-566 (1996).

[50] Dalal, V.L., Kaushal, S.K., Ping, E.X., Xu, J., and Knox, R.D., "Microcrystalline and mixed phase Si:H: preperation, potential and properties of devices," *Mat. Res. Soc. Symp. Proc.* **377**, 137-142 (1995).

[51] Dalal, V.L., "Comprehensive research on stability and electronic properties of a-Si:H and a-(Si,Ge):H alloys and devices." *Final Subcontract Report NREL/ XG-1-10063-8* (1995).

[52] Dalal, V.L., Ping, E.X., Kaushal, S.K., Leonard, M., Bhan, M,K. and Han, K., "Growth of Amorphous silicon materials and devices with improved stability," *Appl. Phys. Lett.* **64**, 1862 (1994).

[53] Dalal, V.L., Kaushal, S.K., Girvin, R., Sipahi, L., and Hariasra, S., "Properties of substrate type a-Si:H devices prepared using ECR conditions," *Mat. Res. Soc. Symp. Proc.* To be published (1996).

[54] Hack, M., and Shur, M., "Physics of amorphous silicon alloy p-i-n solar cells," *J. Appl. Phys.* **58**, 997-1020 (1985).

[55] Dalal, V.L., Kaushal, S.K., Girvin, R., Hariasra, S., and Sipahi, L., "Improved stability in ECR deposited a-Si solar cells," *Proceedings of 25 IEEE Photovoltic Specialist Conference* 1069-1072 (IEEE, New York, 1996).

[56] Dalal, V.L., "Comprehensive research on stability and electronic properties of a-Si:H and a-(Si,Ge):H alloys and devices." *Quarterly Subcontract Report NREL/13318-08*, **4** (1996).

[57] Lieberman, M.A. and Lichtenberg, A.J., *Principles of Plasma Discharges and Materials Processing* (John Wiely and Sons, New York, 1994).

[58] Dalal, V,L., Kaushal, S.K., Knox, R.R., Han, K., and Martin, F., "Significant improvements in stability of amorphous silicon solar cells by using ECR deposition," *Mat. Res. Soc. Symp. Proc.* **377**, 1101-1104 (1995).

ACKNOWLEDGMENTS

I would like to take this opportunity to express my sincere gratitude to my major professor, Dr. Vikram Dalal, for his invaluable guidance and support throughout my graduate studies. I would also like to thank Howard Shanks, Dr. Gary Tuttle, Dr. Scott Chumbley, and Dr. Lamont for serving on my committee. Thanks are also due to Dr. Joe Shinar and Dr. Ruth Shinar for guiding me through the FTIR measurements. The support, help and ever friendly attitude of all the members of Iowa Thin Film group contributed positively towards the successful completion of this project

I would like to thank William Catron for the financial support provided during the past two years and EPRC, for providing the financial support during my first two years of research work at Microelectronics Research Center.

I am very grateful to Dr.Scott Deboer for not only his great friendship but also for giving me the opportunity to get involved in the design and establishment of the new ECR reactor. I gratefully acknowledge Dr. Ralph Knox for his invaluable assistance and suggestions throughout this project. I also take pleasure in acknowledging the technical help from my colleague Keqin Han.

Special thanks are due to Swati Hariasra for her invaluable help in typing of this thesis and for so many late nights of work at MRC.

I would also like to thank Greg Baldwin, Er-Xuan Ping, Russ Bruhn, Bill Liners, Francisco Martin, Philip Bungum, Jonathan Kavanaugh, Florence Olympie, Sandhya Gupta, Shidi Cheng, Raghuram, Carl Erickson, and Jason Harald for their friendship.

Finally, I would like to thank my mother and father for their support, patience, and love during my many years in school. Thanks also go to my brother Sunil, my sister-in-law